To my parents
(A mis papas)

Development of high field MR imaging and spectroscopy techniques of the prostate

ISBN: 978-90-393-6032-3

Printed by Proefschriftmaken.nl

The printing of this thesis was partially funded by Philips

Development of high field MR imaging and spectroscopy techniques of the prostate

Ontwikkeling van functionele MR beeldvormende technieken op hoge velden voor de prostaat en meer
(met een samenvatting in het Nederlands)

Proefschrift

ter verkrijging van de graad van doctor aan de Universiteit Utrecht op gezag van de rector magnificus, prof. G.J. van der Zwaan, ingevolge het besluit van het college voor promoties in het openbaar te verdedigen op dinsdag 1 oktober 2013 des middags te 12.45 uur

door

Catalina Sofía Arteaga de Castro

geboren op 21 Juni 1982 te *Santiago, Chili*

Promotoren:

Prof.dr. P.R. Luijten

Prof.dr. M. van Vulpen

Co-promotoren:

Dr. D.W.J. Klomp

Dr. U.A. van der Heide

INDEX

CHAPTER 1

Introduction

The probability of death due to prostate cancer has dropped since the early nineties up to now. However, prostate cancer is still the second cause of death in men older than 70 years old in The Netherlands, which results in about two thousand casualties per year (2-4) when including all men older than 50 years old. With the improvements in radiotherapy modalities and diagnostic imaging, prostate cancer can be detected earlier and therefore treated. However, there are still many cases in which the tumor is under-graded due to the low specificity of the diagnostic procedure. This last aspect is the one that we would tackle with the development of novel hardware (i.e. endorectal coil and combined setup) and MRS techniques.

This thesis work was developed to overcome the challenges encountered at the ultra-high field of 7 Tesla (7T) for magnetic resonance imaging (MRI) and spectroscopic imaging (MRSI) of the human prostate. In this chapter, the advantages of the ultra-high field strength of 7T and its challenges for MR imaging and spectroscopy are introduced. In addition, some of the techniques used throughout the different chapters are briefly explained with their particular effect to ultra-high fields.

1.1 Advantages of ultra-high field for MRI and MRSI

The ultra-high field strength of 7T offers several advantages compared to lower field strengths that can be exploited for MRI and MRSI. A higher intrinsic signal to noise ratio (SNR) can be obtained at 7T, given that the SNR is proportional to the main magnetic field strength B_0. The increase in SNR can be traded for higher spatial resolutions, beneficial for MRI and anatomy differentiation and for reducing partial volume effects. In addition, the spectral resolution increases at higher field strengths, hence metabolite peaks that overlap at lower fields obscuring information, can be resolved in an ultra-high field MRSI experiment.

1.2 Ultra-high field challenges

At the magnetic field strength of 7T, the radiofrequency (RF) wavelength in the body is reduced to about 12 cm, much less than compared to the wavelength at 3T. As a consequence, substantial non-uniformities appear on the RF transmission (B_1^+) and reception (B_1^-) fields. In addition, the RF penetration is also limited due to the wavelength shortening,

thus limiting the MRI acquisition of deeply located organs. Conventional phased-array body coils are inefficient at 7T, due to the increased local SAR deposition at the body surface and the insufficient RF penetration. The imaging of deeply located organs, such as the prostate, can be done with efficient surface coils like an endorectal coil (ERC), which in contrast to the inefficient phase-array coils, their proximity to the tissue helps reaching strong B_1 amplitudes in the prostate.

In the presence of the B_1^+ non-uniformities found at 7T, conventional pulses also become inefficient. The flip angles obtained with non-uniform B_1 fields can lead to low SNR and signal voids in the MRI. For MRSI, it can lead to signal cancellation within a voxel, stimulated echoes or insufficient water/lipid suppression, all which could contaminate the spectrum and create artifacts.

1.3 Adiabatic pulses

As the B_1 non-uniformities at 7T are unavoidable, they cannot be ignored. All the MRSI sequences developed in this thesis work made use of the so-called adiabatic pulses. These pulses are advantageous given that they can still achieve homogeneous flip angles in the presence of strong B_1 non-uniformities by using not only amplitude ($B_1(t)$), but also frequency (or phase) ($\Delta\omega(t)$) modulation functions as shown in equations 1.1 and 1.2. This is particularly useful for MRSI, where different flip angles over the excited volume could lead to signal cancellation. The functions $f_B(t)$ and $f_\omega(t)$ are unitless trigonometric functions such as the hyperbolic secant (sech), hyperbolic tangent (tanh) pair.

$$B_1(t) = B_{1max} f_B(t)[x'] \qquad 1.1$$

$$\Delta\omega(t) = \Delta\omega_{max} f_\omega(t)[z'] \qquad 1.2$$

The B_{1max} and $\Delta\omega_{max}$ are the modulation amplitudes and **x'**, **z'** indentify the unit vectors on the rotating reference frame or frequency frame (**x', y', z'**), that rotates at the Larmor frequency. In the rotating frame, the spins would feel an additional frequency component $\Delta\omega(t)/\gamma$, due to the frequency modulation of the adiabatic pulses, which deviates from the Larmor frequency over time. Therefore, the magnitude of the time-dependent effective B_1 RF field ($B_{eff}(t)$) would depend on the time varying

amplitude and frequency components, $B_1(t)$ and $\Delta\omega(t)/\gamma$ respectively. Hence, a second rotating frame (**x'', y'', z''**) that rotates at around B_{eff} is defined. In the second reference frame $\mathbf{B_{eff}}(t)$ remains static. However, analogous to the appearance of the additional frequency component in the rotating frame, a second additional frequency component appears in the second rotating frame as a consequence of $\mathbf{B_{eff}}'$. The second additional frequency component must be small to obey the *adiabatic condition* shown in equation 1.3. If $B_{eff} \approx B_{eff}'$ the spins can follow the effective field.

$$\frac{\Delta\omega(t)}{\gamma^2} << B_{eff} \qquad 1.3$$

The adiabatic pulses can be designed with a relatively large frequency sweep, which can overcome frequency offsets in MRSI. As long as the pulse is provided with sufficient B_1 amplitude over time, the adiabatic condition remains fulfilled.

1.4 Chemical shift and MR spectroscopy

Hydrogen (1H), present in water, is the most abundant nucleus in the human body, with 100% natural abundance. At 7T the 1H atoms resonate at the Larmor frequency f0= γB0 of 298 MHz.

The most interesting aspect of looking at the 1H nuclei is actually the environment in which they are embedded in. The surrounding chemical environment of a nucleus "shields" it from the main magnetic field influence with electrons that decrease the main magnetic field contribution as seen from equation 1.4. As a consequence, the Larmor frequency of the nuclei would also decrease by a factor σi due to the magnetic field shielding created by these electrons for the nucleus (equation 1.5).

$$B=B_0\,(1-\sigma_i) \qquad 1.4$$

$$\omega_i=\gamma B_0\,(1-\sigma_i) \qquad 1.5$$

,where $\gamma=2\pi\,\gamma$. The parameter σ_i would change for different chemical environments. Therefore, the final resonance frequency would be different, hence characteristic of a certain metabolite.

In human prostate cancer for example, several metabolites can be

differentiated by their distinct resonance frequency, such as choline (Cho), polyamines (PA), creatine (Cr) and citrate (Cit) that resonate at 3.2 ppm, 3.1 ppm, 3.0 ppm and 2.6 ppm respectively.

1.5 MRS in Prostate Cancer

The relationship between these metabolites and prostate disease has already been investigated elsewhere (1-3) showing that the ratio of (Cho+Cr)/Cit increases in prostate cancer. However, at lower field strengths, the Cho, PA and Cr overlap, thus the contribution of the PA is also included in this ratio. Therefore, the advantage of the increased spectral resolution at ultra-high field, such as 7T would help resolving overlapping peaks, such as PA from Cho and Cr, hence obtaining more specific metabolic information which may enhance the specificity of prostate diagnostics. An example of a typical prostate MR spectrum of the human prostate is shown in Figure 1.1.

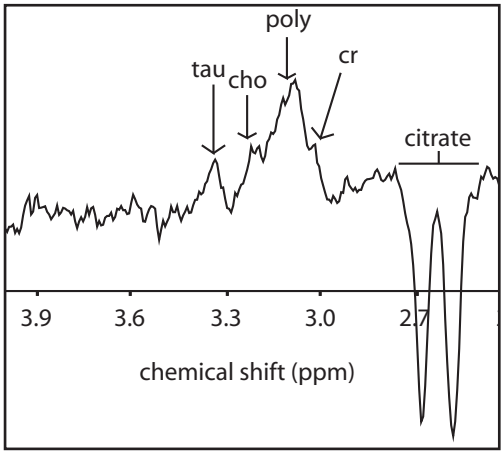

Figure 1.1: MRS of the human prostate obtained at 7 Tesla. Typical metabolites found in the prostate are Cho, Cr, Poly and Cit.

1.6 MRS editing

Besides the metabolites shown in Figure 1.1, more metabolic information can be obtained from the prostate with MRS. Although these metabolites may overlap with stronger signals coming from water or lipids they can still be measured using editing. Several molecules

contain two or more different hydrogen bonds on the same chain. In MR spectroscopy this causes the appearance of more than one peak in the MR spectrum. The different components of such molecule influence each other (i.e. they couple) and have a certain constant associated called J-coupling, which is expressed in hertz (Hz). The J-coupling between spin groups can be exploited to only manipulate (i.e. usually done with selective inversion) one of the J-coupled groups. Two MRS measurements are obtained, one with and one without manipulation. After subtraction of these two measurements, only signals from the coupled group would be visible. This technique is called MRS editing and it measures J-coupled metabolites. Therefore, even metabolites that have a low concentrations (i.e. lactate) that are obscured in the spectrum due to overlapping with signals with higher concentrations can be detected. The increased SNR available at ultra-high field strengths like 7T is an advantage for detecting such low concentrated metabolites.

1.7 Our approach

To overcome the shortening of the wavelength and reduced RF penetration at 7T, it is natural to think of getting closer to the tissue/organ of interest. Therefore, we investigate the feasibility of using an endorectal coil (ERC) for MRI and MRSI of the human prostate at 7T in **chapter 2**. A novel design of a dual-element ERC is explored to overcome the low penetration depth and for improving the coverage and $B_1^{+/-}$ strength over the prostate at 7T. As the ERC is a surface coil, it behaves as such by showing strong $B_1^{+/-}$ amplitudes closer to the ERC that drop-off with depth. To compensate for this $B_1^{+/-}$ non-uniformity, particularly in cases of large prostates, an array of radiative antennas is developed and investigated to use in combination with the ERC, without inclusion of additional hardware in the ERC (i.e PIN diodes) for uniform B_1 MRI in **chapter 3**. Not including PIN-diodes for decoupling the elements, means that both the radiative elements as the ERC can be used as transceivers. In this case, the RF coupling between the external and internal elements is also investigated and addressed, given that it could result in an increase of local SAR and efficiency reduction. As the ERC is able to transmit, strong B_1 MRSI can be obtained during the same MR scanning session. In **chapter 4** the surface coil properties of the ERC are exploited and used as an advantage for implementing dedicated MRSI sequences (i.e. nsLASER and cLASER) for 2D and 3D MRSI of the human prostate. Obviously, as the ERC does not supply homogeneous B_1 fields, these sequences are implemented with adiabatic pulses. Following the implementation of adiabatic sequences,

chapter 5 explores a MEGA-sLASER MRS editing technique to detect low concentration J-coupled metabolites, such as lactate with the inclusion of broad-banded adiabatic frequency offset corrected inversion (FOCI) pulses to maximize the efficiency at 7T. As the method requires a stable field, the human brain is used as a model for testing the novel MRS editing technique performance. Examples of increased detection efficiency for GABA and lactate signals are shown for the human brain.

During an MR examination the inner organs of the body move, causing either periodic (i.e. due to breathing or the cardiac cycle) or non-periodic (i.e. due to random bowel motion or gas pockets in the abdomen) field variations that can be observed and measured as an effect of susceptibility changes. **Chapter 6** shows the feasibility of measuring these susceptibility induced field variations using a field probe inside the housing of the ERC, without prior knowledge of their origin. The monitoring of the field variations is performed during the acquisition of an MRSI data set of a human prostate and used to retrospectively correct it. Improvement of the spectral line width and absence of artifacts demonstrate the effects of the retrospective field corrections.

Finally, on **chapter 7** the results found on the chapters are critically discussed. The benefits and limitations of the novel developed techniques are exposed and compared with results found in other studies. Possible improvements as well as indications for future studies are indicated.

REFERENCES

1. van Duin C, de Jong G, Stoeldraaijer L, Gaarsen J. Bevolkingsprognose 2010–2060: model en veronderstellingen betreffende de sterfte. Bevolkingstrends 2011;2e kwartal:28-41.

2. Heerschap A, Jager GJ, Van Der Graaf M, Barentsz JO, De La Rosette JJMCH, Oosterhof GON, Ruijter ETG, Ruijs SHJ. In vivo proton MR spectroscopy reveals altered metabolite content in malignant prostate tissue. Anticancer Research 1997;17(3 A):1455-1460.

3. Kurhanewicz J, Vigneron DB, Nelson SJ, Hricak H, MacDonald JM, Konety B, Narayan P. Citrate as an in vivo marker to discriminate prostate cancer from benign prostatic hyperplasia and normal prostate peripheral zone: Detection via localized proton spectroscopy. Urology 1995;45(3):459-466.

4. Shukla-Dave A, Hricak H, Moskowitz C, Ishill N, Akin O, Kuroiwa K,

Spector J, Kumar M, Reuter VE, Koutcher JA, Zakian KL. Detection of Prostate Cancer with MR Spectroscopic Imaging: An Expanded Paradigm Incorporating Polyamines. Radiology 2007;245(2):499-506.

CHAPTER 2

Improving SNR and B1 Transmit Field for an Endorectal Coil in 7 T MRI and MRS of Prostate Cancer

Magn Reson Med 68: 311–318. doi: 10.1002/mrm.23200

Abstract

Higher magnetic field strengths are desirable for MR spectroscopy given the increased spectral resolution and SNR. At high field strengths of 7T and above, substantial non-uniformities in $B_1^{+/-}$ and RF power deposition become apparent. In this investigation, we propose an improvement on a conventionally used endorectal coil (ERC), through the addition of a second coil element (stripline). Both coil elements are used as transceivers. In the center of the prostate, a $\sqrt{2}$ SNR increase is achieved as theoretically expected from a quadrature configuration. However, in low SNR regions observed when using a single loop configuration, the quadrature configuration gain in SNR is greater than $\sqrt{2}$. This is due to the natural asymmetry of the $B_1^{+/-}$ fields at high frequencies, which cause destructive (constructive) interference patterns. Global SAR is reduced by a factor 2 as expected. Furthermore, since the hotspots caused by the electric field of each coil element appear in different locations, a 4-fold decrease in local SAR is observed when normalized to the B_1 values in the center of the prostate. Due to the 4-fold local SAR decrease obtained with the dual channel setup for the same reference B_1 value (20 μT at 3.5 cm depth into the prostate) as compared to the single loop, the transmission power (B_1 duty cycle) can be increased 4-fold. Consequently, when using the two elements ERC, the RF power deposition is significantly reduced and RF intense sequences with adiabatic pulses can be safely applied at 7T for ^{1}H MRS and MRI in the prostate. Adiabatic RF pulses overcome the inherent non-uniformities of the transmit field that correspond to the surface ERC. In-vivo ^{1}H MRSI of prostate cancer with a fully adiabatic sequence operated at a minimum B_1^+ of 20μT, shows insensitivity to the non uniform transmit field, while remaining within local SAR guidelines of 10 W/kg.

2.1 Introduction

Magnetic resonance imaging (MRI) is a widely used technique to diagnose prostate cancer (PCa). When combined with dynamic contrast enhanced MRI (DCE-MRI), it can demonstrate a high sensitivity, although limited specificity (e.g. 88% (1)). To improve specificity, other MR techniques have been investigated. These include high resolution MRI, diffusion weighted MRI (DWI) and magnetic resonance spectroscopic imaging (MRSI). These methods have all shown improved specificity of PCa diagnosis and cancer staging (2-5), both at 1.5T and 3T.

The sensitivity and specificity of these MR techniques may benefit from the higher intrinsic signal to noise ratios (SNR) and spectral resolution afforded by higher magnetic fields strengths such as 7T. However, the low penetration depth of the RF field in the human body, limits the use of radiofrequency (RF) pulses to excite and refocus the spins at these high field strengths. Additionally, as field strength increases, electric field hotspots are dominant, thus leading to high local RF power deposition in electrically conductive tissues. Consequently, high specific absorption rates (SAR), limit the RF duty cycle substantially (6).

It has been demonstrated that local endorectal RF coils (ERC) composed of a single loop for transmit and receive can be used at 7T to avoid the penetration depth problems encountered with external coils (7,8). However, at high frequencies (300 MHz at 7T), the single loop approach suffers from substantial differences in B_1^- and B_1^+ fields, limiting the local transmit and receive efficiencies (9). As the RF wavelength approaches the dimensions of the single loop, the current density in the coil varies, resulting in greater spatial variance in B_1 efficiencies.

The use of multiple coil elements for transmission and reception of the MR signal has several benefits such as the ability of manipulating the distribution of the B_1^+ and B_1^- fields. In addition, if the coil geometries are chosen such that their field orientations are orthogonal (quadrature) and their efficiencies are similar, a $\sqrt{2}$ increase in SNR can be expected.

Considering the geometry and the limited space inside of the endorectal coil, a stripline (or a flattened loop if the space for the shield is limited) is a good candidate for a second coil element. Even more, the field orientation of this second element can be orthogonal to the field of the loop coil, which makes it a strong second element candidate. For this second element, the field strength per unit of current density will

be significantly lower at the location of the prostate than for the loop coil. However, the current density per unit of power will be substantially higher. Particularly, if the stripline is surrounded by non-conductive material (latex balloon of the endorectal coil and non conductive liquid) the loaded quality factor (Q) of the stripline will be much higher than for the loop coil, which is in close contact with the tissue. Therefore, the B_1 per unit of power of the stripline can be similar to the B_1 the loop. Even at the location of the prostate.

The properties of a combined coil setup can be used to increase SNR and to reduce the RF deposition or to increase the RF duty cycle, whilst remaining within 10 W/kg local SAR averaged over 10 grams of tissue according to the SAR guidelines of the International Commission on Non-Ionizing Radiation Protection (ICNIRP) (10).

In this study, we have added a stripline with a small sized shield to a conventional 7T endorectal coil that consists of a single loop coil. Both loop and stripline elements are used as transceivers. Using phantom measurements and numerical simulations, SAR levels and B_1 patterns are explored and subsequently validated in-vivo. The full RF duty cycle potential of this dual channel endorectal coil is illustrated by application of a fully adiabatic (LASER (11,12)) sequence at 7T for uniform MRSI in the prostate while remaining within SAR guidelines.

2.2 Methods

2.2.1 Hardware

A 6 cm long stripline coil was fabricated using 3 mm diameter copper litz wire as the active conductor, similar to the design presented by *Eryaman et al.* (13). Litz wire obtained from the shield of a coaxial cable was flattened and used as the electric ground plane of the stripline element. The width of this shield was 0.5 cm. Due to the endorectal coil geometry (central tandem), the distance between the ground plane and the conductor was 1 cm. The stripline was tuned and matched to 50 ohms at 298 MHz using capacitors of 11pF, 6.8pF, 12pF and 18pF at both ends (Figure 2.1 a). This coil was positioned inside the inner balloon of a commercially available endorectal coil (ERC) (MEDRAD Inc., Indianola, Pennsylvania), beneath the loop coil. The stripline was isolated with a shrinking tube. This was done to electrically isolate the stripline from the liquid used to fill the inner balloon. The loop coil was fabricated using the same 3 mm diameter copper litz wire. Tuning and matching to 50 ohms

at 298 MHz was done with capacitors of 4.7 pF, 2x10 pF and 18 pF that were equally distributed along the loop (Figure 2.1 b). After fixation of the loop to the inner balloon, the outer balloon was placed on top, isolating all electrical components from the tissue. The dual coil setup was interfaced to a whole body 7T MR system (Philips Healthcare, Cleveland, OH, USA). The transmit chain was split using a quadrature hybrid box and two home built transmit receive switches were used to enable parallel acquisition from both coil elements.

Power reflection measurements (S_{11}) were obtained to check the matching of both coils at the resonance frequency. In addition, loaded and unloaded Q-factors of each individual coil element were obtained to check the efficiency of the elements.

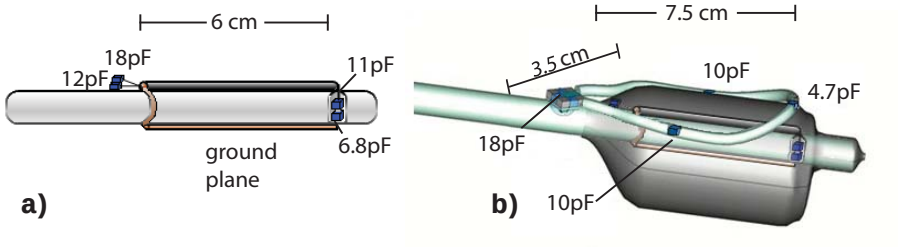

Figure 2.1: Schematics of the stripline element (a) combined with the loop element (b) of the endorectal RF coil. a: The 6-cm stripline coil element is connected to a ground plane through tuning capacitors of 11, 6.8, and 12 pF capacitance as shown in the figure. The 18-pF capacitor is used for matching to 50 ohm and is connected to the coil interface. b: Overall schematic of the ERC without outer insulator showing the stripline element inside the balloon and loop element on top of balloon with its corresponding capacitors of 4.7, 2x10, and 18 pF for tuning and matching, respectively.

2.2.2 Simulations

Finite difference time domain (FDTD) calculations were performed using a home-built software package developed based on methods explained in the study of *van den Bergen et al.* (14). The simulations were performed to calculate B_1^+ and B_1^- fields in a uniform phantom as well as in a realistic model of the human prostate (7,14) for both the loop and the stripline elements. The electrical and magnetic radiofrequency fields were calculated, from which the SAR distribution and B_1^+ fields were

derived.

The transmit field of the combined setup was determined by adding each channel derived B_1^+ field with a fixed 90 degree phase difference. The combined reception field was obtained per voxel by phasing and weighting each derived B_1^- field of each coil element. Local SAR (averaged over 10 grams of tissue) values of the single channel versus dual channel endorectal coils were calculated for the human prostate model.

2.2.3 Spectroscopy

The localization by adiabatic selective refocusing (LASER) sequence was implemented for detection of prostate metabolites. It included a sech/tanh adiabatic half passage (AHP) pulse for excitation, six sech/tanh adiabatic full passage (AFP) pulses for refocusing and spatial selection (11,15,16) and two Mescher Garwood (MEGA) refocusing pulses for water and lipid suppression (17). The adiabatic pulses were designed to work properly at a minimum $B1^+$ of 20μT. The sequence is shown in Figure 2.2 and it was used in combination with the dual channel endorectal coil.

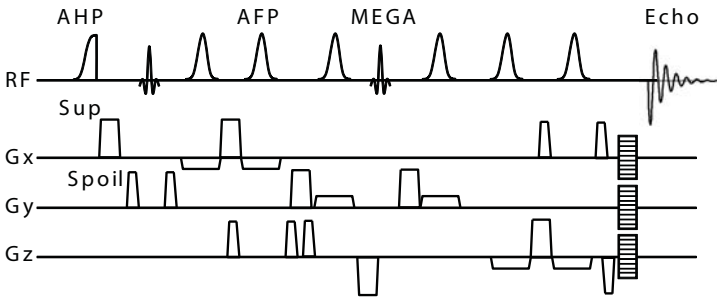

Figure 2.2: LASER sequence developed to use in combination with the dual channel endorectal coil for metabolite detection in patients with prostate cancer.

2.2.4 Phantom Measurements

A dual compartment water phantom filled with 33.4 grams per liter (g/l) of NaCl and 1250 g/l sugar in both compartments was used to investigate the SNR gain. The electrical properties of this phantom were chosen to approximate the average human dielectric properties of relative permittivity ε_r=55 and conductivity σ=0.64 Siemens per meter (S/m) at 7T. These concentrations resulted in measured electrical properties of

ε_r=53.4 and σ=0.63 (S/m) at 7T, in the double compartment phantom. Similar to the values reported by *Beck et al.* (18)

A second phantom was fabricated, containing gelatin to minimize heat conduction during temperature measurements. This phantom was fabricated using concentrations of 100 g/l of gelatin and 3g/l of salt. The endorectal coil was positioned inside the phantom while the gelatin was still in liquid state. This was done to avoid any possible air gap that could appear if the gelatin was removed to position the endorectal coil. The electrical properties of the gelatin phantom resulted in ε_r=70 and σ=1.3. No additional thermal isolation was used.

Gradient echo (GE) images of the water phantom were obtained using a fixed RF power setting, with the two coils operating in quadrature transmit (+90 degrees phase difference). The reception of the signal was done with both elements independently. The relative intensities in the proton density images reconstructed independently from the two elements of the uniform phantom reflect the sensitivity profiles (relative B_1^-) for each coil.

Temperature measurements were performed using three fiber optic temperature probes (Luxtron, Santa Clara, CA, USA, m3300 Biomedical Labkit). The probes were positioned inside the gelatin phantom on top of the capacitors of the dual channel endorectal coil that showed highest local calculated SAR values according to the FDTD results. The temperature measurements were obtained during a 12 minute sequence with a fixed total RF power of 12.6 Watt (W) going to either the loop coil or both coils (i.e. 6.3 W to each element, corrected for the losses in the quadrature hybrid box).

The performance of the LASER sequence was verified using a third phantom, which emulated the metabolites contained in the human prostate gland according to the recipe of *van de Graaf et al.* (19). The phantom consisted of creatine, choline, spermine, calcium, magnesium, calcium, citrate and zinc. A 2D CSI sequence was used (LASER, TR/TE=5000/159 ms, carrier frequency on citrate, 20x20 matrix, 30x30x10 mm FOV).

2.2.5 Patient Measurements

Eight prostate cancer patients with biopsy proven tumors (PSA levels 11.6-56.3) were selected for this study. Written informed consent was obtained for all patients and the study was approved by the local ethics

board. These patients were scheduled for treatment with radiotherapy. All patients were positioned in supine position with the in-house built dual channel endorectal coil inside the 7T MRI scanner. The inner balloon of the endorectal coil was inflated with perfluoro-polyether liquid (Fomblin, Solvay Solexis, Bollate, Italy), thus fixating the ERC to the rectal walls. This minimized the movement of the coil and surrounding structures and helped to avoid potential artifacts. T2 weighted images were required for tumor localization. Given sufficient patient scan time, additional MRI and MRS scans were also performed for prostate protocol development at 7T (proton density images, B_0 and B_1 maps, LASER 3D CSI).

T2 weighted turbo spin echo (TSE) images were obtained for anatomy and tumor localization (TR/TE=5000/100 ms, 312x306 matrix, 250x250x86 mm FOV, 8x2 mm slices) in all eight patients. In four of the patients, it was possible to obtain additional MR images that could be used for comparison of image quality between the single and dual channel endorectal coils. In order to obtain measurements with one element only, the RF transmit cable was directly connected to the transmit-receive switch of the stripline or loop coil. The other element was not removed from the endorectal coil and the inactive cable was terminated with a 50 ohm load. The whole setup change was done manually while the patient remained in the same position inside the magnet. This procedure allowed scanning with the stripline, the loop coil and the combined setup to be performed at the exact same position.

Of all the exams of the four patients, a single patient exam was used to obtain absolute $B_1^{+/-}$ field maps of the dual channel endorectal coil and of the single loop. The remaining three patients were used to obtain MRS data.

Gradient echo (GE) images (FFE, flip angle 60°, TR/TE 100/2 ms, 152x150 matrix, 300x300x35 mm FOV, 5x3 mm slices) were obtained for scouting and for qualitative comparison of single versus dual channel setups. B_1^+ field maps in-vivo were obtained for absolute quantification of the B_1 (multi angle prepulse, 2D FFE, flip angle 20-360° in 20° steps, TR/TE 150/2 ms, 160x132 matrix, 1x1x5 mm voxel (20)). B_0 field maps were obtained for image based second order B_0 shimming (2D FFE, TR/TE 150/3 ms, 5.8 ms delay, 160x132 matrix, 1x1x5 mm voxel) and for correcting the measured effective B_1 field (the measured B_1 field is a combination of the off resonance (B_0) field and the actual B_1 field). Single voxel (SV) (LASER, TR/TE 2000/159 ms, 15x15x15 mm voxel, 64 averages) and 3D chemical shift imaging (CSI) (LASER, TR/TE 2000/159 ms, 12x6x6 matrix, 25x40x25 mm FOV) measurements were obtained for

MR spectroscopy. Additionally, to keep the calculated SAR values within 10 W/kg of local SAR over 10g of tissue, temperature measurements using fiber optic probes (Luxtron, Santa Clara, CA, USA, m3300 Biomedical Labkit) were obtained. The fiber optic probes were accurately positioned on the most significant calculated hot spots (i.e. on top of the capacitors). This was done to assess real time RF safety information during the LASER sequence.

2.3 Results

2.3.1 Phantom Results

Measured reflection coefficients (S_{11}) in the loaded situation were -20 dB and -23 dB at 298 MHz frequency for the loop and stripline coils respectively. Measured loaded and unloaded Q-factors were 24, 176 and 58, 170 for the loop and stripline coil, respectively. These loaded factors were obtained in the water phantom with 3gr/l of salt. In-vivo loaded Q factors were also obtained for both elements. The corresponding values were 10.8 and 55 for the loop and the stripline respectively.

The dual channel endorectal coil showed minimal RF coupling (-18 dB) between its elements. This was expected due to the natural orthogonal alignments of the field produced by each coil. The receive field (B_1^-) reflected in the proton density images obtained for each individual coil showed a clear asymmetry in signal intensity. This asymmetry demonstrated higher signal intensities on the left of the field of view (FOV) for the stripline and on the right for the loop coil. As a result, signal voids were observed at the opposing sides (right and left of the FOV respectively) for the stripline and for the loop. Combining the proton density images from stripline and loop coils, not only enhanced SNR by approximately 40%, but the combination also improved the overall symmetry of the signal intensities. Apparent signal voids, observed when receiving with each coil element separately, disappeared when the reception fields were combined. The combined profile of signal intensities (loop and stripline) is shown in Figure 2.3 at a distance of about 3.5 cm from the outer balloon of the ERC. The observed signal asymmetries from each individual coil element, agree with the FDTD simulations obtained for the relative B_1^- fields of each individual coil (upper corner on Figure 2.3). From these simulations, it is also clear that both elements are able to generate a similar B_1 field per unit of power at the same depth. However,

the simulated B_1 field for the stripline remains slightly lower than for the loop.

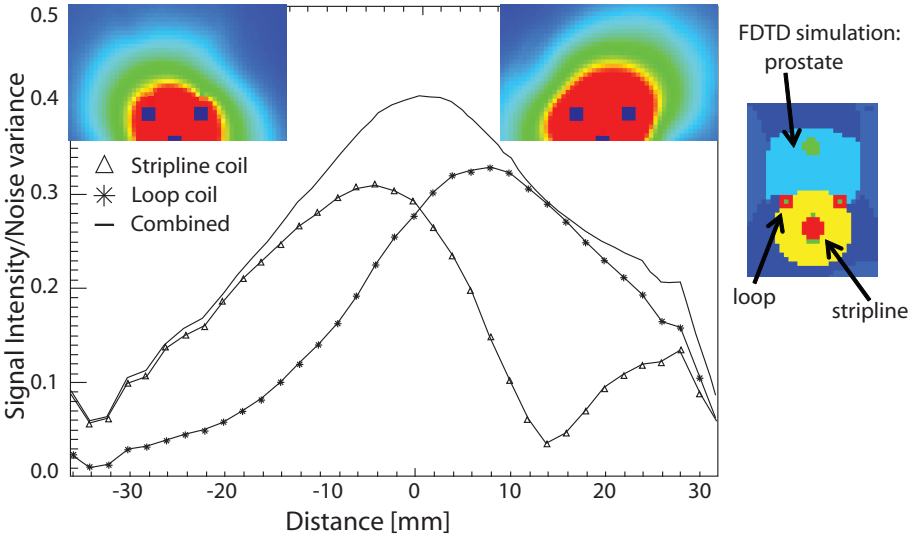

Figure 2.3: Solid line: Profile of the SNR parallel to the coil setup, obtained when combining the MR images for each coil element obtained in the phantom with conductivity and permittivity matched to prostate average values. The profiles correspond to a 3.5 cm depth into the phantom. In the center of the profile, a 40% increase in SNR is reached when combining both coil elements. Observe the increased symmetry and the absence of signal voids when both coils are combined, compared to the individual coil elements. In some areas, the SNR increase is even higher than $\sqrt{2}$. In the upper corners FDTD simulations of the B_1^- fields are shown for each individual coil element (left: stripline element, right: loop element), revealing similar asymmetry as observed in the phantom measurement. On the right, a schematic of the coil positions for the FDTD simulations is shown.

Temperature measurements on the gelatin phantom were obtained using a fixed total RF power. With the dual channel configuration, the fiber optic probes measured a 47.5% reduction in temperature rise on top of the initial capacitor of the loop (i.e. closer to the feeding point of the loop), when compared to the loop only endorectal coil (line 1 in Figure 2.4 *a, b*). This reduction in temperature increase merely reflects the decreased electric field of the loop coil that results from the split power used in the quadrature configuration. The temperature changes on the other two

investigated spots (middle and end capacitors) were also reduced for the quadrature configuration (18.3% and 37.8% respectively lines 2 and 3 in Figure 2.4). Because of the low reduction in temperature increase at these locations, the stripline and the loop contribute almost equally to the local SAR. Nevertheless, the stripline did not contribute to the maximum local SAR of the combined setup, compared to the contribution of the loop coil. The SAR calculations of the human body model obtained with the loop and combined setup were normalized to the B_1^+ obtained in the midline of the loop at a depth of 3.5 cm. The 10g RF power deposition was 4-fold lower for the combined setup than for the conventional loop coil. This is similar as observed in the phantom when considering the almost 2-fold reduced temperature increase per unit of power, in addition to the 40% increased B_1^+ per unit of power.

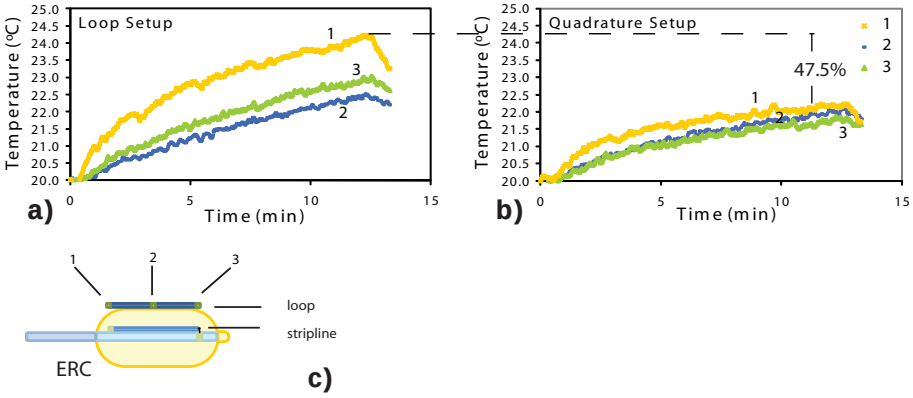

Figure 2.4: Temperature measurements on gelatin phantom during an MR sequence at a fixed RF power setting of 12.6 W (i.e. at approximately 10-fold higher SAR) during 12 minutes. The results show a) $\Delta T \approx 4^{o}C$ maximum increase for the single channel endorectal coil and b) $\Delta T \approx 2^{o}C$ maximum increase for the two coil elements endorectal coil. Using the quadrature setup, the temperature increase is reduced by nearly 50% around the capacitor in position 1, according to the schematics shown on c), when compared to the single coil setup.

Data obtained on the prostate phantom using the LASER sequence for 2D chemical shift imaging (CSI) demonstrate the excellent performance of volume selection with a chemical shift displacement artifact of 17% between citrate and choline (Figure 2.5*a*). Figure 2.5*b* shows the resulting spectra obtained using the LASER sequence on the prostate phantom. At this echo time (159ms), the strongly coupled spin system of citrate was in phase with the coupled spins of spermine as well as the singlets of choline and creatine.

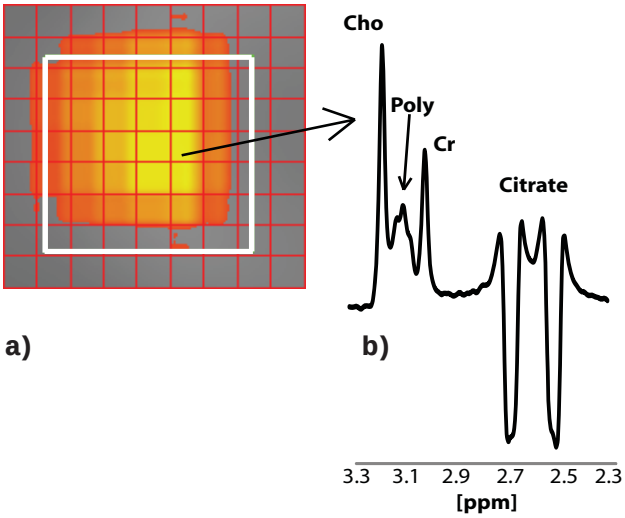

Figure 2.5: a) 2D CSI obtained from a prostate phantom. a) Chemical shift displacement between water and citrate. The white box shows the chosen volume of interest (VOI) with the carrier frequency set to choline, while the colored area represents the integral of the signal coming from citrate, shifted 0.6 ppm from choline. b) MR spectrum from 2D CSI measurement on (a), illustrating the peak appearances for choline, polyamines, creatine and citrate at 159 ms echo time with the LASER sequence.

This spectrum was used as a reference to verify the peak appearances in-vivo. In addition, the spectral map was obtained with uniform spin perturbation, resulting in a sensitivity that meets the reception profile (B_1^-) of the coil setup.

2.3.2 Patient Results

None of the patients complained about the insertion of the endorectal coil. Improvement of SNR and signal uniformity obtained with the dual channel endorectal coil compared to the single channel coil is shown by the T2-weighted TSE images in two patients (Figure 2.6). Improved coverage of the prostate in both transverse and coronal views is obtained with the dual channel endorectal coil (Figure 2.6 *b* and *d*). Furthermore, the signal voids and high intensity foci, previously visible in the images obtained with the loop only, are no longer apparent on images obtained with the dual element endorectal coil (highlighted by the red arrows on both transverse and coronal views in Figure 2.6 *a, c*).

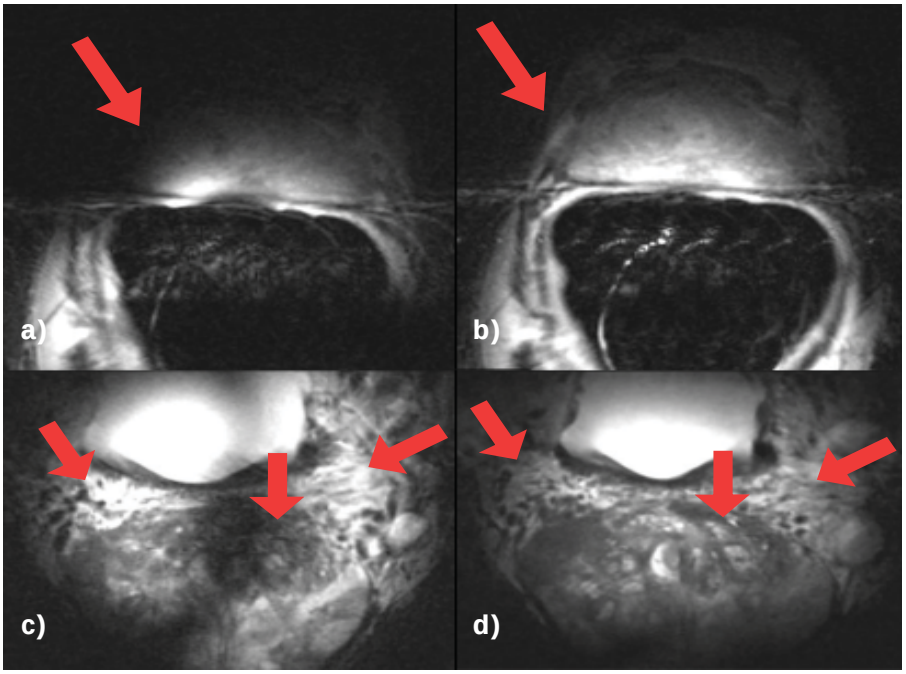

Figure 2.6: In-vivo T2-weighted images (TSE, TR/TE = 5000/100 ms, 250x250x86 mm FOV, 312x306 matrix,8 2 mm slices) at transverse views a) obtained with the single channel endorectal coil and b) with the dual channel endorectal coil. Coronal views c) obtained with the single channel endorectal coil and d) with the dual channel endorectal coil. Red arrows point the areas where coverage uniformity and absence of signal voids is improved, when using the dual channel endorectal coil.

Figure 2.7 *a, b* and *c* show the measured B_1^+ maps for the single and dual channel setups on the same prostate patient. A clear asymmetry of the B_1^+ field is evident when using the single channel setups (Figure 2.7 *a, b*) compared to the dual channel coil (Figure 2.7 *c*). In this patient, the B_1 field generated by the stripline is slightly lower than the one of the loop. Nevertheless, the dual channel coil setup provides significantly increased B_1^+ values in the prostate area compared to the single channel setup. Particularly when normalizing per unit of local SAR.

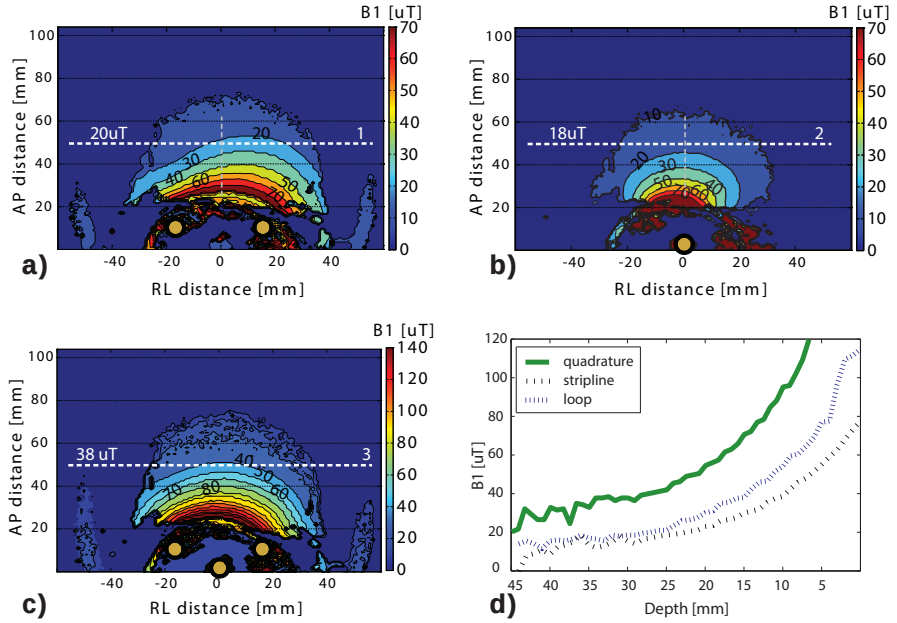

Figure 2.7: In-vivo measured B_1 maps for a) single loop element (two yellow dots on the image), b) single stripline coil (represented by the yellow dot) and c) dual channel configuration (two upper and one lower yellow dots representing the loop and stripline respectively), normalized to local SAR (i.e. at 800W RF peak power per element). The asymmetry that was present with the single elements (a, b) is no longer seen with the dual element configuration (c). The quadrature configuration has clearly higher B_1^+ values at the same location as compared to the loop and stripline only (e.g. locations 1, 2 and 3 shown with the white dashed lines). Vertical profiles (AP) at the RL midline are shown in d) to illustrate the B_1^+ efficiency of the stripline element. The location of the profiles is shown with the grey vertical dashed lines in a) and b). Similar B_1^+ values are obtained at the center of the prostate with both individual elements.

A 3D CSI measurement obtained with the LASER sequence for one patient is shown in Figure 2.8 *b*. Several highlighted voxels defined within the tumor location (depicted from the T2 images) show evident elevated levels of choline. Furthermore, the presence of non uniform B_1^+ fields that generally result in inversion (black) bands on the T2 TSE image (Figure 2.8 *a*) do not affect the obtained spectra (Figure 2.8 *b*). This is due to the successful implementation of adiabatic RF pulses with the dual channel endorectal coil.

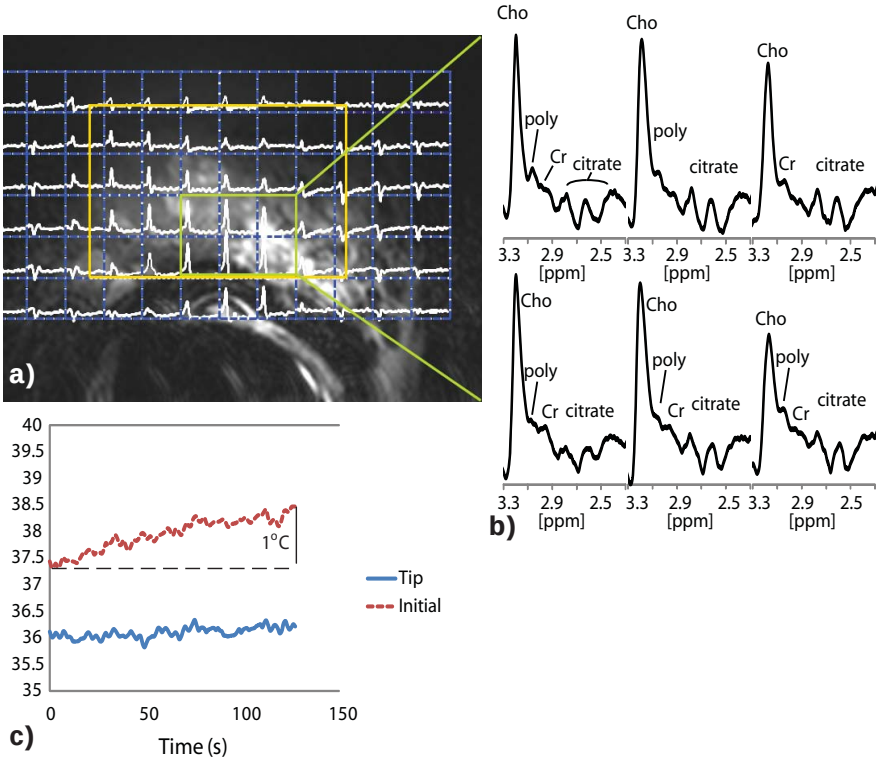

Figure 2.8: adiabatic 3D MRSI results obtained from human prostate cancer in vivo at 7T within SAR guidelines a) T2-weighted image of prostate gland (TSE, TR/TE = 5000/100 ms, 120x120x2.5 mm FOV, 240x240 matrix) with b) highlighted 3D CSI data obtained from a patient with PSA of 27 ng/ml using the LASER sequence (TE/TR = 159/2000 ms, NSA = 1, FOV = 36x36x36 mm, 6x6x6 matrix). Note the high levels of choline even in areas with black bands in the TSE images, reflecting the essence of using adiabatic RF pulses. c) Temperature measurements for monitoring RF heating during the 3D LASER sequence. The temperature increase at the calculated hottest spot (i.e. feed point of elements) was 1 degree Celsius.

Temperature measurements obtained for monitoring heating during the scans for the same patient are shown in *Figure 8*c. The temperature increase while the fully adiabatic LASER sequence ran at maximum local SAR level, remained less than 1°C.This result was obtained at the location calculated as having the highest SAR deposition (i.e. closest to the feeding point capacitor). Negligible temperature increases were observed for the regions situated around the capacitor located at the tip of the coil (deeper into the body).

2.4 Discussion

Higher field strengths such as 7 Tesla may offer improved SNR, spectral resolution and chemical shift displacement compared to lower fields like 3 or 1.5 Tesla (21-23). However, RF power deposition may pose a serious constraint when considering the use of many MR sequences at these higher field strengths.

In this study, we have shown that the use of a dual channel endorectal transceiver provides a 4-fold reduction in local RF power deposition when compared to the already efficient single channel endorectal coil at 7T. The increased RF efficiency allows the use of MR sequences that require higher RF duty cycles such as the LASER sequence. We have also shown that the spatial asymmetry of the B_1^+ and B_1^- fields at 7T for a loop element can be reduced when combined with a stripline element. Consequently, the overall SNR is greatly increased. Significant signal voids and high intensity foci are apparent when using a single coil element. These signal voids and high intensity foci disappear when using both coils simultaneously.

B_1 field simulations show similar efficiency in B_1 per unit of power at the center of the prostate, for the loop and the stripline elements, while their field orientations are orthogonal. Therefore, close to the expected $\sqrt{2}$ increase in SNR is observed in the phantom measurements with the quadrature configuration. Furthermore, an almost 40% increase in B_1^+ efficiency is observed in-vivo at the center of the prostate gland. Albeit, the stripline element can be seen as a flat loop, perpendicular to the loop coil, the B_1 per unit of current will be less. Moreover, the stripline element (flat loop) is more distant to the tissue than is the loop. However, when surrounded by lossless media, the loaded Q factor of the stripline is much higher than the Q factor of the loop coil (i.e. 5-fold). Additionally, the self-inductance of the stripline is lower compared to the self-inductance of the loop. The higher loaded Q factor combined with the low self-inductance results in increased current density normalized to RF power in the stripline compared to that of the loop. Consequently, the B_1 per unit of power of each element can be similar, even at the center of the prostate.

For a similar stripline element, *Eryaman et al.* (13) have shown that the optimal intrinsic SNR can be obtained with a 4 cm length element. In our case, the stripline length is set to 6 cm to cover approximately the same area as the loop coil, while avoiding overlap between both elements. In addition, the increased length of the stripline element allows greater

flexibility on the accuracy when considering the positioning of the ERC.

Temperature measurements obtained in phantoms show an almost 50% reduction in local RF heating when using the double element endorectal coil, in comparison to the single channel endorectal coil driven at equal RF power. This reduction in temperature increase was observed at the area of the capacitor exhibiting the highest electric field according to the FDTD simulations (closest to the feeding point). In fact, the electric field at this area was predominantly created by the loop coil, similar as observed by *Van den Bergen et al.* (14). Therefore, it can be inferred that the approximate 50% reduction in temperature increase found with the quadrature configuration was due to the heating caused by the loop coil. At the other measured positions (capacitors in the middle of the coil and deepest into the body), the heat increase was comparable for both configurations. Altogether, the local SAR per unit of power is decreased by a factor of two and the increased B_1^+ efficiency of the dual setup results in an almost 2-fold reduction in global SAR. Therefore, the local SAR per unit of B_1^+ is reduced by almost a factor of four.

In-vivo measurements show improved prostate coverage when using the dual channel endorectal coil. This was due to the increase in available SNR, RF uniformity and the disappearance of signal voids and high intensity foci as compared to the single channel endorectal coil. The inherent B_1 field non-uniformity of the surface coils remains. Nevertheless, the use of adiabatic RF pulses to overcome these non-uniformities can be explored further due to the relatively low SAR deposition of the dual channel coil setup.

External surface array and body coils have been explored at 7 Tesla to improve B_1 homogeneity and SAR deposition using B_1^+ shimming procedures (6). This approach has resulted in uniform T2 weighted images of the prostate. However, the available B_1 in the prostate region with external surface array coils is still low. Consequently, this results in low bandwidths in combination with conventional RF pulses and high SAR values when using broadband adiabatic pulses at 7T. Conversely, when using local RF coils for transmitting B_1 at high duty cycles, RF power deposition can remain low and adiabatic sequences can be applied within safety guidelines (10 w/kg local SAR averaged over 10 g of tissue (10)). In fact, adiabatic RF pulses have already been explored for MRSI in the prostate (24,7) as well as for other regions in the body (25,15,26) showing insensitivity to B_1 non-uniformities and excellent sharp slice profiles compared to non-adiabatic sequences.

The reduction in SAR deposition associated with the new dual channel endorectal coil makes it possible to explore the possibilities of using high RF consuming adiabatic sequences, such as the LASER sequence used for MRS (27). Although the feasibility of MR spectroscopy in the prostate using semi adiabatic sequences has been already shown (7,28), the non-adiabatic excitation in these sequences makes spatial detection still dependent on B_1 non-uniformities. The implementation of the LASER sequence in our study solved this spatial dependency problem as uniform flip angles were obtained in the prostate. Furthermore, the full potential of the reduced RF power deposition can be demonstrated with the use of the LASER sequence with high bandwidth RF pulses. The implemented LASER sequence with MEGA water and lipid suppression has a high RF duty cycle that remains within SAR guidelines of 10 W/kg local SAR using the dual channel endorectal coil.

Even when using a relatively long echo time (159 ms) the results obtained with the LASER sequence, showed distinctive signals from choline, creatine and polyamines. Furthermore, given the full adiabatic sequence, signals are correctly obtained in areas with substantial B_1 non-uniformity. This is illustrated by the inversion areas seen as black bands closer to the endorectal coil on the T2 weighted images. The halved temperature increase observed with the new endorectal coil as confirmed by in-vivo temperature measurements, shows the efficiency in RF power delivery of this new coil design, versus the conventional ERC. The high B_1 efficiency and distributed RF power deposition enables the use of the LASER sequence within safety guidelines (max local SAR of 10W/kg), thus making this a patient safe approach for MRSI of the human prostate at 7T.

2.5 Conclusions

Including a stripline element to the endorectal RF loop transceiver for prostate imaging enables improved SNR and reduced RF power deposition at 7T. Inherent B_1^+ and B_1^- field asymmetry of the individual coil elements complement each other through cancellation of RF hotspots and signal voids in different regions of the prostate. Since the stripline is fully integrated in the mechanical housing of the endorectal probe, prostate ^{1}H MRSI at 7T can be obtained with fully adiabatic sequences while remaining within safety guidelines with this SAR optimized dual channel endorectal RF coil.

REFERENCES

1. Ocak I, Bernardo M, Metzger G, Barrett T, Pinto P, Albert PS, Choyke PL. Dynamic Contrast-Enhanced MRI of Prostate Cancer at 3 T: A Study of Pharmacokinetic Parameters. Am J Roentgenol. 2007 Oct 1;189(4):W192-201.

2. Kozlowski P, Chang SD, Jones EC, Berean KW, Chen H, Goldenberg SL. Combined diffusion-weighted and dynamic contrast-enhanced MRI for prostate cancer diagnosis - Correlation with biopsy and histopathology. J Magn Reson Im. 2006;24(1):108-113.

3. Sato C, Naganawa S, Nakamura T, Kumada H, Miura S, Takizawa O, Ishigaki T. Differentiation of noncancerous tissue and cancer lesions by apparent diffusion coefficient values in transition and peripheral zones of the prostate. J Magn Reson Im. 2005;21(3):258-262.

4. Hosseinzadeh K, Schwarz SD. Endorectal diffusion-weighted imaging in prostate cancer to differentiate malignant and benign peripheral zone tissue. J Magn Reson Im. 2004;20(4):654-661.

5. Issa B. In vivo measurement of the apparent diffusion coefficient in normal and malignant prostatic tissues using echo-planar imaging. J Magn Reson Im. 2002;16(2):196-200.

6. Metzger GJ, Snyder C, Akgun C, Vaughan T, Ugurbil K, Moortele PVD. Local B1+ shimming for prostate imaging with transceiver arrays at 7T based on subject-dependent transmit phase measurements. Magn Reson Med. 2008;59(2):396-409.

7. Klomp DWJ, Bitz AK, Heerschap A, Scheenen TWJ. Proton spectroscopic imaging of the human prostate at 7 T. NMR Biomed. 2009;22(5):495-501.

8. Near J, Romagnoli C, Bartha R. Reduced power magnetic resonance spectroscopic imaging of the prostate at 4.0 Tesla. Magn Reson Med. 2009;61(2):273-281.

9. Hoult DI. Sensitivity and Power Deposition in a High-Field Imaging Experiment. J Magn Reson Im. 2000;12(1):46-67.

10. The International Commission on Non-Ionizing Radiation Protection. Medical Magnetic Resonance (MR) Procedures: Protection of patients. Health Physics. 2004;87(2):197-216.

11. Tannús A, Garwood M. Adiabatic pulses. NMR Biomed. 1997;10(8):423-434.

12. Norris DG. Adiabatic radiofrequency pulse forms in biomedical nuclear magnetic resonance. Concept Magnetic Res. 2002;14(2):89-101.

13. Eryaman Y, Öner Y, Atalar E. Design of internal MRI coils using ultimate intrinsic SNR. Magn Reson Mater Phy. 2009 3;22(4):221-228.

14. van den Bergen B, Klomp DW, Raaijmakers AJ, Arteaga de Castro C, Boer VO, Kroeze H, Luijten PR, Lagendijk JJ, van den Berg CA. Uniform prostate imaging and spectroscopy at 7 T: comparison between a microstrip array and an endorectal coil. NMR Biomed. 2010; DOI: 10.1002/nbm.1599.

15. De Graaf RA, Nicolay K. Adiabatic rf pulses: Applications to In vivo NMR. Concept Magnetic Res. 1997;9(4):247-268.

16. Lunati E, Cofrancesco P, Villa M, Marzola P, Sbarbati A. Evolution Strategy Optimization for Adiabatic Pulses in MRI. J Magn Reson. 1999 May;138(1):48-53.

17. Mescher M, Tannus A, Johnson MO, Garwood M. Solvent Suppression Using Selective Echo Dephasing. J Magn Reson Ser A. 1996 Dec;123(2):226-229.

18. Beck B, Jenkins K, Rocca J, Fitzsimmons J. Tissue-equivalent phantoms for high frequencies. Concepts Magn. Reson. 2004 2;20B(1):30-33.

19. van der Graaf M, Schipper R, Oosterhof G, Schalken J, Verhofstad A, Heerschap A. Proton MR spectroscopy of prostatic tissue focused on the detection of spermine, a possible biomarker of malignant behavior in prostate cancer. Magn Reson Mater Phy. 2000 Oct 1;10(3):153-159.

20. Brunner DO, Pruessmann KP. B1+ interferometry for the calibration of RF transmitter arrays. Magn Reson Med. 2009;61(6):1480-1488.

21. Vaughan JT, Snyder CJ, DelaBarre LJ, Bolan PJ, Tian J, Bolinger L, Adriany G, Andersen P, Strupp J, Ugurbil K. Whole-body imaging at 7T: Preliminary results. Magn Reson Med. 2009;61(1):244-248.

22. Tkác I, Andersen P, Adriany G, Merkle H, Ugurbil K, Gruetter R. In vivo 1H NMR spectroscopy of the human brain at 7 T. Magn Reson Med. 2001;46(3):451-456.

23. Vaughan T, DelaBarre L, Snyder C, Tian J, Akgun C, Shrivastava D, Liu W,

Olson C, Adriany G, Strupp J, Andersen P, Gopinath A, van de Moortele PF, Garwood M, Ugurbil K. 9.4T human MRI: Preliminary results. Magn Reson Med. 2006;56(6):1274-1282.

24. Near J, Romagnoli C, Curtis AT, Klassen LM, Izawa J, Chin J, Bartha R. High-field MRSI of the prostate using a transmit/receive endorectal coil and gradient modulated adiabatic localization. J Magn Reson Im. 2009;30(2):335-343.

25. Scheenen T, Klomp DWJ, Wijnen J, Heerschap A. 1H-MR spectroscopic imaging of the human brain using adiabatic refocusing pulses at 3 and 7T. In: Proc. Intl. Soc. Mag. Reson. Med. Berlin, Germany: 2007. p. 43.

26. Scheenen T, Heerschap A, Klomp D. Towards 1H-MRSI of the human brain at 7T with slice-selective adiabatic refocusing pulses. Magn Reson Mater Phy. 2008 Mar 1;21(1):95-101.

27. Garwood M, DelaBarre L. The Return of the Frequency Sweep: Designing Adiabatic Pulses for Contemporary NMR. J Magn Reson. 2001 Dec;153(2):155-177.

28. Klomp DWJ, Scheenen TWJ, Arteaga CS, van Asten J, Boer VO, Luijten PR. Detection of fully refocused polyamine spins in prostate cancer at 7 T. NMR Biomed. 2010 Oct. 24(3):299-306.

CHAPTER 3

Prostate MR Imaging with Extended Field of View and MR Spectroscopy with Strong B_1 at 7T using Active Decoupling

Submitted to Magn Reson Med

Abstract

Purpose: to generate uniform B_1 MRI and strong B_1 MRSI of the human prostate by combining an external transceiver array with an endorectal coil (ERC) without PIN-diode decoupling.

Methods: phantom measurements were performed at 7T to demonstrate actively decoupling of the ERC by transmitting counteracting fields to the coupled fields caused by the external elements. Four prostate cancer patients were scanned at 7T with the combined external-ERC setup. In-vivo B_1 maps, T2-weighted MRI and MRSI were obtained from the prostate by transmitting with either active decoupling or constructive interference at maximum allowed RF power.

Results: low RF coupling fields were observed in-vivo, which did not increase the maximum local SAR. Active decoupling could counteract the coupled field caused by the external array on the ERC. Consequently, uniform B_1 fields for MRI with enhanced SNR from the prostate when including the ERC for reception were possible. Additionally, optimal-short-TE, broad-banded MRSI was obtained when using all elements as transceivers. Additionally, the B_1 coverage to the anterior part of the prostate was extended by the external elements as shown with in-vivo B_1 maps.

Conclusion: uniform B_1 MRI combined with strong B_1 MRSI of the prostate is possible during one scanning session at 7T.

3.1 Introduction

Prostate cancer staging relies on transrectal ultrasound (TRUS) guided biopsies, which can often miss the tumor or the most aggressive part of it. Digital examinations and magnetic resonance (MR) T2-weighted images are used for disease and anatomy differentiation, but they lack specificity. It has been shown that MR spectroscopy (MRS) techniques are able to differentiate between benign, normal and diseased prostate tissue (1-3), thus increasing the specificity of tumor grading. However, MRSI suffers from a low sensitivity as the resonances of choline, polyamines and creatine overlap (4). The increased spectral resolution at ultra-high field magnetic resonance spectroscopy (MRS) would reduce this overlap, hence increasing the specificity of tumor grading in prostate cancer. In addition, the increased signal to noise ratio (SNR) can be traded for an increased spatial resolution, which reduces partial volume effects.

MRI and MRSI at ultra-high field are challenging mainly due to the substantial B_1 radiofrequency (RF) field non-uniformities caused by the short wavelength in tissue. Transmission with multiple channels that use constructive and destructive RF interference, can lead to uniform B_1 RF fields at the location of the prostate (5). However, with this approach the B_1 amplitudes remain relatively low, due to the limited available power using external coils or antennas at ultra high field strengths and concomitant SAR limitations (6). An approach to overcome the low B_1 levels is to use a dual-element transceiver endorectal coil (ERC) (7). The proximity of the ERC to the prostate and the additional transceiver element gives strong $B_1^{+/-}$ fields over the prostate. The strong B_1^{+} amplitudes achieved with the dual-element ERC would be beneficial to obtain short- TE and -TR MRSI with broad-banded adiabatic pulses and reduced local SAR (8). However, the ERC B_1 field is highly non-uniform, decaying with depth and consequently has a limited field of view. Hence, the ERC is not optimal for MR imaging.

To enable clinically useful MRI and MRSI of the prostate at 7T, an ERC transceiver should be combined with an external transceiver body array. The combination of an external transceiver array with a receive only (Rx) ERC has already been explored at a 7 Tesla system, where the use of PIN-diodes was indicated for decoupling the ERC from the transmit fields (9). However, the high power PIN-diode necessary for decoupling the ERC from the external array would use a large space in the housing of the ERC, hence causing patient discomfort during insertion of the ERC. Therefore, we propose an alternative to PIN-diodes for decoupling the ERC from the

external array by transmitting RF power with the ERC to counteract the RF coupling field caused when transmitting with the external elements. With this approach, the RF transmit field of the external array would not be influenced by the presence of the ERC without the PIN-diode. This investigation demonstrates that uniform B_1 MRI and high-bandwidth MRSI are possible at 7T during one scan session by combining an external transceiver body array with a transceiver ERC.

3.2 Methods

All MR measurements were performed on a 7 Tesla MR scanner (Philips Healthcare, Best, The Netherlands). The RF elements were interfaced with a home-built 8-channel transmit-receive switch with integrated pre-amplifiers (Advanced Receiver Research, Burlington, USA) that were connected to either two (phantoms measurements) or six (in-vivo measurements) 1 kW RF amplifiers (CPC, Hauppauge, New York, USA) and two 4 kW RF amplifiers.

3.2.2 Phantom MR Measurements

One single-sided adapted dipole (SiSiAD) antenna (10) and a loop coil in an ERC, both tuned and matched to 298.2MHz were used to investigate RF coupling between the elements in phantom experiments. A phantom emulating a body torso (twelve-sided cylinder of 36.6 cm width, 25.6 cm height and 36.2 cm length), filled with common tap water with 3 g/l of table salt was used. The SiSiAD antenna was positioned on top of the phantom and the ERC was inserted in a PVC tube inside the phantom in the mid-axial plane. To investigate the active decoupling with a stronger coupling between the elements, a smaller water phantom was used (square of 30x30x20 cm^3), also filled with common tap water and 3 g/l of table salt. In this case, one SiSiAD antenna and a dual-element ERC were used (7). The strong RF coupling between the elements was achieved in the smaller phantom by positioning both transceiver elements close to each other and tilting the ERC towards the SiSiAD antenna. The RF coupling between the elements was measured as a power transmission (S_{12}) obtained with a network analyzer (Rohde & Schwarz ZVL, Munich, Germany). To observe the effect of the RF coupling on the local B_1 field, MR images of the phantom were obtained transmitting with the SiSiAD only while receiving with all elements using a 2D FFE slice with 102 TFE factor, TE/TR=7/200 ms, 180° nominal flip angle, 400x400 mm^2 FOV,

408x204 matrix and 10 mm slice thickness. From the transition bands caused by the strong nominal flip angle (180 degrees) on the FFE images, local B_1 variations can be observed, which can be matched to a B_1 map of the ERC. The necessary power to generate the B_1 field with the ERC to counteract the RF coupling caused by the SiSiAD was then estimated. Next, transmission with the ERC was included to transmission with the external array, using the estimated RF power found previously. The ERC transmission phase was varied until RF decoupling between the elements was achieved (i.e. absence or alteration of transition bands caused by the ERC).

3.2.3 In-vivo MR Measurements

Four prostate cancer patients were scanned after they signed written informed consent. In-vivo measurements were performed with a double element ERC (7) combined with an array of six SiSiAD antennas (10) (4x1 kW posterior to the patient and 2x4 kW above the pelvis). After scouting the anatomy, all scans were acquired after performing B_1 phase shimming at the location of the prostate. A single-slice transversal T2-weighted image at the mid-plane of the ERC was acquired with a short acquisition time (multi-slice-TSE, TSE factor 18, 90 degree flip angle, TE/TR=100/1000ms, 0.8x0.82x2 mm^3 voxel, 312x486 matrix size) to investigate the presence and location of the RF coupling between the external and internal elements that would appear as a signal void in a T2-weighted image. The location of the signal void with respect to the ERC was used to estimate the RF power needed for the ERC to generate a B_1 field at that location that would have been obtained with the external array without RF coupling. Dynamic series of T2-weighted transverse images (10 scans, transmit phase of ERC loop increased from 0 to 270 degrees in steps of 30 degrees) were acquired also at the mid-plane of the ERC to determine the optimal transmission phase that excludes the signal voids. Subsequent T2-weighted images (MS TSE, TSE factor 18, TE/TR=100,72/5000,2500 ms, 250x400x58 mm^3 FOV, 10 slices) were acquired for anatomy characterization by transmitting with all elements including the ERC with the active decoupling amplitude and phase settings. Reception was obtained with all elements. Subsequently, the strongest B_1 level, constructively interfered at the prostate, rather than the most uniform one was chosen for the MRSI with the maximum peak power allowed per channel. In-vivo MR spectroscopy measurements were acquired with a 2D nsLASER sequence (8), TE/TR= 56/3600 ms, 100x35 mm FOV, 30x300 VOI, 5x5x5 voxel, 20x70 matrix, 2048 samples,

4000 Hz bandwidth, 1 NSA and a VAPOR pre-pulse with a 150 Hz window for additional water suppression. B_1 maps were acquired with the dual TR method for measuring the actual flip angle (11) (3D FFE, $TE/TR_1,TR_2$ = 2.6/25, 125 ms, 50 degree flip angle, 350x200x25mm^3 FOV, 148 x 40 matrix size, 5 slices) in two of the patients with ERC transmission to assess the maximum B_1 over the prostate. Besides the minimal coupling and SAR validations previously obtained (7), additional temperature measurements were performed on one of the patients for safety assessment of the combined setup. A fiber optic temperature probe (Luxtron, Santa Clara, CA, USA, m3300 Biomedical Labkit) was located on top of one of the capacitors of the ERC which is known to have the highest temperature increase (7). Temperature measurements were recorded during the whole prostate examination.

3.3 Results

3.3.1 Phantom Measurements

Measurements on the torso phantom with one SiSiAD antenna and the ERC showed no detectable RF coupling between the elements as observed from the gradient echo images when transmitting with either the SiSiAD antenna only or ERC loop only, while receiving with all elements. Power transmission measurements (S_{12}) obtained with the smaller phantom (Figure 3.1 a) in the maximum coupling situation when tilting the elements, resulted in a -13 dB coupling between the ERC and the SiSiAD elements. Transmission with the single SiSiAD antenna showed several transition bands in the FFE image, not only close to the antenna itself, but also in the vicinity of the ERC, reflecting the coupling between the elements (Figure 3.1 c). By defining the location of the furthest signal void from the element as a 180 degree pulse, the corresponding B_1 amplitude can be assessed (i.e. 3 mT as defined by the MR system). Using the B_1^+ map available for the dual-element ERC (7) (Figure 3.1 b), 40 mT can be generated with 800 W at the location of the furthest signal void observed, that corresponded to the nominal 180 degree flip angle. Therefore, to counteract the RF coupling caused by the SiSiAD on the ERC at this location, about 5 W peak power is needed to generate the same 180 degree pulse if the peak B_{1max} is set to 3 mT (maximum B_1^+ set for the SiSiAD) for the dual-element ERC. The simultaneous transmission of a nominal 180 degree pulse with the SiSiAD and the ERC (i.e. with the estimated power to counteract the RF coupling and the manually found

optimal phase for the loop coil) showed that active decoupling is possible during transmit (Figure 3.1 d). Note however, that the coupling during reception is still visible as a signal intensity increase close to the ERC. Steering the phase of the second element of the ERC showed no influence in the RF coupled field.

3.3.2 In-vivo Measurements

Figure 3.2 shows the differences between acquiring T2-weighted images when transmission is done with the SiSiAD elements without active decoupling (Figure 3.2 a), with the actively decoupled ERC (Figure 3.2 b) and when transmitting with the ERC at maximum allowed power (Figure 3.2 c). The strong B1+ amplitudes achieved by the ERC (Figure 3.2 c) led to a total degradation of the T2-weighted image due to the transition bands created. Figure 3.2 a) shows the full field of view T2-weighted image that can be obtained by transmitting with the SiSiAD array and without active decoupling. An RF coupling spot at the right side of the prostate (white arrow) is observed and it corresponds to a nominal 180 degree flip angle. As the nominal 90 degree flip angle of the T2-weighted image was obtained with a B_{1max} of 10 mT, it is deduced that the 180 degree flip angle was made with a B_{1max} of 20 mT. From the B_1^+ map information, about 90 mT can be achieved with the ERC at 800 W peak power at the location of the 180 degree flip angle. Therefore, just 10 W peak power (i.e. 80-fold lower than what the ERC can generate at that location) would be needed to obtain the additional 90 degree to make up the 180 degree flip angle (i.e. one transition band, 90 degree flip angle with the external array + 90 degree flip angle with the ERC) at that location. The decoupling protocol for the in-vivo measurements was obtained with an amplitude equivalent to 10 W for transmission with the ERC and a varying phase (Figure 3.3 a-j). The white arrows point at the location of the signal void caused by RF coupling. By varying the ERC phase, steering of the RF decoupled field was possible. The phase setting where no RF coupling was observed was used to continue the scanning protocol. Homogeneous T2-weighted images can be obtain with this active decoupling protocol, as shown in Figure 3.2 b. Notice that the hypo-intensity on the right side of the prostate corresponded to tumor presence.

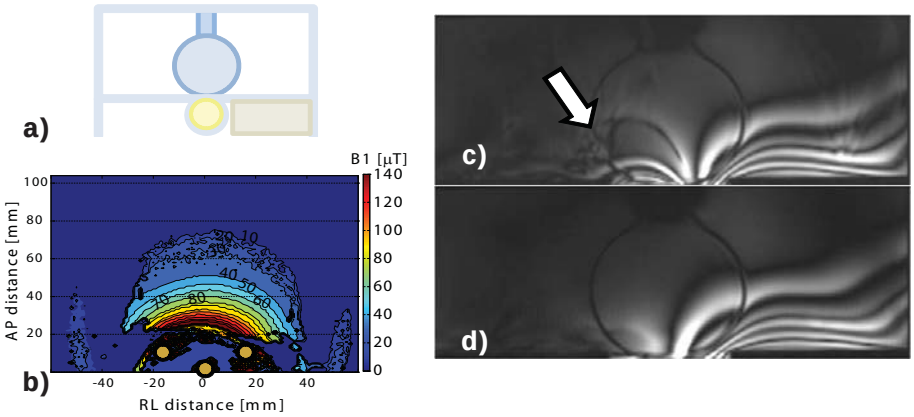

Figure 3.1: Measurements on the smaller phantom. Transverse view of the schematics of the smaller phantom (square and flask inside) with the positioning of the ERC (yellow circle) and the SiSiAD antenna (brown block) is shown on a). The B_1^+ map of the double-element ERC (7) on b) was obtained with a peak power of 800 W per channel and it is used to estimate the power to counteract the coupling field. On c), the coupling field generated by the ERC when transmitting only with the antenna at a nominal B_1 of 3 mT is indicated with the white arrow. On figure d) the SiSiAD antenna B_1 field pattern is restored without coupling field contributions from the ERC after amplitude and phase optimization for the active decoupling. Note in this last figure that the high intensity is caused by the coupling still present during signal reception.

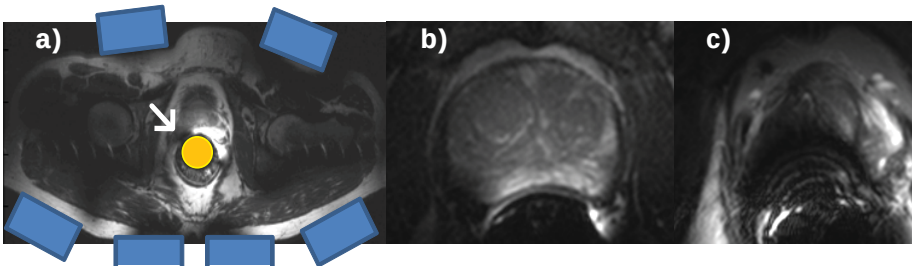

Figure 3.2: T2-weighted images a) showing the positioning of the SiSiAD antennas (blue blocks) on the pelvic region and the ERC (yellow circle) inside the rectum. In addition, RF coupling is observed when transmission is done with the external SiSiAD antennas and reception with all elements (white arrow); b) obtained with uniform B_1 when transmission is done with the external array and the actively decoupled ERC, note the hypo-intense region on the lower right of the prostate matching the tumor location and c) non-uniform B_1 when including transmission with the ERC at maximum power, while reception is obtained with all elements. Notice the degradation of the image in c) due to the transition bands created by the strong non-uniform B_1 amplitudes achieved with the ERC in the prostate.

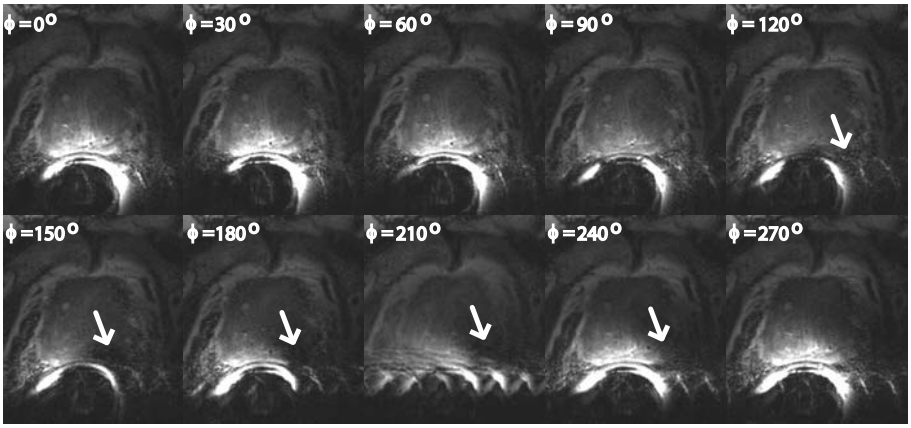

Figure 3.3: Active decoupling scheme obtained with a T2-weighted image across the middle plane of the ERC in the transverse plane. A series of 10 scans were obtained varying the phase of the ERC from 0 to 270 degrees in steps of 30 degrees. The white arrows point at the locations where RF coupling is observed between the external and the internal elements. By steering the phase of the ERC the location of the RF coupling can be removed from the prostate location.

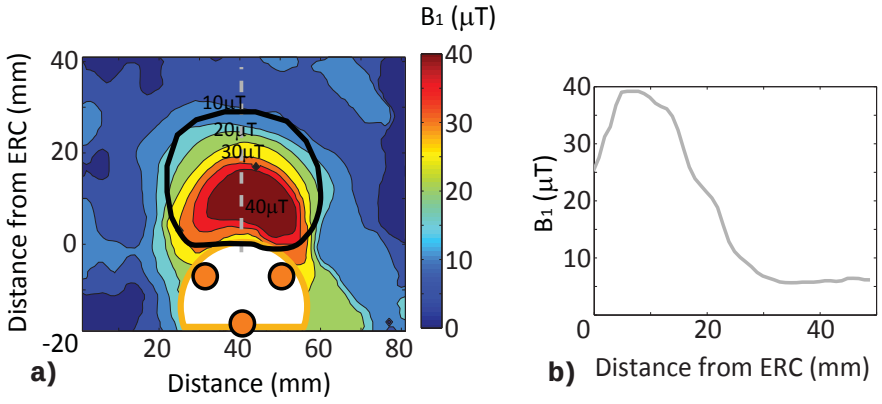

Figure 3.4: B_1 map obtained in-vivo with the combined setup (external radiative elements with internal ERC) when transmission is done with all elements at maximum amplitude (a, b) and reception is obtained with all elements. The orange dots at the bottom of the B_1 map represent the position of the ERC (upper two: loop coil, bottom: stripline) close to the prostate (contoured in black) and the dashed gray line shows the position for the profile shown in c), plotted at the mid plane of the ERC. The inclusion of the SiSiAD antennas during Tx contributes to the B_1 continuity at the anterior limits of the prostate.

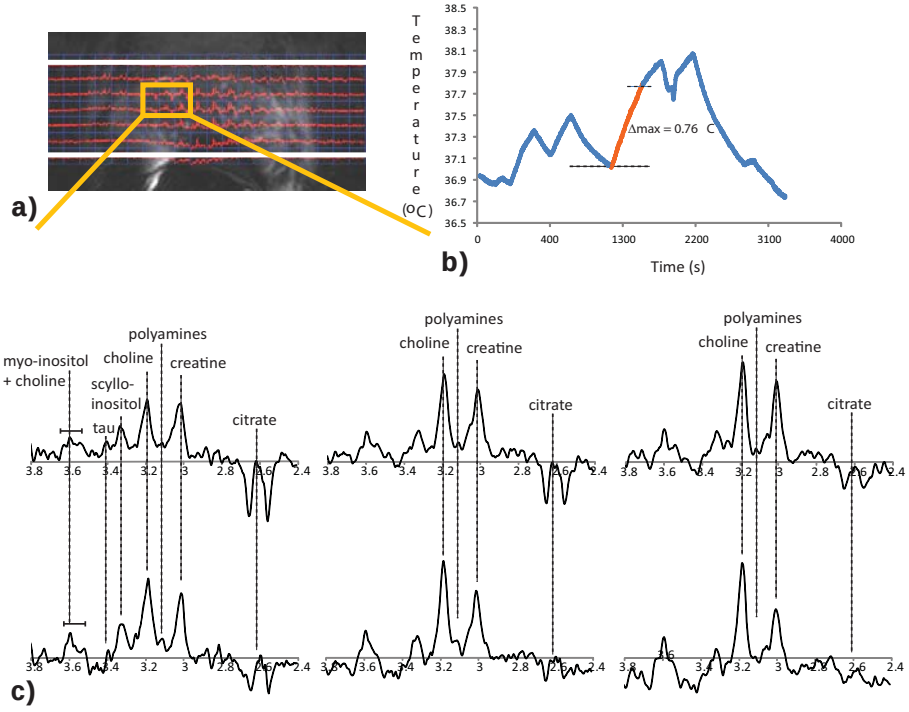

Figure 3.5: a) T2-weighted image of the prostate showing the positioning of the CSI grid for MRSI measurements on c). b) Temperature measurements were obtained during the whole examination protocol, with a fiber optic temperature probe at the location of the hottest spot on the ERC, showing a maximum temperature rise of less than 1 degree Celsius during the MRSI acquisition as expected.

The maximum B_1^+ available when constructively transmitting with all elements at maximum RF peak power is shown for one patient in Figure 3.4 a) with a profile obtained in the mid line of the ERC (Figure 3.4b). Notice the continuity of the B_1^+ amplitudes to the anterior limit of the prostate (delimited by the black contour), which is caused by the SiSiAD antennas contribution. With this configuration of maximized B_1, the MRSI measurements were obtained in-vivo at an echo time of 56 ms (Figure 3.5 a, c). MRSI signals from uniform flip angles over the whole ERC coverage are observed due to the adiabatic nature of the nsLASER sequence. Signals from choline (3.2 ppm), creatine (3.0 ppm) and citrate (2.6 ppm) are visible, while the signal from polyamines (at 3.1 ppm) are absent, suggesting tumor tissue. Due to the relatively short echo time of the nsLASER sequence (TE = 56 ms) other metabolite signals can be

observed such as myo-inositol (mI at 3.6 ppm), taurine (tau at 3.4 ppm) and scyllo-inositol (scI at 3.3 ppm) which have short T2-relaxation times and are generally not visible at longer echo times. The recorded temperature measurements showed a maximum temperature rise during the nsLASER execution of less than 1 degrees Celsius (Figure 3.5 b).

3.4 Discussion

The RF coupling between an external array of antennas and an endorectal coil at 7T is already known to be low, as shown by *Metzger et al. 2010* (9). Therefore, RF safety will not be limited by the minimally coupled ERC, hence making the exploration of the combination of a SiSiAD array (10) and a dual-element ERC (7) without the use of PIN-diode decoupling possible. Without PIN-diodes inclusion, the ERC could also be used for transmission during the MRSI examinations, where high B_1^+ amplitudes are beneficial for obtaining broad-banded adiabatic RF pulses and relatively short echo times.

The acquisition of good quality T2-weighted MR images was possible with the combined setup of external and internal elements using active decoupling as shown in this investigation. While the presence of the ERC during signal reception aids the external array for obtaining a high SNR, the external array assists the ERC by extending the B_1 field. When transmitting with all elements at maximum allowed power for the MRSI measurements with constructive interference at the prostate location, the coverage of high B_1^+ amplitudes achieved in the prostate was extended beyond the prostate limits in the anterior direction, as found from the B_1^+ maps obtained in-vivo. This is particularly useful for obtaining MRSI in the relatively large prostates in patients.

The phantom measurements obtained with one SiSiAD element and the ERC successfully showed the proof of principle of active decoupling, even in extreme RF coupling conditions. The combined SiSiAD and ERC setup showed a low RF coupling between the external and internal elements on prostate cancer patients in-vivo with respect to the coupling in the small phantom. With respect to safety, the observed low RF coupling during the MR imaging, increased the local SAR closest to the ERC by just a fraction of the SAR guidelines, which is equivalent to less than 2% of the necessary power to reach the maximum local SAR of 10 W/kg (12). As important, when transmission is done with the SiSiAD array the maximum local SAR is far from the prostate area (13). Consequently, even when the

ERC is not decoupled, the maximum local SAR is not increased by the ERC. The low local SAR increase due to the RF coupling was corroborated by the temperature measurements obtained on top of the capacitor known to generate the highest temperature increase when transmitting with the ERC (7). This measurement remained below 1 degree Celsius for all scans including the MRSI acquisition.

Although the RF power coupling (S_{12}) between the SiSiAD elements and the ERC is almost non-existent, as expected from the high tissue load, this can still cause field distortions. Nevertheless, these distortions can be corrected using an active decoupling protocol to determine the power and phase necessary to counteract the RF coupling field. The active decoupling protocol required a short adjustment time to find the right counteracting parameters. Consequently, PIN-diode decoupling can be avoided, which helps minimizing the components inside the ERC housing, hence its dimensions and patient discomfort during the ERC insertion. In addition, the ERC can be enabled as a transmitter making MRSI measurements with short TE and TR feasible at 7T within SAR guidelines.

3.5 Conclusion

This investigation has shown that active decoupling can be an effective alternative to PIN-diode decoupling. Using a minimum adjustment time to match the amplitude and phase of the coupled fields of an endorectal coil (ERC) with an external array at 7T, the coupling can be counteracted. With this approach a uniform B_1 field can be provided in the prostate when using the actively decoupled ERC, while improving the SNR during reception. In the same scan session strong B_1 fields can be obtained when using the ERC as a transceiver. In addition, by avoiding PIN-diodes, the components and dimensions of the ERC are minimized and no switching times for driving the PIN-diodes are needed.

Using an actively decoupled ERC as a transceiver combined with an external transceiver array, provides the means to enable sensitivity maximization of MRI combined with efficient MRS of the prostate at 7T.

REFERENCES

1. Heerschap A, Jager GJ, Van Der Graaf M, Barentsz JO, De La Rosette

JJMCH, Oosterhof GON, Ruijter ETG, Ruijs SHJ. In vivo proton MR spectroscopy reveals altered metabolite content in malignant prostate tissue. Anticancer Research 1997;17(3 A):1455-1460.

2. Kurhanewicz J, Vigneron DB, Nelson SJ, Hricak H, MacDonald JM, Konety B, Narayan P. Citrate as an in vivo marker to discriminate prostate cancer from benign prostatic hyperplasia and normal prostate peripheral zone: Detection via localized proton spectroscopy. Urology 1995;45(3):459-466.

3. Scheenen TWJ, Fütterer J, Weiland E, van Hecke P, Lemort M, Zechmann C, Schlemmer H-P, Broome D, Villeirs G, Lu J, Barentsz J, Roell S, Heerschap A. Discriminating Cancer From Noncancer Tissue in the Prostate by 3-Dimensional Proton Magnetic Resonance Spectroscopic Imaging. Investigative Radiology 2011;46(1):25-33.

4. Shukla-Dave A, Hricak H, Moskowitz C, Ishill N, Akin O, Kuroiwa K, Spector J, Kumar M, Reuter VE, Koutcher JA, Zakian KL. Detection of Prostate Cancer with MR Spectroscopic Imaging: An Expanded Paradigm Incorporating Polyamines. Radiology 2007;245(2):499-506.

5. Metzger GJ, Snyder C, Akgun C, Vaughan T, Ugurbil K, Moortele P-FVd. Local B1+ shimming for prostate imaging with transceiver arrays at 7T based on subject-dependent transmit phase measurements. Magnetic Resonance in Medicine 2008;59(2):396-409.

6. van den Bergen B, van den Berg CAT, Klomp DWJ, Lagendijk JJW. SAR and power implications of different RF shimming strategies in the pelvis for 7T MRI. Journal of Magnetic Resonance Imaging 2009;30(1):194-202.

7. Arteaga de Castro CS, van den Bergen B, Luijten PR, van der Heide UA, van Vulpen M, Klomp DWJ. Improving SNR and B1 transmit field for an endorectal coil in 7 T MRI and MRS of prostate cancer. Magnetic Resonance in Medicine 2012;68(1):311-318.

8. Arteaga de Castro CS, Luttje MP, van Vulpen M, Luijten PR, van der Heide UA, Klomp DWJ. Composite slice-selective adiabatic excitation for prostate MRSI. NMR in Biomedicine 2013;26(4):436-442.

9. Metzger GJ, van de Moortele P-F, Akgun C, Snyder CJ, Moeller S, Strupp J, Andersen P, Shrivastava D, Vaughan T, Ugurbil K, Adriany G. Performance of external and internal coil configurations for prostate investigations at 7 T. Magnetic Resonance in Medicine 2010;64(6):1625-1639.

10. Raaijmakers AJE, Ipek O, Klomp DWJ, Possanzini C, Harvey PR, Lagendijk

JJW, van den Berg CAT. Design of a radiative surface coil array element at 7 T: The single-side adapted dipole antenna. Magnetic Resonance in Medicine 2011;66(5):1488-1497.

11. Yarnykh VL. Actual flip-angle imaging in the pulsed steady state: A method for rapid three-dimensional mapping of the transmitted radiofrequency field. Magnetic Resonance in Medicine 2007;57(1):192-200.

12. The International Commission on Non-Ionizing Radiation P. Medical Magnetic Resonance (MR) Procedures: Protection of patients. Health Physics 2004;87(2):197-216.

13. van den Bergen B, Klomp DWJ, Raaijmakers AJE, Arteaga de Castro C, Boer VO, Kroeze H, Luijten PR, Lagendijk JJW, van den Berg CAT. Uniform prostate imaging and spectroscopy at 7 T: comparison between a microstrip array and an endorectal coil. NMR in Biomedicine 2010;24(4):358-365.

CHAPTER 4

Composite slice selective adiabatic excitation for prostate MRSI

NMR in Biomed. 26(4): 436-442

Abstract

Higher magnetic field strengths like 7 Tesla offer increased spectral resolution and higher SNR. These properties can be very advantageous for MRSI. Particularly, signals that generally overlap at lower fields, like choline, polyamines and creatine, can be resolved at 7T. However, higher magnetic field strengths suffer from strong RF field non-uniformities. These non-uniformities become even stronger when using surface transceivers, such as an endorectal coil for prostate imaging. In order to obtain uniform excitations for accurate MRSI measurements, adiabatic sequences are therefore recommended. Conventional adiabatic MR spectroscopy sequences (i.e. Localization by Adiabatic and Refocusing, LASER) have relatively long echo times (TE), especially when optimized to measure the strongly coupled spins of citrate in the prostate. The semi-LASER sequence (sLASER) has a significantly shorter TE, although it does not provide adiabatic excitation. Therefore, we propose an adiabatic sLASER sequence that either has a composite adiabatic slice selective excitation (cLASER) or a non-slice selective adiabatic excitation (nsLASER), allowing for shorter echo times, while maintaining the adiabatic spin excitation. Furthermore, the spatial properties of the composite adiabatic excitation allow for a high slice excitation bandwidth resulting in negligible chemical shift displacement artifacts. Exclusion of the slice selection can be considered once the field of view extends beyond the transmit field of the RF coil. The use of a transceiver at high magnetic field strengths has shown that the cLASER and nsLASER sequences are suitable for MRSI of the prostate both in phantom and in-vivo validations.

4.1 Introduction

Magnetic resonance imaging (MRI) techniques are sensitive for detecting prostate cancer. Although their specificity is still limited even when several MRI modalities are combined (e.g. T2-weighted MRI with dynamic contrast enhanced MRI) (2). Nevertheless, the combination of MR techniques has proven to be useful in diagnosing and staging prostate cancer at 1.5 and 3 Tesla (2-7). One such technique, which offers the possibility of obtaining metabolic information from tissue, is magnetic resonance spectroscopy imaging (MRSI). In the case of the prostate, four low concentrated (few mM) metabolites (choline, polyamines, creatine and citrate) provide information about the aggressiveness or malignancy of a tumor. Detection of these markers has been proven to increase the specificity of the prostate cancer diagnostics (8). Typically, prostate cancer is associated with elevated (choline + creatine)/citrate ratios , when compared to benign lesions or normal tissue (9). Polyamines are also detectable metabolites found in prostate tissue. This coupled spin system resonates at 3.1 ppm in the MR spectrum and overlaps with choline (at 3.2 ppm) and creatine (at 3.0 ppm) at lower field strengths. As a result polyamine signals can be obscured. Higher field strengths can provide increased intrinsic signal to noise ratio (SNR) (10) and chemical shift dispersion thus allowing greater spectral resolution needed to resolve peaks that would normally overlap at lower field strengths (i.e. polyamines from choline and creatine). In-vivo prostate gland polyamine detection has been shown at higher field strengths (1).

Despite the aforementioned benefits, higher field strengths have intrinsic properties that can be detrimental for both MRI and MRSI. The use of external transmit coils does not provide sufficient B_1^+ strength at the deeply located prostate gland to obtain localized MRSI at short echo times (11,12). Internal endorectal coils (ERCs) used as transceivers are preferable due to their proximity to the organ in question. ERCs can boost B_1^+ values in the prostate, while maintaining highest sensitivity. Despite this, the homogeneity of the transmit field is still severely compromised due to the inherent properties of surface coils (11-13).

The high ERC B_1^+ strength results in an acceptably small chemical shift displacement artifact, even at 7 T. This makes the ERC useful for volume localization in MR spectroscopy. However, the intrinsic B_1 field non-uniformities associated with local transceivers, will result in non uniform spin excitations when using conventional (amplitude modulated

(AM)) RF pulses. To avoid this, adiabatic RF pulses, which are both amplitude (AM) and frequency modulated (FM) are preferable. These pulses result in uniform spin perturbations for the metabolites of interest even in the presence of B_1 field non-uniformities.

Localization by adiabatic selective refocusing (LASER) is an attractive adiabatic MR spectroscopy sequence (14,15). The LASER sequence consists of a non selective adiabatic half passage RF pulse (AHP) for excitation and three pairs (one pair for each direction) of adiabatic full passage (AFP) RF pulses for slice selective refocusing (Figure 4.1 a). The adiabatic nature of this sequence makes it insensitive to B_1 in-homogeneities. However, due to the large amount of relatively long RF pulses that it contains, the echo times tend to be long leading to signal reduction due to T2 relaxation effects. Particularly for the metabolite detection in the prostate, additional RF pulses are needed for water and lipid suppression (i.e. basing or MEGA (16)). In addition, inter-pulse timings need to be optimized for simultaneous and accurate detection of the strongly coupled spin system of citrate and the coupled system of polyamines. We recently showed that the optimum TE for the LASER sequence at 7 T is 159ms (17), compared to 56ms for the non-adiabatic semi-LASER (sLASER) sequence (1) (Figure 4.1 a and b respectively). The sLASER sequence has a shorter echo time due to its slice selective excitation which excludes the need for one pair of (adiabatic) refocusing pulses. However, the excitation pulse in the sLASER sequence is a conventional (AM only) RF pulse which is still sensitive to the B_1^+ field in-homogeneities making it sub-optimal in combination with an ERC transceiver. A preferable alternative would be to make the sLASER sequence completely adiabatic, taking advantage of the short echo time and the insensitivity to the non uniformities of the B_1^+ field.

Traditional adiabatic half passage RF pulses for excitation have asymmetric excitation profiles whose excitation bandwidths depend on the B_1 field strength. In addition, the frequency profile of an adiabatic excitation pulse has a poor stop-band performance preventing its use as a slice selective excitation pulse. Nevertheless, when using the ERC as a transceiver, the field of view (FOV) is already limited by the B_1 field created by the coil. This is especially true in the right-left (RL) direction, where the dimension of the coil is smaller than the prostate. The sensitivity of the coil beyond the RL boundaries of the prostate is very low suggesting that slice selection in the RL direction may be excluded as long as the field of view (FOV) of the chemical shift imaging (CSI) grid extends the field of view of the RF coil. This would enable the use of adiabatic non-selective pulses for excitation in the RL direction for MRSI. The increased

FOV would increase the scan duration which could be compensated by shortening the repetition time.

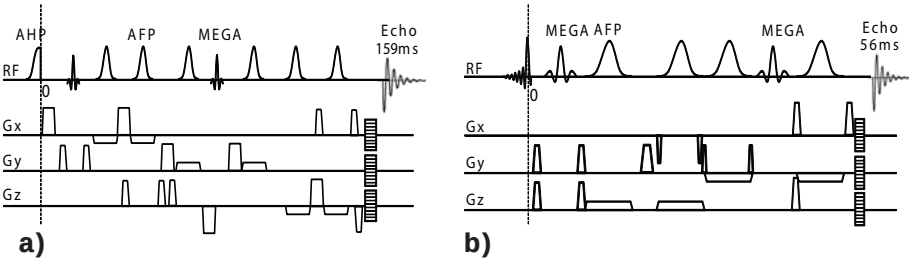

Figure 4.1: (a) Localization by adiabatic selective refocusing (LASER) MRSI sequence for volume localization. An adiabatic half passage (AHP) radiofrequency (RF) pulse is used for excitation and three pairs of adiabatic full passage (AFP) RF pulses are used for slice-selective refocusing in each (*x*, *y*, *z*) direction. Simultaneous water and lipid suppression is obtained with two Mescher–Garwood (MEGA) RF pulses. TE for the LASER sequence is 159 ms when optimized to obtain a fully absorptive signal from the strongly coupled system of citrate in the prostate gland (17). (b) Semi-LASER (sLASER) MRSI sequence for volume localization. The slice-selective excitation is achieved with a conventional RF pulse. Two pairs of AFP RF pulses are needed to refocus in the remaining two directions. Simultaneous water and lipid suppression is obtained with two MEGA RF pulses.

An alternative to reduce the scan duration would be to make the AHP RF pulse spatially selective using conventional spatially selective pulses. This can be achieved with composite RF pulses using conventional slice selective AM pulses, while varying the amplitudes and phases per pulse to describe the envelope of the AHP RF pulse. In this way an adiabatic spatially selective excitation pulse can be made with properties similar to that of the original AHP RF pulse. Slice selective properties are then determined by the RF pulses that comprise the composite pulse.

As a solution to obtain accurate volume selection, we propose two adiabatic sequences based on the sLASER sequence: the non-selective excitation LASER (nsLASER) and the composite excitation LASER (cLASER). The nsLASER sequence takes advantage of the spatial excitation properties of the ERC transceiver in the RL direction of the prostate which, in combination with a conventional adiabatic RF excitation pulse, requires minimal spatial oversampling. Therefore, the nsLASER enables artifacts free MRSI of the prostate when a relatively large FOV is used.

On the contrary, the spatially selective adiabatic excitation in the cLASER sequence enables a global reduction of the FOV thus providing adiabatic 3D localized MRSI within the prostate at acceptable acquisition times. The performance of both sequences is validated in phantoms and in patients with prostate cancer at 7 Tesla.

4.2 Methods

An adiabatic half passage RF pulse was used for the adiabatic excitation, with hyperbolic tangent (*tanh*) and tangent (*tan*) functions for the amplitude ($B_1(t)$) and the frequency ($\Delta\omega(t)$) modulations (equations [1] and [2] as well documented in the work of de Graaf et al. (18)). The parameters ξ and κ are adjustable variables that modulate the shape of the *tanh* and *tan* functions. T is the pulse duration and t is the dwell time. In our case, the parameters used for these functions were ξ=10, κ=1.52, T=5 ms, t=0.1 ms and $\Delta\omega=20\pi$ [10^3 rad s^{-1}].

The adiabatic excitation obtained at a minimum B_1 of 10μT resulted in an excitation bandwidth (FWHM) of 1 kHz. The limited field of view of the ERC, particularly in the RL direction where the prostate is larger than the size of the coil, made it possible to avoid additional localization. Under these conditions, two slice selections were applied in the non-selective LASER sequence (nsLASER): the anterior-posterior (AP) and feet-head (FH) directions (Figure 3.2 c). To validate the spatial selection properties of the ERC transceiver, 2D MRSI was performed in patients with prostate cancer with an extended FOV in the RL direction (i.e. RLxAPxFH = 150x50x5 mm^3).

The excitation pulse can be made slice selective in order to achieve a fully controllable 3D volume selection sequence without relying on the localization properties of the ERC. This was accomplished by designing a 2D adiabatic RF pulse for excitation (i.e. spatially selective adiabatic pulse (19)) where the spectral part reflects the adiabatic properties. The same adiabatic half passage RF pulse for excitation used in the nsLASER was made in a composite way (cLASER). The composite envelopes (i.e. AM and FM) resembled the adiabatic excitation pulse and each segment provided a conventional slice selective RF pulse. The AM and FM shapes of the excitation pulse were divided in 17 segments. On each segment of the AM part, a single lobe sinc pulse of 0.3 ms duration was used.

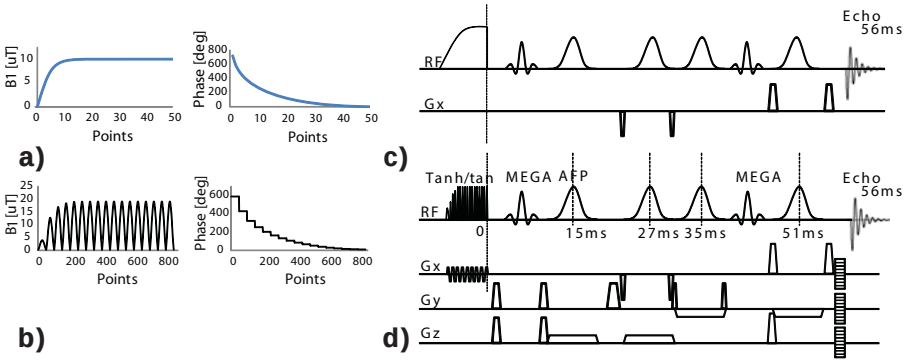

Figure 4.2: Continuous (a) and discrete (b) amplitude-modulated (AM) and phase-modulated (PM) shapes of the adiabatic half passage (AHP) (tanh/tan) radiofrequency (RF) pulse for excitation. Every segment of the composite AM shape in (b) corresponds to a 0.3-ms sinc pulse without zero crossings. The amplitude of each sinc was doubled to achieve the same area under the curve as the original (continuous) AM function. A total of 17 sinc RF pulses was used and resulted in a 5.1-ms composite RF pulse. The PM shape in (b) was kept constant during each sinc element, but changed discretely following the original phase modulation in (a). Schematics of the nonselective localization by adiabatic selective refocusing (nsLASER) sequence with the nonselective adiabatic excitation RF pulse and the composite LASER (cLASER) sequence with composite slice-selective excitation are shown in (c) and (d), respectively. Mescher–Garwood (MEGA) pulses (1) were used in both sequences for simultaneous water and lipid suppression. Two pairs of adiabatic full passage (AFP) RF pulses were used to refocus the magnetization in two directions to obtain a bar (nsLASER) or volume (cLASER) selection. TE was optimized to obtain a fully absorptive signal from the strongly coupled system of citrate and the coupled polyamine spin system at 7 T, resulting in 56 ms for both sequences.

The area under each sinc pulse was set to the same area under the curve of the corresponding segment on the original AM shape of the tanh/tan RF pulse. Consequently, the amplitude of each sinc was almost doubled, reaching maximum amplitudes close to 20μT. The frequency modulation component of the composite pulse was set by modulating the phase of each pulse segment. The phase modulation of the composite pulse was achieved via phase steps while keeping the phase constant over the duration of each sinc pulse. Modulating this way resembles the same phase change observed on the original tanh/tan pulse over the same interval corresponding to each sinc lobe. In the case of the cLASER sequence bipolar gradients were used for slice selection. To accommodate

the gradient slopes, a 0.1ms gap was left between each sinc pulse of the composite excitation resulting in an overall pulse duration of 6.6ms. The final composite shapes are shown in Figure 3.2 b and the resulting sequence in Figure 3.2 d.

Pulse performances were simulated using TopSpin 3.0.b.8 (Bruker Biospin GmbH, Germany) for both the original and the composite tanh/tan shapes. The B_1 dependency was obtained from the RF profile simulations for each pulse. The performances of the original and composite versions of the tanh/tan RF pulses were compared. Spatial profiles of the composite excitation were simulated using MATLAB (MATLAB 7.11.0, The MathWorks Inc., Natick, MA, 2010) for different offset frequencies and different B1 levels. These profiles were compared to the sLASER excitation spatial selection profile on resonance.

A whole body 7T MR system (Philips Healthcare, Cleveland, OH, USA) was used. All sequences were first tested on a phantom with a uniform B_1 field using a volume RF head coil (NOVA Medical). A phantom bottle filled with mineral oil was used to investigate pulse performance. Volume of interest (VOI) localization, B_1 signal dependency and chemical shift displacement artifacts (CSDA) were investigated using this phantom. The carrier frequency of the excitation pulses was set at a 0.6 ppm difference from the water frequency (4.7 ppm) to obtain the CSDA between choline and citrate. The B_1 was varied from 10 to 20μT to test the adiabatic condition of the adiabatic pulses.

A prostate phantom was used to validate sequence performance with respect to detection of the coupled metabolites in the prostate using the ERC. This phantom consisted of a mixture of prostate metabolites specified by the recipe described in the work of van der Graaf et al. (20). This spherical phantom was placed inside a container with 3.4 g/L salt to resemble the appropriate loading conditions for the ERC. The performance of the nsLASER and cLASER was compared with the performance of the sLASER sequence. MRSI parameters for all sequences were TE/TR = 56/3000ms, 8x8 matrix, voxel size 5x5 mm^2.

The sequences were validated in-vivo in two prostate cancer patients. Both patients were scanned at 7 Tesla using the double-element ERC (13). Image based second order B_0 shimming was applied. RF power calibration was done to obtain 20μT at 3.5 cm from the dual element ERC (13). The cLASER was compared to the sLASER in one patient using a FOV of 50x30x36 mm^3, 10x6x6 matrix, 2048 samples and TE/TR = 56/2500 ms. The nsLASER was performed on the second patient using a FOV of

150x50x5 mm^3, 30x10x1 matrix, 2048 samples and a TE/TR = 56/2000 ms.

4.3 Results

Figure 4.3 shows the excitation performance as function of B_1 (RF profiles), obtained for the conventional and composite versions of the adiabatic half passage tanh/tan RF pulse. The minimum B_1 to reach the adiabatic condition of the original and composite versions of the RF pulse can be obtained from these RF profiles. The lower limit of B_1 to fulfill the adiabatic condition resulted in 3 and 6 μT for the original and composite versions respectively. At this B_1 level, the excitation bandwidth (BW) is only 200Hz at FWHM for the composite pulse (Figure 4.3 b), which is just sufficient to excite all the metabolites of interest (3.2-2.5 ppm). At higher B_1 levels (i.e. 10 μT for the original pulse) the bandwidth was increased to 1 kHz (FWHM). In order to obtain the same effective area under the curve and same flip angle as with the conventional amplitude modulation at this B_1^+ level (10 μT), a B_1 of 18.7μT had to be chosen for the composite version of the pulse. The excitation profiles with respect to the chemical shift obtained with 10 and 18.7 μT for the original and the composite versions of the tanh/tan pulse are shown in Figure 4.3 c). Note that even at this higher B_1 level, the BW is still relatively small so the water and lipids signals were only partially excited.

The RF profile simulations with different offsets are shown in Figure 4.4. The minimum and maximum offsets were chosen to be -300 to 300 Hz (approximately twice the chemical shift between choline and citrate). The behavior of the composite pulse at different B_1 levels was investigated within this range of offsets. For values lower than 9 μT, the pulse did not reach the adiabatic condition over the entire frequency range, while at relatively high B_1 levels (i.e. close to the coil conductors where B_1 >30 μT) the pulse profile remained flat over 2 ppm (600 Hz) chemical shift.

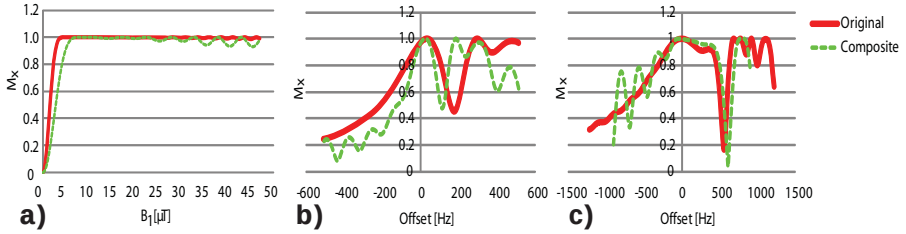

Figure 4.3: (a) Radiofrequency (RF) profile simulations of the original and composite versions of the tanh/tan RF pulse. The simulation shows the spectral performance of the pulses for different B_1 amplitudes. The continuous red line corresponds to the simulation of the original RF pulse and the green broken line to the composite pulse. As seen from (a), the minimum values to reach the adiabatic condition are 3.5 and 6 μT for the original and composite pulses, respectively. The adiabatic range of the composite pulse is reduced (6 to 30 μT) when compared with the original pulse (3 to 50 μT). For both RF pulses, the minimum B_1 value results in insufficient bandwidth to excite all the metabolites of interest (b). (c) The spectral profiles are simulated using 10 and 18 μT for the original and composite versions of the tanh/tan RF pulse, respectively. At these chosen B_1 amplitudes, both RF pulses have approximately the same effective area under the curve. The resulting bandwidth at half-maximum is approximately 1 kHz for both RF pulses. This bandwidth is sufficient to excite all the metabolites of interest.

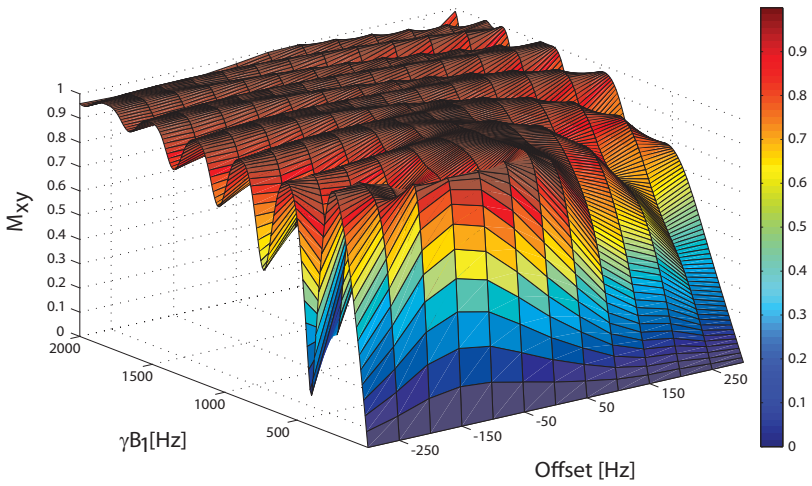

Figure 4.4: Radiofrequency (RF) profile simulations of the composite localization by adiabatic selective refocusing (cLASER) excitation pulse for different frequency offsets and B_1 levels. At elevated B_1 values [$\gamma B_1 > 1400$ Hz (32 μT)], which are generated in the prostate close to the endorectal coil (ERC), the behavior of the composite pulse remains within less than 10% variation in the available magnetization M_{xy}.

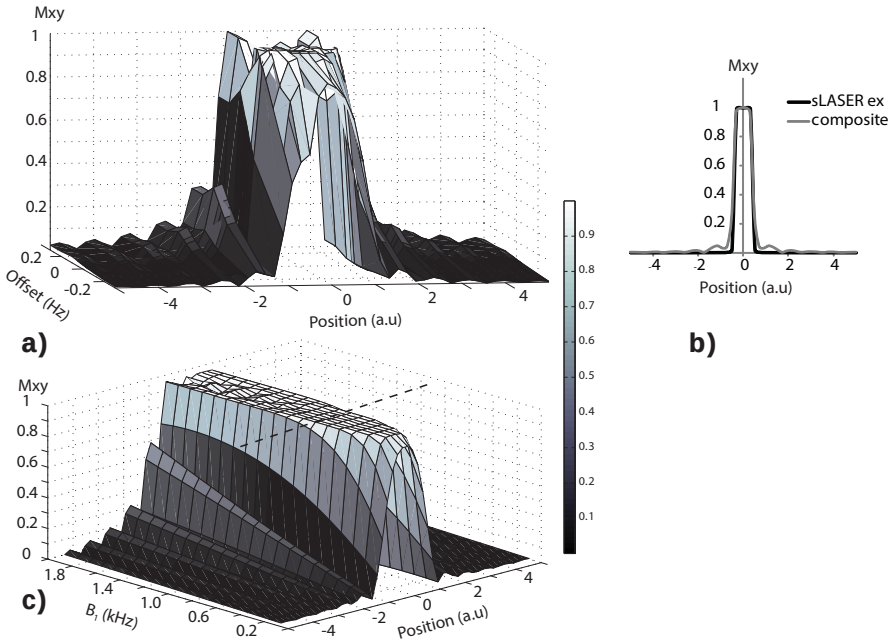

Figure 4.5: (a) Spatial profiles of the composite radiofrequency (RF) pulse simulated for different frequency offsets (−300 to 300 Hz) at a B_1 of 18 μT. At offset frequencies larger than 200 Hz, the selectivity profile of the composite RF pulse is compromised. Simulation on-resonance of the spatial profiles for the semi-localization by adiabatic selective refocusing (sLASER) excitation pulse and the composite pulse is shown in (b). The stop-band performance of the cLASER excitation is less optimal relative to sLASER excitation when assuming a uniform B_1. (c) The selection profiles for different B_1 values are simulated to demonstrate the uniformity over the slice selection. The broken line in (c) indicates the location of the nominal B_1 value (18 μT) used for the composite excitation pulse.

The slice selection variability over varying B_1 can be extracted from Figure 4.5 c. The dashed line on the graph indicates the 18mT nominal B_1 value used for the composite pulse. The slice selection remains stable for B_1 values up to about 40mT.

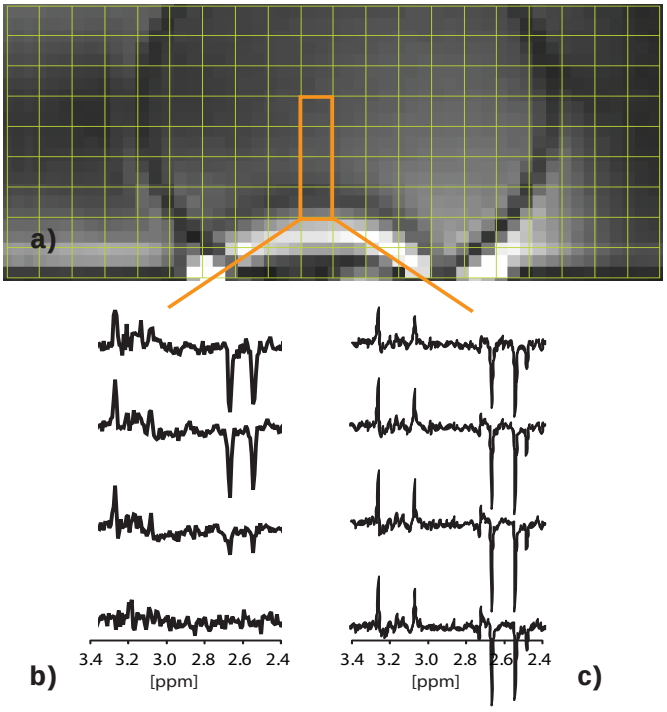

Figure 4.6: Measurements on the two-compartment phantom showing the appearance of transition bands in the gradient echo images reflected by deviations from the actual flip angle compared to the nominal angle of 90° (a). These deviations lead to signal degradations in the voxels obtained with the conventional (non-adiabatic) semi-localization by adiabatic selective refocusing (sLASER) sequence (b). These signal degradations (voids) are absent in the corresponding voxels obtained with the (adiabatic) composite LASER (cLASER) (or nonselective LASER, nsLASER) sequence (c).

Measurements on the bottle phantom revealed 1% CSDA between choline and citrate on the right-left direction when using the cLASER sequence. On the anterior-posterior direction, which corresponded to the slice selective refocusing direction the CSDA was 9%. In the case of the sLASER a 7.4% CSDA was found for the excitation pulse on the left-right direction. At the location corresponding to twice the nominal flip angle (i.e. at the black bands on the gradient echo image obtained with the same nominal flip angle settings of 90 degrees, Figure 4.6 a, b) the conventional excitation RF pulse from the sLASER resulted in no signal in the spectrum and variable values throughout the field of view due to the

B_1-dependency of the sLASER excitation. These B_1^+ dependencies were absent when using the adiabatic cLASER (or nsLASER) sequence (Figure 4.6 c).

In-vivo 2D and 3D MRSI results obtained with the nsLASER, cLASER and sLASER sequences are shown in Figure 4.7. Due to the fully adiabatic nsLASER and cLASER sequences it was possible to obtain spectra with uniform spin perturbation over the entire prostate. The highlighted spectra of a non-suspicious area (normal intensity on the T2-weighted image) in Figure 4.7 e show fully resolved resonances of choline, polyamines, creatine and citrate peaks obtained with the nsLASER on a 2D slice without lipids artifacts. On a different subject, a location is chosen where the actual B_1 field is close to the nominal B_1 field and no chemical shift displacement artifacts are expected. While B_0 shimming was less optimal in this patient, metabolite signals can be observed with the cLASER and the sLASER sequences (Figure 4.7 f). Dynamic alterations in B_0 shimming may have played a role due to the non uniformity of the B_1 field at this area. Nevertheless, the adiabatic behavior of the cLASER sequence showed a better performance and higher SNR compared to the sLASER results.

4.4 Discussion

Increased B_1 non-uniformities are found at higher magnetic fields (10) or when surface transceivers are used for MRI or MRSI (11,12,21). Such field non-uniformities can be a problem for quantified MRSI. The presented work shows that the uniform excitations with adiabatic RF pulses can be obtained at higher fields, hence facilitating reliable measurements and quantification of MRSI in patients with prostate cancer at 7T.

Two fully adiabatic sequences have been implemented for prostate MRSI. Both sequences were based on the LASER sequence (22) for localized MR spectroscopy. To decrease the number of RF pulses, the RF deposition and echo time, the excitation pulse can be modified. Using the nsLASER sequence, 2D localization with an adiabatic non-selective excitation RF pulse was possible. As a consequence, only two pairs of refocusing pulses were required. This implementation is analogous to that of the sLASER sequence (23) and reduces the minimum echo time to 56 ms when optimized for citrate detection. The limited coverage of the endorectal coil in the right-left direction, made it possible to use the

nsLASER for prostate MRSI and obtain in-vivo MR spectroscopy without spurious artifacts coming from water or lipids from tissue surrounding the prostate. MRSI results in-vivo showed distinct resonances of choline, creatine, citrate and also significant signal intensities of polyamines (3.1 ppm).

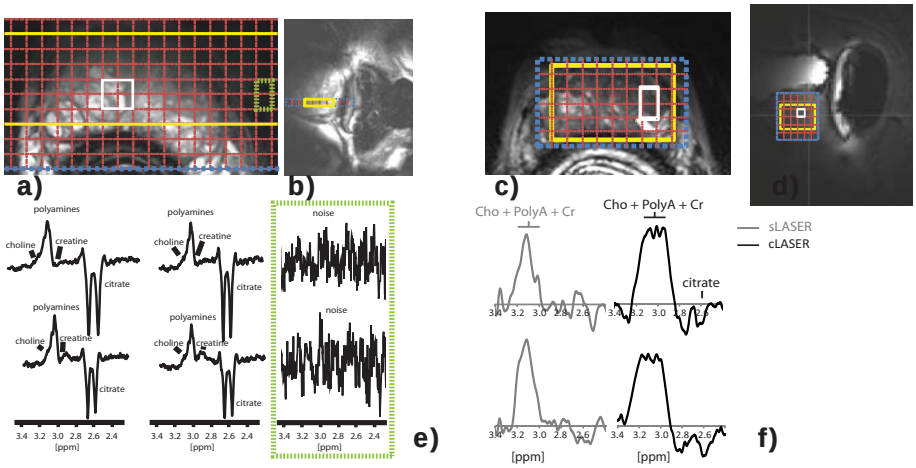

Figure 4.7: **In vivo** measurements on two patients with prostate cancer. Transverse $\mathbf{T}_2$-weighted images (a, c) and sagittal $\mathbf{T}_2$-weighted images (b, d) showing the volume of interest localization within the field of view (blue box) for the nonselective localization by adiabatic selective refocusing (nsLASER) and composite LASER (cLASER) (and semi-LASER, sLASER) measurements, respectively. Two-dimensional MRSI was acquired with the nsLASER sequence (TR/TE = 3000/56 ms; 24 x 8 matrix; 5 x 5 mm^2 voxel). Highlighted spectra from the white box in (a) are shown in (e). Frequencies of choline, polyamines, creatine and citrate can be resolved. Notice the absence of signal artifacts outside the prostate (green broken box), reflecting the spatial selection properties of the endorectal coil (ERC). Spectra from an apparent tumor region on a different subject [white box in (c) and (d) in the $\mathbf{T}_2$-weighted images), acquired with the cLASER (black) and sLASER (gray) sequences and scaled at equal noise levels, are highlighted in (f). Although $\mathbf{B}_0$ shimming was suboptimal in this patient, metabolite signals can be detected with both sequences. Notice the lower signal-to-noise ratio available from the sLASER spectrum, reflecting either a dynamic alteration of the $\mathbf{B}_0$ shimming or a potential mismatch of the flip angle caused by the non-uniform $\mathbf{B}_1$ field.

3D localized MR spectroscopy at the same short echo time of 56 ms was obtained with the cLASER sequence. A spatially selective adiabatic excitation RF pulse was implemented in a composite manner. This

pulse showed a chemical shift displacement artifact of only 1%. Due to the pulse segmentation, the composite pulse for excitation loses its adiabatic properties at lower B_1 values compared to the non-composite version. Therefore, it needs a higher B_1 to reach the adiabatic conditions when compared to the non-composite RF pulse. Nevertheless, using a local transceiver as the ERC, these B_1 levels can easily be obtained in the prostate (13). As only single-lobe sinc RF pulses were used on the composite segments, the stop band of the composite RF pulse is sub optimal when compared to the longer spatially selective RF pulse on the sLASER sequence. However, the use of the ERC made it possible to use the composite excitation with only a minimal oversampling. Furthermore, the slice profile of the composite excitation remains uniform when using the ERC. Phantom and in-vivo results using the cLASER showed the insensitivity to field in-homogeneities when compared to the sLASER sequence. This property of the cLASER sequence is particularly appreciated in areas where the actual flip angle is twice its nominal value.

Regarding SAR, for a comparable performance (i.e. B_1 = 18 mT for the composite pulse and 10 mT for the conventional adiabatic excitation) the composite pulse requires about 3.2 fold more RF power than the AHP on the nsLASER. However, most of the RF power is consumed by the broadband refocusing pulses. Hence, the increased SAR of the composite versus the conventional adiabatic excitation RF pulse is only 6.2%, therefore minimally affecting the choice of the minimum TR.

Since the echo time was not compromised, both the nsLASER and the cLASER sequences performed equal to the sLASER in areas where the actual flip angle corresponded to the nominal angle. When compared to a LASER sequence, the nsLASER and the cLASER sequences have a significantly lower TE and SAR.

4.5 Conclusions

Adiabatic sequences show superior performance in the presence of B_1 non-uniformities when compared to conventional RF pulse sequences. The combination of surface transceivers at higher field strengths like 7 Tesla with fully adiabatic sequences can provide excellent spin manipulation at very low CSDA even in the prostate. Exclusion of one pair of adiabatic refocusing pulses in a LASER sequence leads to shortened TE and reduced SAR, while spatial selection can be maintained by the RF coil itself or by using a spatially selective adiabatic pulse like the composite

adiabatic pulse for excitation. Combined with 3D spatial encoding the nsLASER and cLASER are good candidates to investigate the potential of high field MRSI in prostate cancer.

REFERENCES

1. Klomp DWJ, Scheenen TWJ, Arteaga CS, van Asten J, Boer VO, Luijten PR. Detection of fully refocused polyamine spins in prostate cancer at 7 T. NMR in Biomedicine 2010;24(3):299-306.

2. Ocak I, Bernardo M, Metzger G, Barrett T, Pinto P, Albert PS, Choyke PL. Dynamic Contrast-Enhanced MRI of Prostate Cancer at 3 T: A Study of Pharmacokinetic Parameters. Am J Roentgenol 2007;189(4):W192-201-W192-201.

3. Fütterer JJ, Heijmink SWTPJ, Scheenen TWJ, Jager GJ, Hulsbergen–Van de Kaa CA, Witjes JA, Barentsz JO. Prostate Cancer: Local Staging at 3-T Endorectal MR Imaging—Early Experience1. Radiology 2006;238(1):184-191.

4. Fütterer JJ, Heijmink SWTPJ, Scheenen TWJ, Veltman J, Huisman HJ, Vos P, de Kaa CAHV, Witjes JA, Krabbe PFM, Heerschap A, Barentsz JO. Prostate Cancer Localization with Dynamic Contrast-enhanced MR Imaging and Proton MR Spectroscopic Imaging1. Radiology 2006;241(2):449-458.

5. Hosseinzadeh K, Schwarz SD. Endorectal diffusion-weighted imaging in prostate cancer to differentiate malignant and benign peripheral zone tissue. Journal of Magnetic Resonance Imaging 2004;20(4):654-661.

6. Kozlowski P, Chang SD, Jones EC, Berean KW, Chen H, Goldenberg SL. Combined diffusion-weighted and dynamic contrast-enhanced MRI for prostate cancer diagnosis - Correlation with biopsy and histopathology. Journal of Magnetic Resonance Imaging 2006;24(1):108-113.

7. Sato C, Naganawa S, Nakamura T, Kumada H, Miura S, Takizawa O, Ishigaki T. Differentiation of noncancerous tissue and cancer lesions by apparent diffusion coefficient values in transition and peripheral zones of the prostate. Journal of Magnetic Resonance Imaging 2005;21(3):258-262.

8. Yu KK, Scheidler J, Hricak H, Vigneron DB, Zaloudek CJ, Males RG, Nelson

SJ, Carroll PR, Kurhanewicz J. Prostate Cancer: Prediction of Extracapsular Extension with Endorectal MR Imaging and Three-dimensional Proton MR Spectroscopic Imaging. Radiology 1999;213(2):481-488.

9. Koutcher JA, Zakian K, Hricak H, Garnick M, Stone N, Debruyne F, Moul J. Magnetic resonance spectroscopic studies of the prostate. Molecular Urology 2000;4(3):143-153.

10. Vaughan JT, Garwood M, Collins CM, Liu W, DelaBarre L, Adriany G, Andersen P, Merkle H, Goebel R, Smith MB, Ugurbil K. 7T vs. 4T: RF power, homogeneity, and signal-to-noise comparison in head images. Magnetic Resonance in Medicine 2001;46(1):24-30.

11. Metzger GJ, van de Moortele P-F, Akgun C, Snyder CJ, Moeller S, Strupp J, Andersen P, Shrivastava D, Vaughan T, Ugurbil K, Adriany G. Performance of external and internal coil configurations for prostate investigations at 7 T. Magnetic Resonance in Medicine 2010;64(6):1625-1639.

12. van den Bergen B, Klomp DWJ, Raaijmakers AJE, Arteaga de Castro C, Boer VO, Kroeze H, Luijten PR, Lagendijk JJW, van den Berg CAT. Uniform prostate imaging and spectroscopy at 7 T: comparison between a microstrip array and an endorectal coil. NMR in Biomedicine 2010.

13. Arteaga de Castro CS, van den Bergen B, Luijten PR, van der Heide UA, van Vulpen M, Klomp DWJ. Improving SNR and B1 transmit field for an endorectal coil in 7 T MRI and MRS of prostate cancer. Magnetic Resonance in Medicine 2011;DOI: 10.1002/mrm.23200.

14. Tannús A, Garwood M. Adiabatic pulses. NMR in Biomedicine 1997;10(8):423-434.

15. Norris DG. Adiabatic radiofrequency pulse forms in biomedical nuclear magnetic resonance. Concepts in Magnetic Resonance 2002;14(2):89-101.

16. Mescher M, Tannus A, Johnson MO, Garwood M. Solvent Suppression Using Selective Echo Dephasing. Journal of Magnetic Resonance, Series A 1996;123(2):226-229.

17. Arteaga CS, van der Heide UA, van Vulpen M, Luijten PR, Klomp DWJ. 1H MR Spectroscopy of the human prostate using an adiabatic sequence with a SAR optimized endorectal coil. 2010; Stockholm, Sweden. p 3502.

18. De Graaf RA, Nicolay K. Adiabatic rf pulses: Applications to In vivo NMR. Concepts in Magnetic Resonance 1997;9(4):247-268.

19. Balchandani P, Pauly J, Spielman D. Slice-selective tunable-flip adiabatic low peak-power excitation pulse. Magnetic Resonance in Medicine 2008;59(5):1072-1078.

20. van der Graaf M, Schipper R, Oosterhof G, Schalken J, Verhofstad A, Heerschap A. Proton MR spectroscopy of prostatic tissue focused on the detection of spermine, a possible biomarker of malignant behavior in prostate cancer. Magnetic Resonance Materials in Physics, Biology and Medicine 2000;10(3):153-159.

21. Metzger GJ, Snyder CJ, Akgun C, Adriany G. Comparison of transceive endorectal and external surface array coils for prostate imaging at 7 Tesla. 2008; Toronto, Canada. p 171-171.

22. Garwood M, DelaBarre L. The Return of the Frequency Sweep: Designing Adiabatic Pulses for Contemporary NMR. Journal of Magnetic Resonance 2001;153(2):155-177.

23. Klomp DWJ, Bitz AK, Heerschap A, Scheenen TWJ. Proton spectroscopic imaging of the human prostate at 7 T. NMR in Biomedicine 2009;22(5):495-501.

CHAPTER 5

Improved Efficiency on Editing Magnetic Resonance Spectroscopy of Lactate and GABA by Inclusion of FOCI Pulses at High Fields

NMR in Biomed. doi: 10.1002/nbm.2937

Abstract

GABA and lactate are metabolites which are present in the brain. These metabolites can be indicators of e.g. psychiatric disorders or tumor hypoxia respectively. Measurement of these weakly coupled spin systems can be done using MRS editing techniques, however, at high field strength this can be challenging. This is due to the low available B_1^+ field at high fields, which results in narrow bandwidth refocusing pulses and consequently, in large chemical shift displacement artifacts (CSDA). In addition, due to the increased CSDA and chemical shift dispersion, the efficiency of the MRS method is reduced, even when using adiabatic refocusing pulses. To overcome this limitation, frequency offset corrected inversion (FOCI) pulses have been suggested as a way to substantially increase the bandwidth of adiabatic pulses. In this study, a MEGA-sLASER editing sequence with refocusing FOCI pulses is presented for measurements of GABA and lactate in the human brain. Metabolite detection efficiency was improved by 20% and 75% for GABA and lactate respectively when compared to editing techniques that employ adiabatic RF refocusing pulses.

The highly efficient MEGA-sLASER sequence with refocusing FOCI pulses is an ideal and robust MRS editing technique for measuring weakly coupled metabolites at high field strengths.

5.1 Introduction

A large number of metabolites with high concentrations can be detected with proton MR spectroscopy. Metabolites with low concentrations can be measured as well when their resonance frequencies can be distinguished from overlapping resonances or metabolites with high concentrations. Some of these signals with low concentrations have demonstrated diagnostic potential. Good examples of such compounds are lactic acid (lactate) and γ-aminobutyric (GABA). Lactate is an end product of the anaerobic glycolysis pathway whose concentration can increase when the oxygen supply to tissues is low. Elevated lactate concentrations compared to normal tissue (1-4) have been measured in tumors. However, the lactate signal is obscured by either large lipids or macromolecules signals. GABA is an inhibitory neurotransmitter that has been linked to brain functionality and it can be associated with neurological and psychiatric disorders (5,6). However, the GABA signal overlaps with large creatine (Cr) and also with the macromolecular signals.

Several techniques to separate overlapping metabolites exist. Some of these techniques can be double quantum filters (7), 2D MRS (8,9), homonuclear transfer (10,11) or spectral editing (12,13). Weakly coupled (AX_n) spins in metabolites with low concentrations (e.g. GABA and lactate), which overlap with other resonances can be measured using MRS editing techniques (12,13). Using *J*-coupling differences between the different spin groups (A and X), both GABA and lactic acid can be separated from the overlapping signals. MRS editing techniques require at least two measurements; the first measurement selectively inverts one of the J-coupled spin groups which also affect the coupled group. The second measurement has no selective inversion. Ideally after subtraction of the two measurements, only the signal(s) that J-couple to the spin group that felt the selective inversion RF pulse are left on the edited spectrum.

GABA has three methyl (CH_2) groups resonating as a quintet at 1.9 and as triplets at 2.3 and 3.0 ppm (14-16). The 3.0 ppm resonance overlaps with creatine at 3.0 ppm, which can have up to a 6-fold higher concentration than GABA in the human brain (14). The selective inversion of the 1.9 ppm group on a spin echo experiment, causes the coupled group (J = 7.3 Hz) at 3.0 ppm to be observed as a conventional triplet. However, if the selective inversion is not present, the side peaks of the 3.0 ppm group are inverted. When these measurements are subtracted the outer peaks of the triplet remain without the singlet (not coupled) signals. This

scheme is applied on alternating scans with an echo time of 1/2*J* (68 ms).

Lactic acid is a system of four non-exchangeable protons. Selective inversion of the methine group at 4.1 ppm in a spin echo experiment with an echo time of TE = 1/*J* (*J* = 6.93 Hz) results in the doublet methyl group at 1.3 ppm to be observed upright (14). In the case of no selective inversion, the polarity of the doublet is reversed. Subtraction of these measurements leaves an upright doublet resonating at 1.3 ppm without overlapping lipids or other singlets (uncoupled resonances) (16).

Higher magnetic field strengths can be advantageous for the detection of metabolites signals with low concentration as they offer an increase in SNR and chemical shift dispersion (17-19). The increased chemical dispersion can be advantageous to separate metabolites that overlap at lower fields. However, MRS at higher field strengths suffers from increased chemical shift displacement artifacts (CSDA). Although the selective inversion pulses are insensitive to CSDA, the refocusing pulses for voxel localization are sensitive to CSDA due to limited B_1 amplitude and bandwith. The increased CSDA can substantially reduce the efficiency of the editing techniques (during voxel selection) aimed at metabolites with coupled groups at distant resonance frequencies (e.g. lactate in particular, where the chemical shift difference between the coupled spins is 2.8 ppm large). In single voxel MRS editing four compartments can be defined (20). Each compartment affects the two J-coupled spin groups differently due to their chemical shift difference. In one compartment both spin groups will be refocused equally as all coupled spin groups will feel all refocusing pulses. On two of the compartments only one of the refocusing pulses will be felt by one of the coupled spin groups (usually the A group). As for the last compartment, none of the refocusing pulses will be felt by one of the coupled spin groups. These refocusing differences result in partial refocusing of the J-coupling effects. Consequently, the resulting signal will be a sum of all compartments, which depending on inter-pulse timings can be negative and thus can even cancel the edited signal (21). For this reason, the use of broad-banded refocusing pulses would be advantageous to minimize the CSDA or compartmentalization effects, improving the efficiency of single voxel MRS editing.

Adiabatic RF refocusing pulses are advantageous due to their increased bandwidths, when compared to conventional RF pulses. These RF pulses have been used in the semi-LASER (sLASER) sequences to minimize the CSDA and to overcome the B_0 and B_1 non uniformities (22-26). Conveniently, the CSDA encountered with the adiabatic refocusing pulses can be further reduced as Ordidge et al. (27) have shown using

frequency offset corrected inversion (FOCI) pulses for localized spectroscopy. The FOCI pulses are not only amplitude and frequency modulated, but also gradient modulated. These pulses can be constructed based on a hyperbolic secant (HS) pulse and can increase the original bandwidth by an order of magnitude without compromising the pulse performance. At high field strengths, the FOCI pulses may substantially reduce the CSDA, thus improving the editing efficiency. In addition, the B_0 and B_1^+ field non-uniformities (which scale with field strength) do not affect the performance of the adiabatic FOCI pulses. Consequently, the CSDA is only limited by the gradient strengths rather than the B_1 limitations of the system.

In the work of Andreychenko et al. (12) a semi-adiabatic LASER (sLASER) editing sequence that uses Mescher-Garwood (MEGA) pulses (MEGA-sLASER) to refocus the J-coupled metabolites has been used to measure GABA in the human brain at 7 T. The selective MEGA pulses are centered interleaved at 1.9 ppm or 1.5 ppm, hence contributing equally to the macromolecules (MM) located at 1.7 ppm. Consequently, after subtraction of the interleaved measurements, the 1.7 ppm MM contribution can be cancelled out. While the chemical shift difference between the coupled groups of GABA is relatively small (only 1.1 ppm), still the efficiency for its detection can be further improved if using the previously described FOCI pulses. For lactate the chemical shift difference (groups at 4.1 ppm and 1.3 ppm) is 2.5-fold higher than for the GABA spins, therefore the use of the same technique could result in a 6.25-fold increase in CSDA. The use of FOCI pulses can reduce the CSDA by an order of magnitude, thereby substantially affecting the efficiency of the MRS editing for metabolites like lactate.

Therefore, we propose to include FOCI pulses for refocusing in a MEGA-sLASER sequence for single voxel MRS editing with increased bandwidth (and therefore decreased CSDA) and a limited B_1 of 20mT at 7T. Compared to high bandwidth adiabatic RF pulses, we demonstrate the improved sensitivity and efficiency of the FOCI pulses when used in a MEGA-sLASER sequence, particularly for the edited detection of lactate.

5.2 Methods

FOCI pulses were generated based on a hyperbolic secant (HS) pulse according to the amplitude B(t) and frequency ω(t) modulation functions from equations 5.1 and 5.2 (27). The gradient shape G(t) was

also modulated according to equation 5.3.

$$B(t)=A(t)\times B_{1,max}\times \mathrm{sech}[\beta(1-2t/T)] \quad 5.1$$

$$\omega(t)=A(t)\times(-\mu\beta \tanh[\beta(1-2t/T)]+\omega_0) \quad 5.2$$

$$G(t)=A(t)\times G_{HS} \quad 5.3$$

$$A(t)=\begin{cases}\cosh(\beta t) & \text{if } \mathrm{sech}(\beta t)>1/f_F \\ f_F & \text{otherwise}\end{cases} \quad 5.4$$

where t is the time interval, T is the pulse duration, β and μ are adjustable dimensionless parameters that change the shape of the hyperbolic secant. The off resonance frequency related to the spatial localization corresponds to w_0. The modulation function A(t) in equation 5.4 is chosen depending on the (adjustable and also dimensionless) *foci factor* f_F and the resulting bandwidth of the FOCI pulse can be calculated as . Note that a foci factor of 1 results in a standard HS pulse.

The parameters T, μ, β, $B_{1,max}$ and f_F were chosen to be 6.7 ms, 200, 4.2, 18mT and 10, such that the resulting FOCI pulse is within the B_1 and gradient limits of the 7T MR system. G_{HS} is the required gradient strength to refocus the slice when the HS pulse would have been used. Frequency inversion profiles of the HS and FOCI RF pulses were simulated on- and off-resonance (MATLAB R2010b, The MathWorks, Inc.) to evaluate and compare pulse performances. The refocusing component for the FOCI pulses at different RF intensities ranging from 0.2 to 2 kHz was simulated to investigate its adiabatic behavior and adiabatic condition threshold. The theoretical efficiency of the HS and the FOCI pulses was calculated based on the bandwidths of each pulse. These calculated efficiencies are used for comparison with the real (phantom and in-vivo) MRS measurements.

All experiments were performed on a 7 Tesla MR scanner (Philips, Cleveland, OH, USA) interfaced to a dual channel NOVA volume transmit head coil and a 32 channel receiver array (NOVA Medical, Inc. Wilmington MA) using a 4kW peak power amplifier. A tube of 10 cm length and 1 cm diameter containing a high concentration of lactate was used as a phantom to compare the MEGA-sLASER editing sequence with either HS (f_F=1) or FOCI (f_F=10) pulses for refocusing. The phantom was positioned along the B_0 field of the MR scanner and the slice selective excitation was chosen along the tube. The spectroscopy voxel was positioned such that

the intersection of the chemical shift boxes of the 4.1 ppm and the 1.3 ppm groups for the refocusing pulses overlapped with the phantom to ensure 100% detection of the lactate signal in both cases (diagram on Figure 5.3 a). A second measurement was obtained with the phantom positioned in the middle of the selected volume corresponding to the chemical shift box of the 4.1 ppm group. Single voxel MRS measurements were obtained with the MEGA-sLASER (with HS or FOCI RF pulses), TE/TR = 144/6500 ms, 2 averages and 100x100x30 mm^3 voxel. The relative signal difference between the two measurements was used to measure the efficiency of the two sequences.

In-vivo measurements of GABA and lactate from the brain of healthy volunteers were also obtained (MEGA-sLASER (HS or FOCI with f_F = 10), TE/TR=74/5000 ms, 64 NSA and 144/6600ms, 32 NSA respectively) on a 27mL and 36mL volume, to ensure enough SNR and a short acquisition time to accurately observe the differences when using FOCI or HS RF pulses for refocusing. The long repetition times were chosen to ensure compliance to SAR guidelines even when the transmit coil was driven in quadrature rather than in dual transmit. With the available coil setup at our 7T scanner it is possible to reach at least 18mT in the brain. Therefore, all FOCI pulses and the excitation pulse were set to the maximum B_1 of 18mT. Each MRS acquisition was frequency aligned with the non affected singlet resonance of choline. The acquisitions were averaged after correction and the signal intensities of GABA and lactate were compared between the different RF pulses used in the corresponding sequence. To compare efficiencies of the measurements with the different refocusing pulses GABA over creatine (GABA/Cr) and lactate over creatine (lac/Cr) ratios were calculated in each in-vivo case. The GABA and lactate peaks were fitted in MATLAB (MATLAB R2010b, The MathWorks, Inc.) as doublets on the edited spectra with fixed separations between the peaks (14 Hz for GABA and 7 Hz for lactate). The creatine peaks were fitted as a singlet in MATLAB on the summed spectra for either the GABA or the lactate measurements. Fitted peaks were integrated to calculate the GABA/Cr and lac/Cr ratios.

5.3 Results

The resulting modulation shapes of the FOCI pulse using T=6.7 ms, β=4.2, μ=200 and f=10 are shown in Figure 4.1 a, b and c (black line). For comparison, the modulation shapes of the original hyperbolic secant (HS)

pulse are also shown (gray). The spatial inversion profiles for both RF pulses are compared for the spins on- and 850 Hz off-resonance in d) (i.e. chemical shift difference between lactate spin groups). The off-resonance inversion profile of the FOCI pulse shows only 4.7% shift compared to the 47% found for the - already high bandwidth - HS RF pulse. The inversion profile of the FOCI pulse has also a sharper transition compared to the HS pulse, which improves the localization of the technique. The refocusing component is shown in Figure 5.2 for the FOCI refocusing RF pulse with a foci factor of 10. For RF amplitudes (γB_1) below 600 Hz, the pulse did not yet reach the adiabatic condition as visualized by the lower refocused magnetization. Above the 600 Hz threshold, the FOCI pulses remained adiabatic and were able to refocus more than 95% of the magnetization. The theoretical efficiency of the GABA and lactate detection was calculated using the bandwidth differences (i.e. the resulting CSDA) between the HS and the FOCI inversion pulses. The added signal expected from the four compartments lead to a maximum efficiency of 92% against 98% for GABA and 54% against 95% for lactate when comparing the HS (f_F= 1) and the FOCI (f_F=10) pulse respectively.

Phantom measurements in the intersection of the chemical shift boxes showed equal signal to noise ratio (SNR) when using either the FOCI or the HS pulses for signal refocusing (Figure 5.3 a). However, the HS pulses showed 57% signal loss when the phantom was positioned in the middle of the voxel selection (Figure 5.3 b). The FOCI pulses on the other hand, provided 100% of the edited lactate signal.

In-vivo results show the edited signal of GABA and lactate in the human brain at 7T (Figure 5.4 and Figure 5.5). Both measurements demonstrate the proof of principle and essence of using the broad banded FOCI pulses to overcome efficiency degradation by limits in B_1 field amplitudes. Figure 5.4 c demonstrates, as expected from the calculated theoretical efficiency, the increased GABA signal obtained at the particular location indicated in the MRI (Figure 5.4 a) when using the FOCI refocusing pulses instead of the HS RF pulses (Figure 5.4 b). In this in-vivo measurement, the GABA over creatine (GABA/Cr) ratios resulted in 1.07 and 1.36 for the HS and the FOCI RF pulses respectively meaning that the FOCI pulses were 26% more efficient when compared to the HS pulses (Figure 5.4 d). Figure 5.5 a, shows the voxel positioning used for obtaining lactate on the brain. A substantial signal gain for the lactate signal was found when measuring with FOCI refocusing pulses as compared to HS refocusing pulses (Figure 5.5 c and b respectively) even after correction with the water reference

peak (Figure 5.5 d). The lactate/Cr ratios for the HS and FOCI pulses were 0.19 and 0.34 respectively, resulting in a 75% improved efficiency for the FOCI pulses (Figure 5.5 e). In addition, an improved overall SNR is seen in the edited spectrum due to the improved selection profile (yields a bigger voxel) when using the FOCI pulses. Furthermore, a 37% RF power deposition increase was found when using the sequence with the FOCI pulses as compared with the use of HS pulses. However, the relatively low B_1 that these pulses need (18mT), guarantees that SAR is kept within safety guidelines (28) at the used TR.

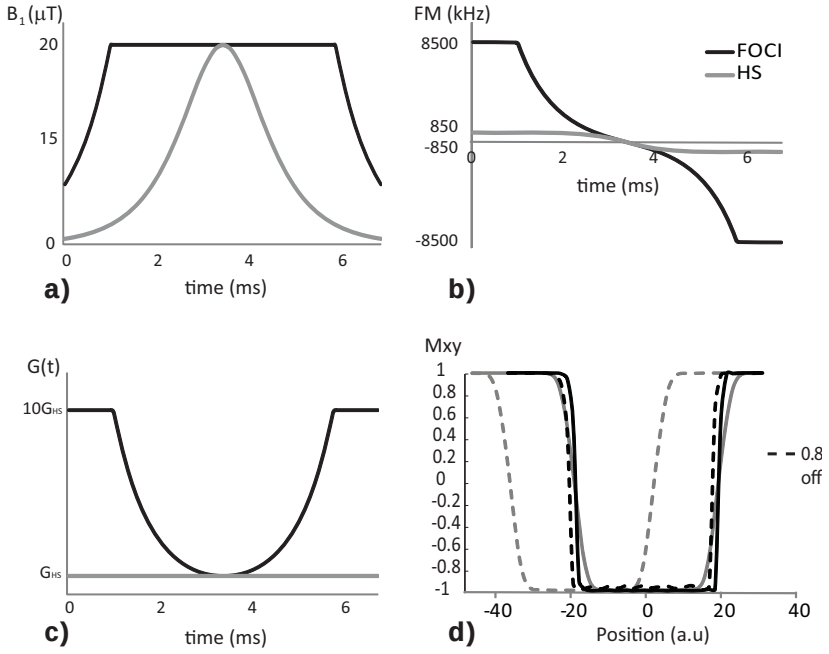

Figure 5.1: a) amplitude, b) frequency and c) gradient modulation functions for the original hyperbolic secant and FOCI (f=10) RF pulses. The inversion profiles for both pulse shapes are shown in d) on-resonance (hard lines) and 850 Hz off-resonance (dashed lines) corresponding to the chemical shift between the lactate spin groups. The FOCI pulse shows only 4.7% shift of its inversion profile compared with the 47% for the HS pulse.

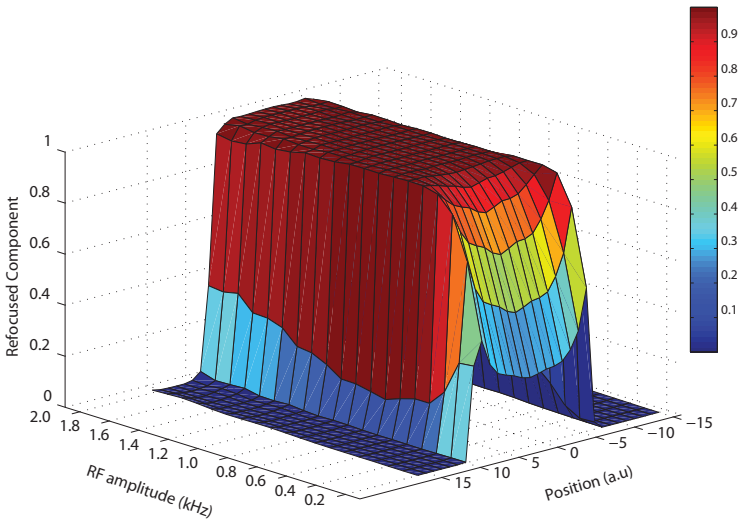

Figure 5.2: refocused component obtained for the FOCI RF pulses for a range of RF amplitudes. For low RF amplitudes such as 0.2 kHz, the adiabatic condition is yet not reached. For amplitudes above 0.6 kHz, the adiabatic condition is fulfilled and the FOCI pulses can refocus the full magnetization within its selection bandwidth.

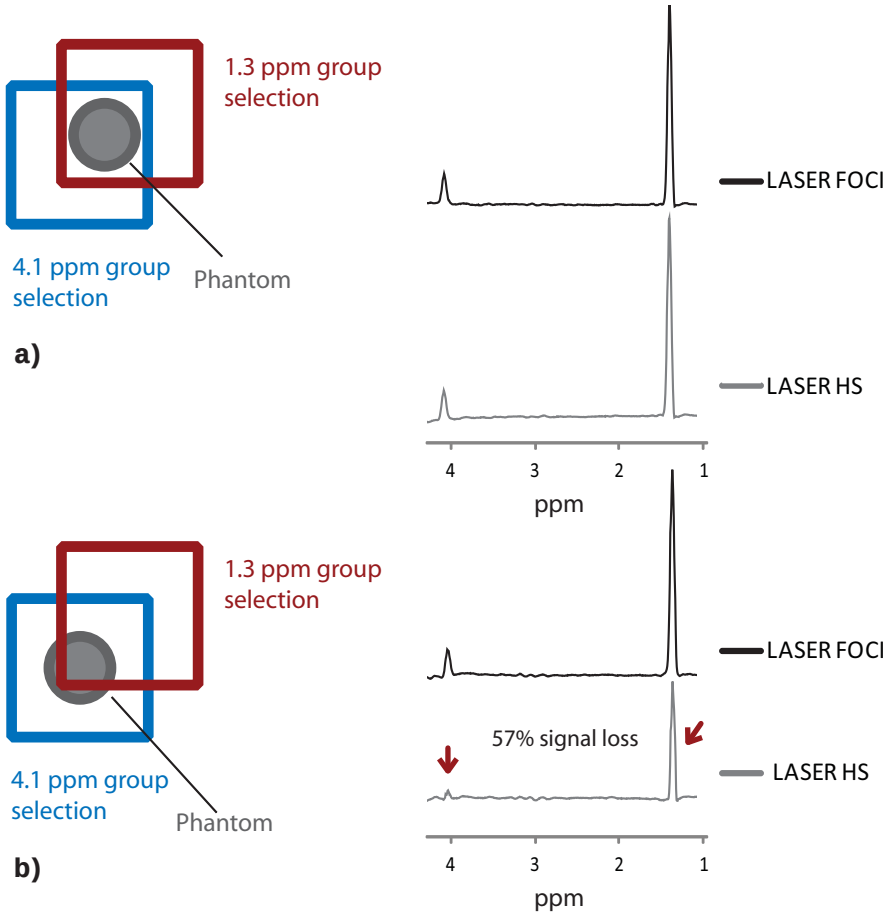

Figure 5.3: Lactate editing with LASER sequence on a phantom. On a), the phantom was positioned in the intersection of the chemical shift boxes between water and lactate. Full signals from the 4.1 and 1.3 ppm groups are observed with the HS and FOCI pulses. Another case is observed in b), where the phantom was positioned in the middle of the selection box for water. Measurements using FOCI pulses for refocusing (black), showed full signals for the 1.3 and 4.1 ppm groups. However, the measurement with HS refocusing pulses showed 57% signal lost for the 1.3 ppm group.

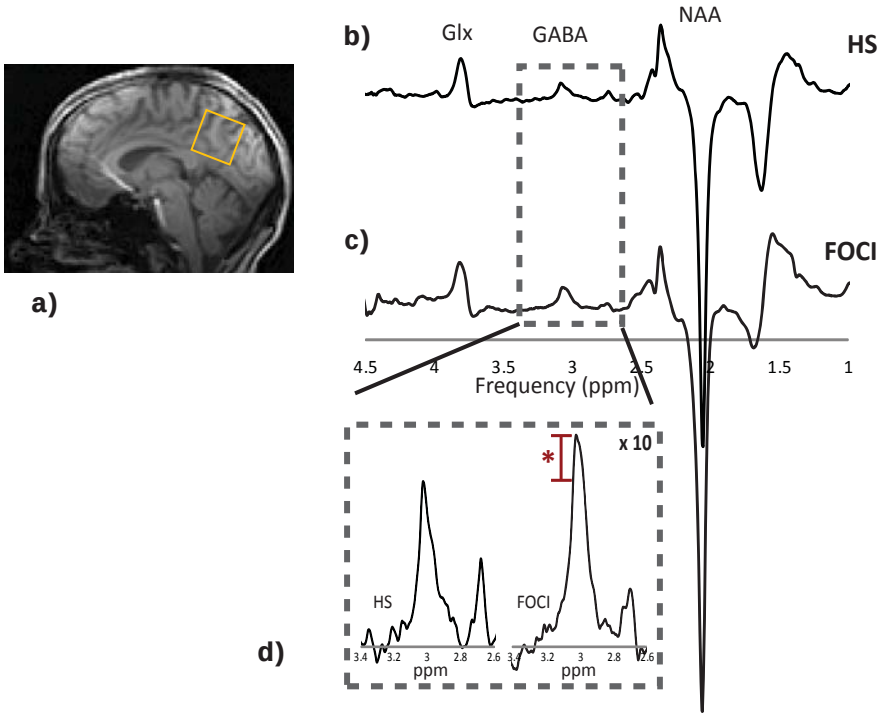

Figure 5.4: GABA editing with different RF pulses for refocusing. On a) the localization of the voxel on the brain of a volunteer is shown. MRS (sLASER, TE/TR = 74/5000 ms, 64 averages, 30x30x30 mm^3 voxel) obtained with b) HS pulses for refocusing and c) FOCI refocusing pulses. Higher SNR is obtained with the FOCI pulses as shown in the zoomed area for the GABA peaks in d). The increased signal obtained with the FOCI pulses (*) corresponds to 26% more than for the HS pulses, when comparing the GABA/Cr ratios (non-edited metabolite spectra not shown).

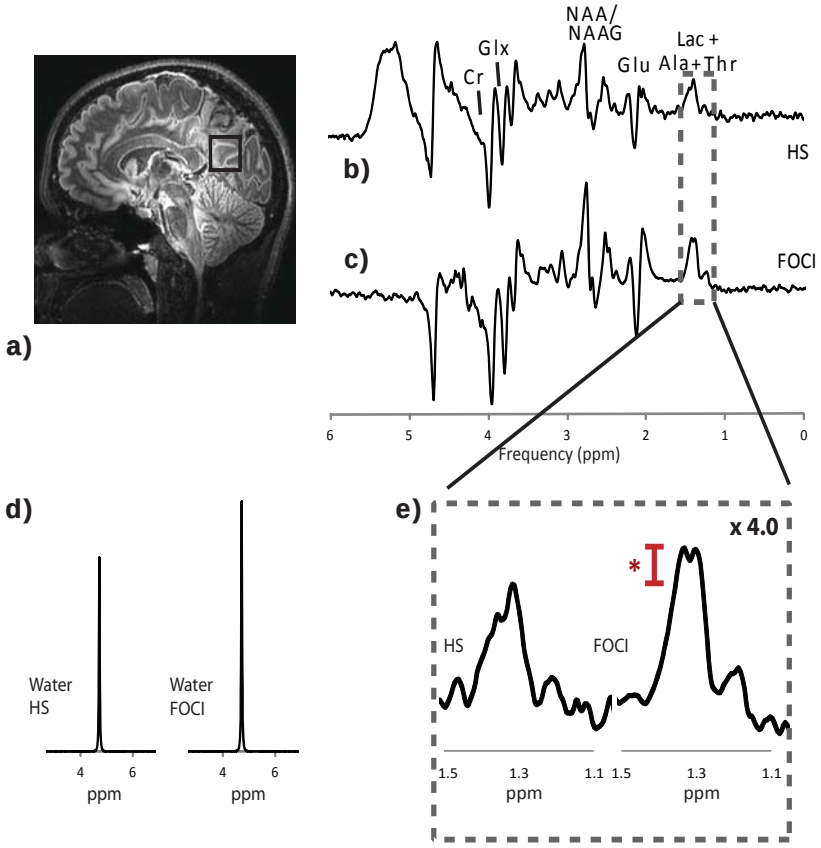

Figure 5.5: a) 3D fluid attenuated inversion recovery (FLAIR) image of the brain showing the MRS voxel localization. Single voxel lactate editing MRS (sLASER, TE/TR = 144/6600 ms, 32 averages, 30x30x40 mm^3 voxel) using b) HS refocusing pulses and c) FOCI refocusing pulses. The spectrum obtained with the FOCI refocusing pulses shows higher SNR, best water suppression and splitting of the lactate peak at 1.3 ppm, even after correction with the water reference peak (d) that removes the gain (31% higher with the FOCI pulses) from the improved transition in the spatial selection. The zoomed spectra (e) show the increased lactate signal obtained by the FOCI pulses measurement. (*) The lac/Cr ratio calculated for the FOCI pulses resulted in 75% increased efficiency when compared to the HS pulses. (Non-edited metabolite spectra not shown).

5.4 Discussion

Detection of metabolites such as GABA and lactate can be challenging. This is not only due to their low concentrations (and therefore low SNR), but also due to the fact that their MR signals overlap with other signals with higher concentrations.

Higher magnetic field MR systems can offer increased SNR and increased chemical shift dispersion (17-19). The latter property can be beneficial for selective inversion pulses in editing techniques used to remove overlapping signals (12). Despite the increase of CSDA (coincident with the increased chemical shift dispersion) at higher field strengths, we showed improved MRS editing efficiency at 7T and therefore increase sensitivity to detect coupled metabolites like GABA and lactate.

Fitting techniques have been used to extract signals from short TE MRS experiments (29). However, metabolites like GABA and lactate that overlap with other metabolites at the same frequencies are difficult to quantify correctly using only an LC model analysis. The basis sets and the correct contribution from the MM should be known at the given field strength, which may be subject dependent. Extremely challenging would be to use an LC model analysis in patient data, given that little information is known about the behavior of the different metabolites and macromolecules in these populations. While indeed this short echo time (TE) approach is more sensitive than editing at a longer TE, the specificity of the short TE approach without editing remains questionable.

At ultra high field strengths (e.g. 7 Tesla) the relatively low B_1 amplitude available, limits the maximum bandwidth of the refocusing RF pulses. More importantly, when using editing techniques, the increase of CSDA will result in signal cancelation within the actual voxel, depending on the bandwidth of the refocusing pulses. FOCI pulses have been described elsewhere (27,30) and they have been used to reduce the chemical shift displacement artifact (CSDA). The MRS editing CSDA at 7T has been reduced with the implementation of FOCI RF refocusing pulses in a MEGA-sLASER sequence (12). While adiabatic RF refocusing pulses have been included before to reduce the CSDA (31), the bandwidth of the FOCI pulses is broader, resulting in an up to 10-fold more CSDA reduction along with 95% efficient detection of lactate (2.8 ppm chemical shift difference between coupled groups) at 7T. In addition, due to the improved spatial transition profile of the FOCI compared to the HS refocusing pulses, the SNR in the in-vivo experiments is improved. Efficient editing of GABA

has already been shown at 7T (12), where B_1 focusing with two transmit channels was necessary to obtain sufficiently strong B_1 (32). Although the RF power deposition can be reduced per unit of B_1^+ when using RF focusing, the FOCI pulses do not require full B_1 focusing to ensure a low CSDA. As we have shown in this study, the B_1 provided by a conventional transmit coil in the human head at 7T (18mT), can be sufficient for a good performance of the FOCI pulses.

The FOCI pulses are adiabatic, thus their slice profile is insensitive to B_1^+ field non-uniformities. While multi transmit coils can be considered to provide a uniform B_1, they may not be used to reduce the CSDA. The high bandwidth required to assure minimum CSDA in the editing results, implies the use of adiabatic RF pulses, not only for their insensitivity to B_1 but mostly for their high bandwidth per unit of peak B_1. While uniformity with a multi transmit system can be provided, it comes at the expense of increased RF power deposition, so would lengthen the TR of the FOCI editing sequence even more. Considering the relatively small voxel size, when compared to the transmit field RF wavelength, adiabatic RF pulses may not be considered essential as the non-uniformities within the selected voxel are expected to be small. However, the main purpose of voxel selection is to avoid signal contamination in the spectrum from signals outside the volume of interest. Consequently, the use of conventional pulses would result in variable performances related to the local B_1 levels. Particularly for the refocusing pulses, this effect would result in significant signal loss (33-35). The adiabatic performance of the FOCI pulses remained stable even for spins at 850 Hz off-resonance. Other gradient modulated pulses have been explored for MRS sequences, such as GOIA pulses (36,37). However, the off-resonance performance of the GOIA pulses resulted in poor pass bands compared to the FOCI pulses, thus lowering the efficiency and outcome prediction. Optimization of FOCI pulses has also been investigated leading to time-resample (TR-) FOCI (38), which can be more efficient and less B_1 sensitive at lower B_1 amplitudes, at the cost of requiring more parameterization. Nevertheless, the performance of the FOCI pulses remains better at the relatively high B_1 amplitudes of 18mT.

Phantom and in-vivo measurements showed increased efficiency of the MEGA-sLASER MRS editing method when using FOCI refocusing pulses. Even for metabolites with relatively small chemical shift difference between the coupled spins, like GABA the improvement was up to 20%. In addition to the enhanced efficiency, the localization of the MEGA-sLASER sequence with FOCI pulses is also improved. Although the

improved efficiency of including the FOCI pulses could have been only demonstrated in phantoms, in-vivo measurements were also obtained not only for GABA, but also for lactate detection demonstrating the applicability of the method. Furthermore, due to the reduced CSDA of the FOCI pulses, the transition between pass-band and stop-band is sharper when compared to that of the HS pulses. While this benefits the efficiency, it also reduces partial volume effects. Due to the fact that the editing is based on subtraction of relatively large overlapping signals that require frequency and phase alignments per shot, the acquisition of spatial mapping with a CSI approach is challenging. In addition, as uniformity must be assured over a larger area when considering CSI, B_1 and B_0 shimming will be compromised. Finally, when even considering CSI, CSDA can be treated differently, which may be less severe when techniques like OVERPRESS are used (39,40).

The FOCI pulses overcome bandwidth limitations and consequently CSDA. Nevertheless, other sequence limitations exist. Such limitations include the *foci* factor, which is restricted by the maximum available B_0 gradient strength, which in turn limits the minimum voxel size (or the maximum bandwidth). A *foci* factor of 10 with our current setup and a maximum gradient strength of 40mT/m set the minimum possible voxel size to 1.1cm. Another important limitation is the RF power deposition. At the same maximum B_1 level, the RF duty cycle of the FOCI pulses was higher when compared to the HS. In consequence, the sequence with the FOCI pulses showed 3-fold more RF power deposition. Despite this, the FOCI pulses can be operated at lower B_1 levels, thus reducing the overall RF power deposition (e.g. a reduction of 16% local SAR is obtained when lowering the B_1 amplitude from 18 to 15mT). The local SAR averaged over 10g of tissue (28) is kept at all times below the maximum of 8W/kg by using relatively long repetition times, due to the increased RF duty cycle imposed by the FOCI pulses. However, the minimum TR based on this maximum local SAR of 8W/Kg averaged over 10g of tissue, can be lowered when using lower B_1 amplitudes (e.g. using a f_F=10 the TR can be lowered from 4780 ms at B_{1max}=18mT to 4020 ms at B_{1max} 15mT). Further lowering of the peak and overall RF power deposited can be done with altered FOCI pulses like VERSE-FOCI (41). The VERSE-FOCI pulses can use less than 50% of the peak power and a total RF power of 94% compared to the original HS pulse. However, these pulses are still sensitive to B_0 variations. Moreover, B_1 focusing with a dual transmit setup can be used to further reduce the SAR (32), while keeping the *foci* factor of 10 and the B_1 of 18mT. Consequently, the MEGA-sLASER sequence can be performed

with the proposed FOCI pulses (f_F=10, B_1=18mT) using a dual transmit head coil at 7T with a TR of 4.5s. Alternatively, the *foci factor* can also be reduced with the normal quadrature setup to decrease the TR.

5.5 Conclusion

The MEGA-sLASER sequence including FOCI pulses for refocusing is an efficient and accurate method for MRS editing of weakly coupled systems at high field strengths such as 7 T.

REFERENCES

1. Behar KL, den Hollander JA, Stromski ME, Ogino T, Shulman RG, Petroff OA, Prichard JW. High-resolution 1H nuclear magnetic resonance study of cerebral hypoxia in vivo. Proc Natl Acad Sci U S A 1983;80(16):4945-4948.

2. Behar KL, Rothman DL, Shulman RG, Petroff OA, Prichard JW. Detection of cerebral lactate in vivo during hypoxemia by 1H NMR at relatively low field strengths (1.9 T). Proc Natl Acad Sci U S A 1984;81(8):2517-2519.

3. Bruhn H, Frahm J, Gyngell ML, Merboldt KD, Hanicke W, Sauter R, Hamburger C. Noninvasive differentiation of tumors with use of localized H-1 MR spectroscopy in vivo: initial experience in patients with cerebral tumors. Radiology 1989;172(2):541-548.

4. Yaligar J, Thakur SB, Bokacheva L, Carlin S, Thaler HT, Rizwan A, Lupu ME, Wang Y, Matei CC, Zakian KL, Koutcher JA. Lactate MRSI and DCE MRI as surrogate markers of prostate tumor aggressiveness. NMR in Biomedicine 2012;25(1):113–122.

5. Brambilla P, Perez J, Barale F, Schettini G, Soares JC. GABAergic dysfunction in mood disorders. Mol Psychiatry 2003;8(8):721-737, 715.

6. Petroff OA, Hyder F, Rothman DL, Mattson RH. Homocarnosine and seizure control in juvenile myoclonic epilepsy and complex partial seizures. Neurology 2001;56(6):709-715.

7. Keltner JR, Wald LL, Frederick BDB, Renshaw PF. In vivo detection of GABA in human brain using a localized double-quantum filter technique. Magnetic Resonance in Medicine 2005;37(3):366-371.

8. Lange T, Trabesinger AH, Schulte RF, Dydak U, Boesiger P. Prostate spectroscopy at 3 Tesla using two-dimensional S-PRESS. Magnetic Resonance in Medicine 2006;56(6):1220-1228.

9. Lange T, Schulte RF, Boesiger P. Quantitative J-resolved prostate spectroscopy using two-dimensional prior-knowledge fitting. Magnetic Resonance in Medicine 2008;59(5):966-972.

10. De Graaf RA, Dijkhuizen RM, Biessels GJ, Braun KPJ, Nicolay K. In vivo glucose detection by homonuclear spectral editing. Magnetic Resonance in Medicine 2000;43(5):621-626.

11. Lee HK, Yaman A, Nalcioglu O. Homonuclear J-refocused spectral editing technique for quantification of glutamine and glutamate by 1H NMR spectroscopy. Magnetic Resonance in Medicine 2005;34(2):253-259.

12. Andreychenko A, Boer VO, Arteaga de Castro CS, Luijten PR, Klomp DW. Efficient spectral editing at 7 T: GABA detection with MEGA-sLASER. Magn Reson Med 2011.

13. Lazeyras F, Terrier F, Aue WP, Frey FJ, Howarth N. Measurement of lactate in acutely ischemic rat kidneys using magnetic resonance spectroscopy. Investigative Radiology 1994;29(1):24-30.

14. De Graaf RA. In vivo NMR Spectroscopy: Principles and Techniques. WILEY, editor; 2007.

15. Kaiser LG, Young K, Meyerhoff DJ, Mueller SG, Matson GB. A detailed analysis of localized J-difference GABA editing: theoretical and experimental study at 4 T. NMR Biomed 2008;21(1):22-32.

16. Star-Lack J, Spielman D, Adalsteinsson E, Kurhanewicz J, Terris DJ, Vigneron DB. In Vivo Lactate Editing with Simultaneous Detection of Choline, Creatine, NAA, and Lipid Singlets at 1.5 T Using PRESS Excitation with Applications to the Study of Brain and Head and Neck Tumors. Journal of Magnetic Resonance 1998;133(2):243-254.

17. Klomp DWJ, Bitz AK, Heerschap A, Scheenen TWJ. Proton spectroscopic imaging of the human prostate at 7 T. NMR in Biomedicine 2009;22(5):495-501.

18. Tkác I, Andersen P, Adriany G, Merkle H, Ugurbil K, Gruetter R. In vivo 1H NMR spectroscopy of the human brain at 7 T. Magnetic Resonance in Medicine 2001;46(3):451-456.

19. Vaughan JT, Garwood M, Collins CM, Liu W, DelaBarre L, Adriany G, Andersen P, Merkle H, Goebel R, Smith MB, Ugurbil K. 7T vs. 4T: RF power, homogeneity, and signal-to-noise comparison in head images. Magnetic Resonance in Medicine 2001;46(1):24-30.

20. Yablonskiy DA, Neil JJ, Raichle ME, Ackerman JJH. Homonuclear J coupling effects in volume localized NMR spectroscopy: Pitfalls and solutions. Magnetic Resonance in Medicine 1998;39(2):169-178.

21. Schick F, Nägele T, Klose U, Lutz O. Lactate quantification by means of press spectroscopy—Influence of refocusing pulses and timing scheme. Magnetic Resonance Imaging 1995;13(2):309-319.

22. De Graaf RA, Luo Y, Terpstra M, Merkle H, Garwood M. A New Localization Method Using an Adiabatic Pulse, BIR-4. Journal of Magnetic Resonance, Series B 1995;106(3):245-252.

23. Slotboom J, Bovée WMMJ. Adiabatic slice-selective rf pulses and a single-shot adiabatic localization pulse sequence. Concepts in Magnetic Resonance 1995;7(3):193-217.

24. De Graaf RA, Nicolay K. Adiabatic rf pulses: Applications to In vivo NMR. Concepts in Magnetic Resonance 1997;9(4):247-268.

25. Garwood M, DelaBarre L. The Return of the Frequency Sweep: Designing Adiabatic Pulses for Contemporary NMR. Journal of Magnetic Resonance 2001;153(2):155-177.

26. Sacolick LI, Rothman DL, Graaf RAd. Adiabatic refocusing pulses for volume selection in magnetic resonance spectroscopic imaging. Magnetic Resonance in Medicine 2007;57(3):548-553.

27. Ordidge RJ, Wylezinska M, Hugg JW, Butterworth E, Franconi F. Frequency offset corrected inversion (FOCI) pulses for use in localized spectroscopy. Magnetic Resonance in Medicine 1996;36(4):562-566.

28. The International Commission on Non-Ionizing Radiation P. Medical Magnetic Resonance (MR) Procedures: Protection of patients. Health Physics 2004;87(2):197-216.

29. Tkáč I, Öz G, Adriany G, Uğurbil K, Gruetter R. In vivo 1H NMR spectroscopy of the human brain at high magnetic fields: Metabolite quantification at 4T vs. 7T. Magnetic Resonance in Medicine 2009;62(4):868-879.

30. Kinchesh P, Ordidge RJ. Spin-echo MRS in humans at high field: LASER localisation using FOCI pulses. Journal of Magnetic Resonance 2005;175(1):30-43.

31. Scheenen TW, Klomp DW, Wijnen JP, Heerschap A. Short echo time 1H-MRSI of the human brain at 3T with minimal chemical shift displacement errors using adiabatic refocusing pulses. Magn Reson Med 2008;59(1):1-6.

32. Boer VO, van Lier ALHMW, Hoogduin JM, Wijnen JP, Luijten PR, Klomp DWJ. 7-T 1H MRS with adiabatic refocusing at short TE using radiofrequency focusing with a dual-channel volume transmit coil. NMR in Biomedicine 2011;24(9):1038-1046.

33. Duijn JH, Matson GB, Maudsley AA, Hugg JW, Weiner MW. Human brain infarction: proton MR spectroscopy. Radiology 1992;183(3):711-718.

34. Ryner LN, Ke Y, Thomas MA. Flip Angle Effects in STEAM and PRESS—Optimized versus Sinc RF Pulses. Journal of Magnetic Resonance 1998;131(1):118-125.

35. Wild JM, Marshall I. Normalisation of metabolite images in 1H NMR spectroscopic imaging. Magnetic Resonance Imaging 1997;15(9):1057-1066.

36. Near J, Romagnoli C, Curtis AT, Klassen LM, Izawa J, Chin J, Bartha R. High-field MRSI of the prostate using a transmit/receive endorectal coil and gradient modulated adiabatic localization. Journal of Magnetic Resonance Imaging 2009;30(2):335-343.

37. Tannús A, Garwood M. Adiabatic pulses. NMR in Biomedicine 1997;10(8):423-434.

38. Hurley AC, Al-Radaideh A, Bai L, Aickelin U, Coxon R, Glover P, Gowland PA. Tailored RF pulse for magnetization inversion at ultrahigh field. Magnetic Resonance in Medicine 2010;63(1):51-58.

39. Li Y, Osorio JA, Ozturk-Isik E, Chen AP, Xu D, Crane JC, Cha S, Chang S, Berger MS, Vigneron DB, Nelson SJ. Considerations in applying 3D PRESS H-1 brain MRSI with an eight-channel phased-array coil at 3 T. Magnetic Resonance Imaging 2006;24(10):1295-1302.

40. Tran T-KC, Vigneron DB, Sailasuta N, Tropp J, Le Roux P, Kurhanewicz J, Nelson S, Hurd R. Very selective suppression pulses for clinical MRSI studies of brain and prostate cancer. Magnetic Resonance in Medicine

2000;43(1):23-33.

41. Shen J, Chen Z, Yang J. New FOCI pulses with reduced radiofrequency power requirements. Journal of Magnetic Resonance Imaging 2004;20(3):531-537.

CHAPTER 6

Corrections of Dynamic B_0 Field Variation Effects on MRSI of the Human Prostate at 7T using Field Probes

Submitted to NMR in Biomed

Abstract

Objectives: to monitor, analyze and correct for the dynamic field variations that cause spectral degradation in MR spectroscopic imaging of the human prostate. These distortions are caused by moving organs that generate substantial temporal and spatial field fluctuations due to susceptibility mismatching with the surrounding tissue and can be both predictable (i.e. caused by periodic breathing and cardiac motion) and unpredictable (i.e. cause by random moving organs such as bowel motion). Here we investigated the effect of these field fluctuations in the prostate of patients with prostate cancer and demonstrated that an internal field probe can be used to correct for its dominant disturbance in MRSI.

Materials and Methods: nine prostate cancer patients were scanned with an endorectal coil (ERC) on a 7 Tesla MR scanner. Dynamic B_0 field variations were observed in these patients using fast dynamic B_0 mapping. Simulations of dynamic B_0 corrections were done with zero up to second order terms. In addition, a field probe tuned and matched for the ^{19}F frequency was incorporated into the housing of the ERC. The data acquired with the field probe was compared to the B_0 maps data and used to correct the MRSI data sets retrospectively.

Results: the dynamic B_0 mapping data showed dynamic variations of up to 30 Hz (0.1 ppm) over 1min 12s at 7T. The simulated zero order corrections, calculated as the root mean square (rms), reduced the standard deviation (STD) of the dynamic variations by an average of 41%. When using second order corrections, the reduction of the STD was on average 56%. The field probe data had the same variation range as the dynamic B_0 data and the variation patterns corresponded. After retrospective correction, the MRSI data showed artifact reduction and improved spectral resolution, which resulted in up to 40% reduced line width of the citrate peaks.

Conclusions: dynamic fluctuations of up to 0.1 ppm inside a static magnetic field are observed in the fixated human prostate. The incorporation of a field probe into an ERC housing for prostate cancer MR examinations can monitor these fluctuations during MRI and MRS. In fact, dynamic B_0 variations can be monitored and corrected for, without having knowledge of where the effects originated.

6.1 Introduction

Proton magnetic resonance spectroscopy (^{1}H MRS) has a high potential for increasing specificity of diagnostics of prostate cancer, particularly when combined with dynamic contrast-enhanced magnetic resonance imaging (DCE-MRI), diffusion-weighted MRI (DWI) and T2-weighted imaging (1-3). MRSI can be further improved when acquired at high field strengths like 7 Tesla. In addition to the increased SNR, high field strengths offer increased spectral resolution that may enable distinct detection of metabolite signals that would overlap at lower fields. The signals of polyamines (3.1 ppm) for instance can be successfully detected and separated from the metabolites signals of choline and creatine (at 3.2 and 3.0 ppm respectively) at 7T, but overlap substantially at 3T and even more at 1.5T (4,5).

The spectral resolution in voxels inside the prostate depends on the homogeneity of the main magnetic field B_0, which can be affected by susceptibility differences of tissues in and outside the prostate. Particularly outside the prostate, these susceptibility differences can be substantial (i.e. transitions from tissue to air or even lipids), which can lead to magnetic field (B_0) non-uniformities inside the prostate, hence requiring external B_0 shimming to ensure a uniform field inside the prostate. However, as it has been demonstrated in brain (6) and breast (7), the field non-uniformity can change dynamically, therefore affecting the MRSI outcome even when the static B_0 was homogeneous after B_0 shimming. While many potential causes can be assigned to the origin of dynamic field distortions, some may be unknown or at least unknown a priori. Some of the field distortions in the breast have a strong correlation to the breathing and cardiac cycle. Also movements of extremities can cause substantial field fluctuations, even in the brain (8). While the prostate is located relatively close to those potential sources of field distortions, it is also located closer to sources of strong susceptibility differences (for instance gas inside the bowels) that may change spatially over time. Thus, dynamic field distortions can be expected in the prostate causing reduction of spectral resolution if not accounted for.

Once the origin of the field distortion is known, dynamic field compensations can be applied as has been demonstrated successfully for the human brain, where shim sets had been calibrated based on the level indicated by the respiratory sensor (6). Even real-time field monitoring, by means of an NMR field camera, has been shown to enable real-time field compensation, as demonstrated for the human breast (7). In fact,

knowing the exact field fluctuations over time and space with real-time measurements can already improve spatial and spectral resolution (9).

As the sources of time-varying field fluctuations are difficult to predict, we propose to measure the magnitude of the field distortions over time using dynamic B_0 mapping at 7 Tesla. The prostate is fixated with an endorectal coil (ERC) balloon to avoid field variations that may arise from its movements. The results of simulated dynamic shim corrections on the fast dynamic B_0 mapping were investigated to compare the reduction of field variations with zero up to second order corrections. In addition, using the concept of Barmet et al. (10), a field probe was incorporated within the endorectal coil housing to enable real-time monitoring of the effects of time dependent susceptibility variations. The field probe data were compared to the results obtained from the dynamic B_0 maps and retrospectively used to correct the MRSI data sets.

6.2 Materials and Methods

This study was approved by the local ethics review board. Nine patients diagnosed with prostate cancer were examined at a 7 Tesla MR scanner (Philips, Cleveland, OH, USA) after written informed consent was obtained. A 2-elements endorectal coil (11) tuned and matched at 298 MHz (Figure 6.1) was used and filled with fluorinated fluid (GALDEN; Solvay Solexis, Milan, Italy), to match the susceptibility of the balloon to the prostate. A 4 kilowatts (kW) MR amplifier was used to transmit with both channels of the ERC in quadrature (2x2kW). After obtaining scout images and T2-weighted images, a static 3D B_0 map was obtained for image based static 2^{nd} order B_0 shimming (3D FFE, TE/TR=3.0/5.2 ms, acquisition matrix 64x84, 2.81x2.81x3 mm^3 voxel, 20 slices). In addition, dynamic B_0 maps were acquired (2D FFE transverse, TR/TE = 10/1.97 ms, 150/300 dynamics, 64x48 acquisition matrix, 2.25x3x10 mm^3 voxel, 0.5s temporal resolution). The dynamic B_0 maps were analyzed in MATLAB (R2010b, The MathWorks, Inc.) to simulate a potential correction with dynamic B_0 shimming using only the spherical harmonics terms f_0, x, y, $2xy$, x^2-y^2 (note that the remaining first and second order shims have been excluded as only one transverse slice information was acquired). The root mean square values (rms) of the not-corrected and the simulated corrected data over the whole prostate were calculated per dynamic.

The field probe (FP) consisted of a small loop coil (1 cm diameter)

tuned and matched to 50 ohm at 280 MHz (^{19}F frequency) and it was positioned within the housing of the ERC on top of the inner balloon (Figure 6.1). This probe used the fluorinated fluid contained in the inner balloon as the sample to monitor the field. The probe was interfaced to a second 4 kW RF amplifier for transmission using a home-built transmit and receive switch and used only a fraction of the available peak power (about 20 W). The receiver line was connected to one of the 32 receiver channels, which after adjustment of the digital filter could obtain the ^{19}F signals as well as the ^{1}H signals. Within the pulse programming environment of the MR system, a sequence building block was constructed that controlled the FP. Fast pulse acquire segments (block pulse excitation, 0.1 ms duration, 2ms acquisition window) at a fixed RF power setting were synchronized to the MR sequences and sent through the FP to monitor the zero order term of the B_0 field. The FP sequence could be positioned almost anywhere in the MR sequence within every repetition time (TR). The timing of the FP recording was set to end 0.8 ms prior to each ^{1}H excitation in the B_0 map and the MRSI sequence. A linear fit over 2 ms of the phase variations in time was used to obtain the frequency and thereby the field variation over time.

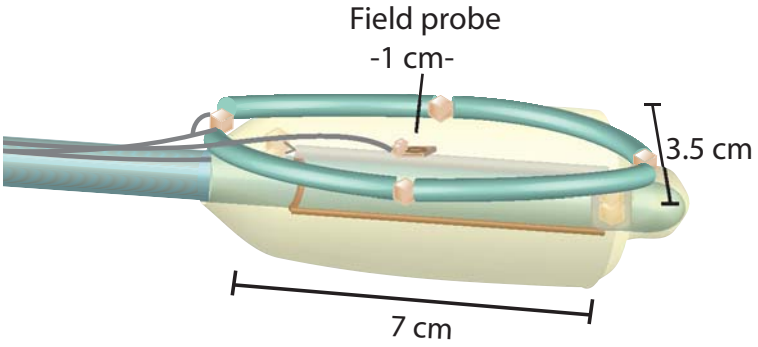

Figure 6.1: Double element endorectal coil (resonant at 298MHz) showing the field probe tuned and matched at 280MHz (^{19}F frequency) used to monitor the field variations on top of the inner balloon of the ERC.

To assess the relation between field variations measured with the FP and the field variations inside the prostate, FP data was recorded during the dynamic B_0 mapping. Without any patient specific calibration, assuming an absolute field relation between the FP and the prostate, the monitored field changes detected with the FP during the MRSI examinations (2D

nsLASER, TE/TR=56/2000 ms, 30x10 matrix, 5x5x5 mm^3 voxel) were used to correct the MRSI data retrospectively (i.e. frequency and phase correction of each point in k-space). Presence of artifacts and spectral resolution were analyzed and compared between the non-corrected and corrected MRSI data sets.

6.3 Results

Figure 6.2 shows the results of the measured dynamic B_0 maps in nine patients. Three of the data sets were acquired without static B_0 shimming (Figure 6.2 a, b, f) and the rest was acquired with static B_0 shimming. The green lines show the original (not-corrected) field variations over time with changes up to 0.1 ppm, equivalent to 30 Hz at 7 Tesla. The inclusion of B_0 shimming did not influence the range of variation or the performance of the simulated dynamic B_0 shimming as seen from the different scales in the data sets that are independent on the a priori performed B_0 shimming. Several patients show periodicity on the dynamic changes at different temporal frequencies (Figure 6.2 a, b, g, h), which may be caused by breathing. However, in the other cases (Figure 6.2c, d, e, f, i), no periodicity is seen. Zero order dynamic corrections, which in principle could be provided by a single FP, are shown with the red lines for all cases. Second order dynamic corrections are shown for three patients (Figure 6.2**.** a, b, c) in blue. The zero order corrections reduced the temporal variations by 38% on average (ranging from 1% to 65%) from the static B_0 shim values. The second order compensations (including zero and first order terms) reduced the temporal variations by 56% on average (ranging from 2% to 86%) from the static B_0 shim values. Overall, the rms of the static shimmed B_0 field variation was on average 0.02 ppm (0.009-0.03 ppm) over the prostate, but increased to 0.04 ppm (0.02-0.07 ppm) when averaged over time per patient. Application of zero or second order B_0 corrections would improve this to 0.02 ppm (0.008-0.03 ppm and 0.007-0.03 ppm respectively).

In Figure 6.3, the field measurements obtained with the dynamic B_0 mapping (Figure 6.3 a) are compared to the monitored field changes obtained with the field probe (Figure 6.3 b). Both measurements have a similar pattern and variation ranges. This demonstrates that the measurements obtained with the field probe resemble the field changes observed in the prostate during this time window. Figure 6.4 b) shows the monitored field changes during the acquisition of an MRSI data

set. Frequency variations up to 12 Hz within a spread of 10 Hz were recorded during the MRSI acquisition. Retrospective corrections of the MRSI were obtained and compared with the non-corrected MRSI data set. A spectrum from a voxel close to the ERC is shown without and with corrections (Figure 6.4 c, d respectively). An improved spectral quality and resolution of the metabolite peaks can be observed in the corrected spectrum as indicated with the arrows for taurine (tau), choline (Cho), polyamines (poly) and creatine (Cr). The line width was measured for the citrate peaks (peaks pointing down centered at 2.6 ppm) at full-width-half-maximum (FWHM) in both non-corrected and corrected spectra, resulting in 40% improvement for the corrected case. In addition, the artifact seen at about 3.9 ppm is removed after correction. For comparison, a second voxel, further away from the ERC is also shown without and with field probe corrections (Figure 6.4 e, f respectively). In this case, an artifact is also present around 3.9 ppm and is removed after corrections. The overall spectral resolution and quality is also improved as indicated by the arrows pointing at the metabolites myo-inositol (mI), taurine, choline, polyamines and creatine that are fully resolved. In this case, the line width calculated for the citrate peaks in the corrected spectrum is improved, by 24%.

6.4 Discussion

The monitoring of the field variations in the human prostate when fixated with an endorectal balloon, resulted in variations of up to 0.1 ppm, which corresponds to the spectral resolution required to differentiate polyamines (3.1 ppm) from choline (3.2 ppm) and creatine (3.0 ppm). The use of the (Cho+Cr)/Cit ratio for cancer detection is well known and thresholds have been determined at several field strengths to distinguish between benign and cancer tissue (12,13). However, in-vivo MRS studies have already shown that the threshold of the (Cho+Cr)/Cit changes if the polyamines contribution is included (5,14), which have shown to increase in benign tissue (15-17). Therefore, accurate detection of the overlapping polyamines maybe crucial for a precise diagnose of prostate cancer.

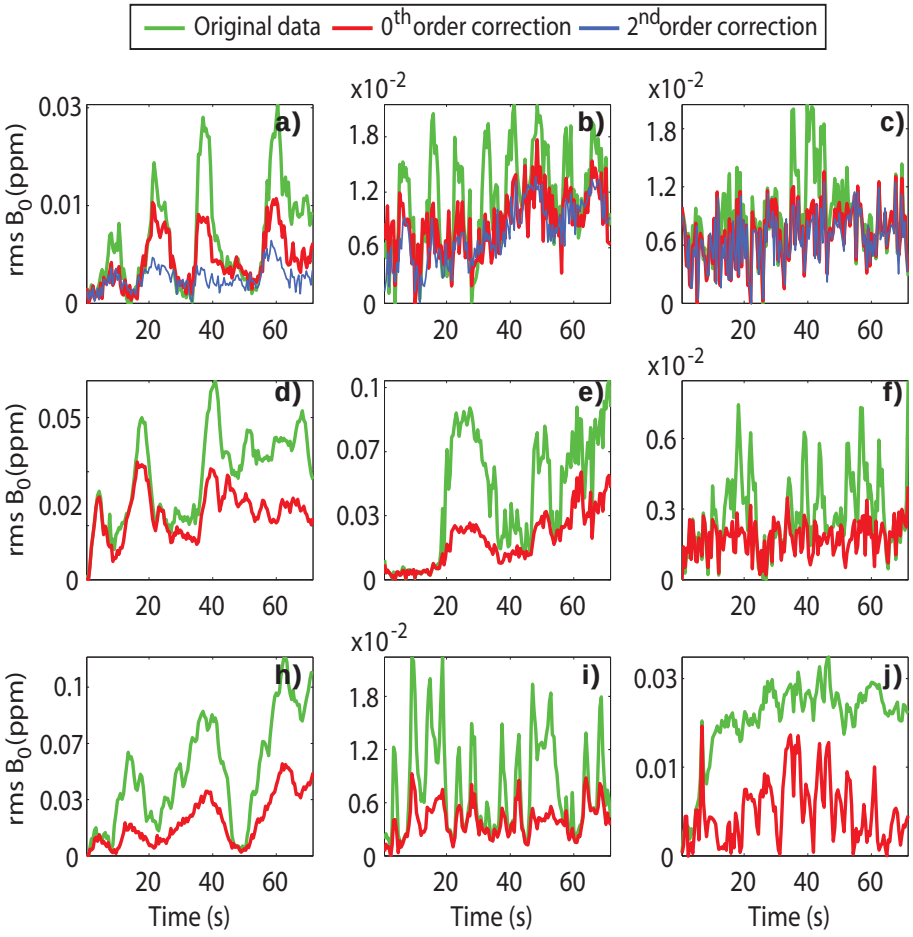

Figure 6.2: Temporal frequency variations expressed as the root mean square value over the prostate in ppm. Notice all plots have different scaling. The green lines show the original measured dynamic variation during a period of 74 seconds. The red lines show the effect of applying a simulated zero order dynamic B_0 shim correction and the blue lines, a second order dynamic correction (only showed for a, b and c). The zero order correction shows to be the dominant component for reducing the dynamic variations (41% reduction in average). The second order dynamic correction reduces the dynamic variations even more, yet the total variation decrease resulted in 56% average.

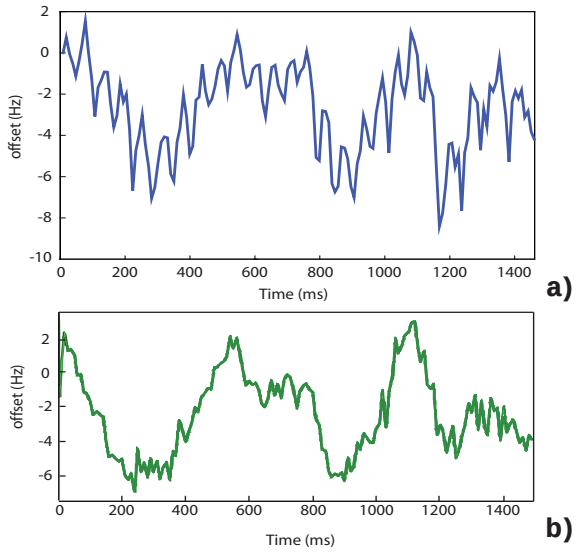

Figure 6.3: Comparison between the dynamic field variations obtained with the dynamic B0 map and the field monitoring obtained with the field probe within the ERC. Both measurements have a similar variation pattern with a total variation range of about 8 Hz during this measurement.

It was shown that within the prostate the dominant spatial varying field term is a zero order spatial harmonic, which when corrected for can reduce these variations by 41% on average. When incorporating first and second order spatial components as well, the hypothetical corrections of the dynamic variations yielded another 15% reduction in average. Although these results were obtained at the field strength of 7 Tesla, the susceptibility induced effects on the MR spectrum is field strength independent. Therefore, the application of dynamic field variation corrections would also improve the spectral resolution in prostate MRS at conventionally used MR systems, such as 1.5T and 3T. While some of the factors that result in dynamic B_0 variations may have been anticipated for by using cardiac triggering or breathing triggered calibrated field compensation(6), we used real-time field monitoring and retrospective field correction. In this way, unpredicted field variation effects can also be compensated for (i.e. bowel motion, air pockets). This proof of principle study has shown the feasibility of inserting a field probe inside the housing of an ERC for the real-time recording of the dominant zero order dynamic field variations in the prostate. As the field probe was operated at the ^{19}F frequency, the field changes could be detected without affecting the performances of the MRI or MRSI experiments. As one probe was used,

only zero order corrections could be assessed in real-time. However, since the zero order term was found to be the dominant one, significant improvements were observed in the MRSI data after retrospective corrections as demonstrated in a prostate cancer patient that showed small field fluctuations measured in real-time. In both cases the artifacts that were present in the non-corrected spectra, were significantly reduced after field probe based corrections.

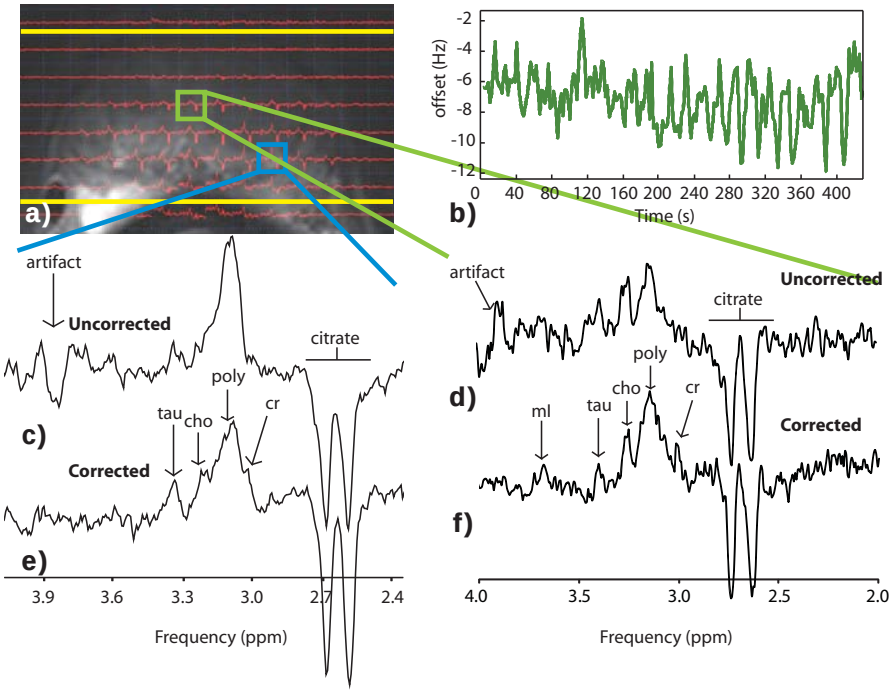

Figure 6.4: MRSI example from a human prostate showing a) the spectral map overlaid on the T2-weighted image of the prostate, b) field probe monitoring results during the MRSI data acquisition, c) a spectrum from a voxel close to the ERC without and d) with inclusion of the field probe corrections. A second spectrum from a voxel further away from the ERC is also shown e) without and f) with field probe corrections. In both cases (close and far from the ERC), the retrospective correction with the field probe data, substantially improves the spectral quality and resolution as seen by the better depiction of the metabolites mI (f), tau, Cho, Poly and Cr. Artifacts that were present in both cases at around 3.9 ppm are removed and the line width calculated with the citrate peaks improved in 40% and 24% in the close and far voxel case respectively.

Besides the degradation of the line width or spectral resolution caused by the temporal variations, artifacts such as ghosting can also obscure the MRS data, particularly in MRSI that uses k-space encoding. With the field probe information, these artifacts could be reduced (i.e below noise level), hence improving spectral quality even more, which would result in more reliable quantifications.

6.5 Conclusions

Spatial B_0 uniformities that can be obtained within the human prostate could enable distinct detection of signals of polyamines from choline and creatine at 7T. However, temporal B_0 variations are observed in prostate patients of more than 0.1 ppm within the time frame used to obtain MRSI measurements. We have shown that the temporal differences can be monitored and investigated without prior knowledge using dynamic B_0 mapping techniques. These temporal differences have a dominant zero order term, but include considerable contributions of the second order shim terms as well. The implementation of a monitoring field probe within the housing of the ERC was shown to be feasible. The acquired field probe data matches the data obtained with the simultaneously acquired dynamic B_0 mapping. Proof of concept in correcting MRSI data with the field probe data was shown to substantially improve the spectral resolution enabling accurate, robust and distinct detection of choline, polyamine, creatine and citrate mapped over the prostate.

REFERENCES

1. Fütterer JJ, Heijmink SWTPJ, Scheenen TWJ, Veltman J, Huisman HJ, Vos P, de Kaa CAHV, Witjes JA, Krabbe PFM, Heerschap A, Barentsz JO. Prostate Cancer Localization with Dynamic Contrast-enhanced MR Imaging and Proton MR Spectroscopic Imaging. Radiology 2006;241(2):449-458.

2. Reinsberg SA, Payne GS, Riches SF, Ashley S, Brewster JM, Morgan VA, deSouza NM. Combined Use of Diffusion-Weighted MRI and 1H MR Spectroscopy to Increase Accuracy in Prostate Cancer Detection. American Journal of Roentgenology 2007;188(1):91-98.

3. Yaligar J, Thakur SB, Bokacheva L, Carlin S, Thaler HT, Rizwan A, Lupu ME, Wang Y, Matei CC, Zakian KL, Koutcher JA. Lactate MRSI and DCE MRI as surrogate markers of prostate tumor aggressiveness. NMR in

Biomedicine 2012;25(1):113–122.

4. Klomp DWJ, Scheenen TWJ, Arteaga CS, van Asten J, Boer VO, Luijten PR. Detection of fully refocused polyamine spins in prostate cancer at 7 T. NMR in Biomedicine 2010;24(3):299-306.

5. Shukla-Dave A, Hricak H, Moskowitz C, Ishill N, Akin O, Kuroiwa K, Spector J, Kumar M, Reuter VE, Koutcher JA, Zakian KL. Detection of Prostate Cancer with MR Spectroscopic Imaging: An Expanded Paradigm Incorporating Polyamines. Radiology 2007;245(2):499-506.

6. van Gelderen P, de Zwart JA, Starewicz P, Hinks RS, Duyn JH. Real-time shimming to compensate for respiration-induced B0 fluctuations. Magnetic Resonance in Medicine 2007;57(2):362-368.

7. Boer VO, vd Bank BL, van Vliet G, Luijten PR, Klomp DWJ. Direct B0 field monitoring and real-time B0 field updating in the human breast at 7 tesla. Magnetic Resonance in Medicine 2012;67(2):586-591.

8. Versluis MJ, Sutton BP, de Bruin PW, Börnert P, Webb AG, van Osch MJ. Retrospective image correction in the presence of nonlinear temporal magnetic field changes using multichannel navigator echoes. Magnetic Resonance in Medicine 2012;68(6):1836-1845.

9. Barmet C, Zanche ND, Pruessmann KP. Spatiotemporal magnetic field monitoring for MR. Magnetic Resonance in Medicine 2008;60(1):187-197.

10. Barmet C, De Zanche N, Wilm BJ, Pruessmann KP. A transmit/receive system for magnetic field monitoring of in vivo MRI. Magnetic Resonance in Medicine 2009;62(1):269-276.

11. Arteaga de Castro CS, van den Bergen B, Luijten PR, van der Heide UA, van Vulpen M, Klomp DWJ. Improving SNR and B1 transmit field for an endorectal coil in 7 T MRI and MRS of prostate cancer. Magnetic Resonance in Medicine 2012;68(1):311-318.

12. Scheenen TWJ, Fütterer J, Weiland E, van Hecke P, Lemort M, Zechmann C, Schlemmer H-P, Broome D, Villeirs G, Lu J, Barentsz J, Roell S, Heerschap A. Discriminating Cancer From Noncancer Tissue in the Prostate by 3-Dimensional Proton Magnetic Resonance Spectroscopic Imaging. Investigative Radiology 2011;46(1):25-33.

13. Scheenen TWJ, Heijmink SWTPJ, Roell SA, Hulsbergen–Van de Kaa CA, Knipscheer BC, Witjes JA, Barentsz JO, Heerschap A. Three-dimensional

Proton MR Spectroscopy of Human Prostate at 3 T without Endorectal Coil: Feasibility. Radiology 2007;245(2):507-516.

14. Jung JA, Coakley FV, Vigneron DB, Swanson MG, Qayyum A, Weinberg V, Jones KD, Carroll PR, Kurhanewicz J. Prostate Depiction at Endorectal MR Spectroscopic Imaging: Investigation of a Standardized Evaluation System. Radiology 2004;233(3):701-708.

15. van Asten J, Cuijpers V, Hulsbergen-van de Kaa C, Soede-Huijbregts C, Witjes J, Verhofstad A, Heerschap A. High resolution magic angle spinning NMR spectroscopy for metabolic assessment of cancer presence and Gleason score in human prostate needle biopsies. Magnetic Resonance Materials in Physics, Biology and Medicine 2008;21(6):435-442.

16. Cheng LL, Wu C-l, Smith MR, Gonzalez RG. Non-destructive quantitation of spermine in human prostate tissue samples using HRMAS 1H NMR spectroscopy at 9.4 T. FEBS Letters 2001;494(1–2):112-116.

17. van der Graaf M, Schipper R, Oosterhof G, Schalken J, Verhofstad A, Heerschap A. Proton MR spectroscopy of prostatic tissue focused on the detection of spermine, a possible biomarker of malignant behavior in prostate cancer. Magnetic Resonance Materials in Physics, Biology and Medicine 2000;10(3):153-159.

CHAPTER 7

General Discussion

Through the chapters of this thesis we have described the development of new techniques for MR imaging and spectroscopic imaging at 7T. These developments were mainly intended for prostate applications; however some developed techniques can be applied to other body organs such as the human brain (e.g. **chapter 4**).

Ultra-high fields like 7 Tesla (7T) offer an increased SNR, which can be translated to an increased spatial and spectral resolution. However, there are many challenges associated with ultra-high fields. The shortening of the wavelength in the body to about 12 cm at 7T causes the appearance of B_1 transmit (B_1^+) and receive (B_1^-) RF field non-uniformities and interference patterns. In addition, because of the wavelength shortening, the penetration depth of the $B_1^{+/-}$ fields gets compromised. As the prostate is an organ deeply located in the pelvic region and the B_1^+ penetration depth was limited, an endorectal coil (ERC) approach seemed the most suitable option for prostate MR imaging and spectroscopy at 7T. However, when using a one element ERC at ultra-high field as it is used at lower fields (1-4), it results in transmit and receive asymmetries that difficult MR imaging and spectroscopy of the prostate. In **chapter 2** it was shown that the inclusion of a second element to an ERC improved the uniformity and coverage of the $B_1^{+/-}$ fields over the prostate, increased the SNR by a factor of $\sqrt{2}$ and gave a 4-fold reduction of the local SAR. As the dual-element ERC is still a surface coil, its inherent B_1 non-uniformity (in the anterior-posterior direction) remained.

At lower field strengths like 1.5 and 3T, the availability of pelvic phased-array coils makes the acquisition of full field of view images with uniform $B_1^{+/-}$ possible (5-8). At ultra-high field, such phased-array coils become suboptimal due to their limited penetration depth. As shown in **chapter 2,** a dual-element ERC for ultra-high field seemed optimal for prostate MR imaging and spectroscopy, given the improved B_1^+ coverage and homogeneity. However, such ERC transceiver lacks the ability of obtaining a uniform B_1 field and a full field of view of the pelvis. Therefore, new transceiver approaches such as radiative antennas (9) have been developed to improve the B_1 field uniformity and the field of view. With such elements an antenna-array could be made with uniform B_1^+ over the prostate to obtain good quality MRI of the human pelvis. However, the available B_1^+ amplitude reached with the antenna-array remained low, even after using B_1 shimming (9,10). This is detrimental for MRSI (i.e. low bandwidth pulses, increased local SAR and TE). Therefore, to obtain uniform B_1 MRI and strong B_1 MRSI within one scan session, we decided

to combine the radiative antennas array with the dual-element ERC. Conventionally, PIN-diode decoupling is used to decouple the ERC from the external elements. However, to enable transmission with the ERC for achieving the strong B_1 fields, the PIN-diodes have to be avoided. The RF coupling between the external and internal elements is already known to be low at the ultra-high field of 7T, even in a lean volunteer (11). However, the RF coupling had to be addressed in our investigation as well. We showed that when transmitting with the external array the RF coupling on the ERC was minimal. However, in some cases it resulted in signal voids at the prostate location, thus degrading image quality. This was resolved with the use of an optimized active decoupling protocol that increased the local SAR. With this coils-antennas combination we showed that it was possible to obtain high quality MR images of the human prostate with a uniform B_1 when using the actively decoupled ERC. In addition, strong B_1, short TE and TR MRSI was obtained when constructively interference transmission was done with all elements at maximum RF peak power. The presence of the ERC enhanced the SNR during the MRI acquisitions. The presence of the external array during MRSI increased the B_1 field coverage to the anterior side of the prostate.

Although we showed in **chapter 3** that good quality MR imaging of the human prostate could be achieved, the presence of the ERC for MR spectroscopic imaging still posed some challenges, such as the inherent B_1 non-uniformity of this surface coil, even when combined with the external array. To address this issue, MRS sequences with adiabatic pulses were investigated. Already in **chapter 2** it was shown that MRSI could be acquired with the dual-element ERC using a localization by adiabatic selection and refocusing (LASER) sequence (12). The LASER sequence is a fully adiabatic sequence, insensitive to the B_1 non-uniformities. However, the amount of adiabatic pulses needed for volume selection makes the LASER a SAR consuming sequence with a relatively long echo time. In order to increase the SNR of the MRSI signals obtained in the human prostate, two new adiabatic approaches were developed in **chapter 4**. Based on a semi-LASER sequence (13), two fully adiabatic sequences were implemented: the nsLASER and the cLASER for 2D and 3D MRSI respectively. In the case of the nsLASER, the limited coverage of the ERC on the right-left direction was used as an advantage by making the excitation pulse adiabatic and non-selective. The flip angles obtained with the nsLASER in-vivo were uniform over the whole field of view and the signals did not show lipid or water signals contamination from the voxels outside the prostate. However, due to the non-selective excitation of the nsLASER, the field of

view had to be extended in the right-left direction to prevent folding over artifacts and signal contamination, lengthening the nsLASER acquisition time. With the implementation of the 3D cLASER sequence, several issues were improved. The excitation was made adiabatic and spatially-selective by pulse segmentation allowing for 3D volume selection at a respectably acquisition time. In addition, the chemical shift displacement artifact was found to be only 1% with the composite excitation. The flip angles obtained with the cLASER in-vivo were uniform as expected due to the adiabatic nature of the sequence. However, due to the use of single lobe sinc pulses for the segments of the excitation pulse, oversampling had to be done to prevent point spread contamination.

The methods developed so far can detect metabolites that can be well resolved. However, some signals of interesting metabolites like lactate still overlap with higher signals like lipids making their detection challenging. Several techniques already exist for detecting these overlapping low concentrated metabolites (e.g. homonuclear transfer, double quantum filters, 2D MRS, spectral editing and LC model fitting (14-20)), but MRS editing is the easiest to implement. However, for metabolites with chemical shifts distant from each other, MRS editing techniques can be highly inefficient. Therefore, we decided to include broad-banded frequency offset corrected inversion (FOCI) pulses for refocusing into a MEGA-sLASER MRS editing sequence (19). As MRS editing sequences rely in subtraction of the interleaved acquired signals, which can cause artifacts or signal decrease due to f_0 misalignments, the human brain was used as a model to test the method. The resulting sequence showed improved signal detection efficiency for measuring GABA and even lactate (2.8 ppm apart spin groups) of up to 26% and 75% respectively. When compared to conventional adiabatic hyperbolic secant (HS) pulses, the broad-banded, adiabatic FOCI pulses increased the local SAR, although kept within guidelines. However, the adiabaticity of the FOCI pulses allowed decreasing the B_1 amplitude or the so-called *FOCI factor* (f_F), while keeping the broad-banded spatial profiles. B_1 focusing could also be applied as an alternative to lower local SAR even further (21). To make this type of sequences work for the prostate would be advantageous for obtaining lactate signals. Lactate is a marker in hypoxic tissue (22,23) and it has been linked to tissue aggressiveness (24,25), hence its detection may improve the prostate cancer diagnostics specificity. The spectral resolution in voxels inside the prostate depends on the homogeneity of the main magnetic field B_0, which can be affected by susceptibility differences of tissues in and outside the prostate. These

susceptibility differences can be substantial outside the prostate (i.e. transitions from tissue to air or even lipids), which can lead to static and temporal magnetic field (B_0) non-uniformities inside the prostate. The static variations can be solved by external B_0 shimming for a uniform field inside the prostate. The use of an ERC for MRI and MRSI already helps fixating the prostate, hence minimizing movement and some of the temporal B_0 variations. However, the susceptibility sources that cause the temporal B_0 variations can be originated elsewhere in the body. Therefore, in **chapter 6** monitoring, measuring and correction of the effects of the temporal B_0 variations, without having prior-knowledge of their origin were explored. The results exposed in **chapter 6** showed that the B_0 field variations can be monitored with fast B_0 mapping techniques and can be as large as 30 Hz, corresponding to 0.1 ppm at 7T. This maximum variation could have important consequences for prostate MRSI, given that the separation between choline (3.2 ppm) or creatine (3.0 ppm) and polyamines (3.1 ppm) coincides with the maximum variation found of 0.1 ppm. In addition, the field variations could be monitored in real-time with a field probe (FP) integrated in the housing of the ERC. The FP results coincided with the fast B_0 mapping results and retrospective corrections were possible in an MRSI data set. The retrospective corrections using the FP data improved the peaks detection, the line width (up to 41%) and it decreased artifacts substantially. The presence of such a FP inside the ERC for monitoring the B_0 field variations could also be advantageous to correct MRI data sets. In addition, the ability to provide dynamic B_0 corrections to MRSI data sets would enable the stable acquisition of other low concentration metabolites such as lactate using MRS editing.

Conclusions

New ultra-high field techniques have been developed for prostate MR(S) imaging. These techniques have shown substantial potential for acquisition of high (spatial) spectral resolution data that would benefit clinical diagnostics performed at 7T. In particular, uniform full field of view MRI of the pelvis can now be obtained at 7T notwithstanding its challenges, with a higher signal to noise ratio than at lower field strengths. In addition, the developed adiabatic MRS(I) sequences made possible the detection of metabolite signals, even with low concentrations such as lactate, with higher SNR than at lower fields. The improved quality of the MRS(I) data found at 7T may provide a higher diagnostic specificity for the human prostate. The ultra-high field strength of 7T is still considered

a research field strength. We have changed this with the developed techniques that put the 7T MR scanner closer to the clinical use.

Future directions

Accurate assessment of the spectral quality obtained at 7T compared to the one at 3T can now be performed, as the challenges of prostate MRSI at 7T have been overcome. In addition, the gain of including the distinct detection of the polyamines into prostate cancer grading can be assessed.

It remains to be seen if metabolites such as lactate can be accurately measured in the human prostate, as it was in the brain with a MEGA-sLASER sequence or an equivalent. Inclusion of retrospective corrections using navigators or real-time monitoring devices such as a field probe would improve the detection accuracy in those field variation-sensitive experiments.

Metabolic information of other nuclei, such as 31-phosphor (^{31}P), can also be incorporated into the prostate diagnostics chain. Phosphor metabolites offer additional information of cell formation and depletion. All the additional information (i.e. lactate and ^{31}P metabolites) would greatly benefit the specificity of prostate cancer diagnostics by helping differentiating aggressive tissue from necrotic or benign tissue.

As for the development of the MRSI sequences, special attention is directed to speed-up acquisition techniques, such as EPI readouts to reduce the total acquisition time and obtain 3D MRSI acquisitions of the whole prostate.

REFERENCES

1. Kurhanewicz J, Vigneron DB, Nelson SJ, Hricak H, MacDonald JM, Konety B, Narayan P. Citrate as an in vivo marker to discriminate prostate cancer from benign prostatic hyperplasia and normal prostate peripheral zone: Detection via localized proton spectroscopy. Urology 1995;45(3):459-466.

2. Yu KK, Scheidler J, Hricak H, Vigneron DB, Zaloudek CJ, Males RG, Nelson SJ, Carroll PR, Kurhanewicz J. Prostate Cancer: Prediction of Extracapsular Extension with Endorectal MR Imaging and Three-dimensional Proton

MR Spectroscopic Imaging. Radiology 1999;213(2):481-488.

3. Futterer JJ, Scheenen TWJ, Huisman HJ, Klomp DWJ, van Dorsten FA, Hulsbergen-van de Kaa CA, Witjes JA, Heerschap A, Barentsz JO. Initial Experience of 3 Tesla Endorectal Coil Magnetic Resonance Imaging and 1H-Spectroscopic Imaging of the Prostate. Investigative Radiology November 2004 2004;39(11):671-680.

4. Scheenen TWJ, Gambarota G, Weiland E, Klomp DWJ, Fütterer JJ, Barentsz JO, Heerschap A. Optimal timing for in vivo 1H-MR spectroscopic imaging of the human prostate at 3T. Magnetic Resonance in Medicine 2005;53(6):1268-1274.

5. Heijmink SWTPJ, Fütterer JJ, Hambrock T, Takahashi S, Scheenen TWJ, Huisman HJ, Hulsbergen–Van de Kaa CA, Knipscheer BC, Kiemeney LALM, Witjes JA, Barentsz JO. Prostate Cancer: Body-Array versus Endorectal Coil MR Imaging at 3 T—Comparison of Image Quality, Localization, and Staging Performance. Radiology 2007;244(1):184-195.

6. Sato C, Naganawa S, Nakamura T, Kumada H, Miura S, Takizawa O, Ishigaki T. Differentiation of noncancerous tissue and cancer lesions by apparent diffusion coefficient values in transition and peripheral zones of the prostate. Journal of Magnetic Resonance Imaging 2005;21(3):258-262.

7. Shukla-Dave A, Hricak H, Moskowitz C, Ishill N, Akin O, Kuroiwa K, Spector J, Kumar M, Reuter VE, Koutcher JA, Zakian KL. Detection of Prostate Cancer with MR Spectroscopic Imaging: An Expanded Paradigm Incorporating Polyamines. Radiology 2007;245(2):499-506.

8. Scheenen TWJ, Heijmink SWTPJ, Roell SA, Hulsbergen–Van de Kaa CA, Knipscheer BC, Witjes JA, Barentsz JO, Heerschap A. Three-dimensional Proton MR Spectroscopy of Human Prostate at 3 T without Endorectal Coil: Feasibility. Radiology 2007;245(2):507-516.

9. Raaijmakers AJE, Ipek O, Klomp DWJ, Possanzini C, Harvey PR, Lagendijk JJW, van den Berg CAT. Design of a radiative surface coil array element at 7 T: The single-side adapted dipole antenna. Magnetic Resonance in Medicine 2011;66(5):1488-1497.

10. Metzger GJ, Snyder C, Akgun C, Vaughan T, Ugurbil K, Moortele P-FVd. Local B1+ shimming for prostate imaging with transceiver arrays at 7T based on subject-dependent transmit phase measurements. Magnetic Resonance in Medicine 2008;59(2):396-409.

11. Metzger GJ, van de Moortele P-F, Akgun C, Snyder CJ, Moeller S, Strupp J, Andersen P, Shrivastava D, Vaughan T, Ugurbil K, Adriany G. Performance of external and internal coil configurations for prostate investigations at 7 T. Magnetic Resonance in Medicine 2010;64(6):1625-1639.

12. Garwood M, DelaBarre L. The Return of the Frequency Sweep: Designing Adiabatic Pulses for Contemporary NMR. Journal of Magnetic Resonance 2001;153(2):155-177.

13. Klomp DWJ, Bitz AK, Heerschap A, Scheenen TWJ. Proton spectroscopic imaging of the human prostate at 7 T. NMR in Biomedicine 2009;22(5):495-501.

14. Lee HK, Yaman A, Nalcioglu O. Homonuclear J-refocused spectral editing technique for quantification of glutamine and glutamate by 1H NMR spectroscopy. Magnetic Resonance in Medicine 2005;34(2):253-259.

15. De Graaf RA, Dijkhuizen RM, Biessels GJ, Braun KPJ, Nicolay K. In vivo glucose detection by homonuclear spectral editing. Magnetic Resonance in Medicine 2000;43(5):621-626.

16. Keltner JR, Wald LL, Frederick BDB, Renshaw PF. In vivo detection of GABA in human brain using a localized double-quantum filter technique. Magnetic Resonance in Medicine 2005;37(3):366-371.

17. Lange T, Trabesinger AH, Schulte RF, Dydak U, Boesiger P. Prostate spectroscopy at 3 Tesla using two-dimensional S-PRESS. Magnetic Resonance in Medicine 2006;56(6):1220-1228.

18. Lazeyras F, Terrier F, Aue WP, Frey FJ, Howarth N. Measurement of lactate in acutely ischemic rat kidneys using magnetic resonance spectroscopy. Investigative Radiology 1994;29(1):24-30.

19. Andreychenko A, Boer VO, Arteaga de Castro CS, Luijten PR, Klomp DW. Efficient spectral editing at 7 T: GABA detection with MEGA-sLASER. Magn Reson Med 2012;68(4):1018-1025.

20. Lange T, Schulte RF, Boesiger P. Quantitative J-resolved prostate spectroscopy using two-dimensional prior-knowledge fitting. Magnetic Resonance in Medicine 2008;59(5):966-972.

21. Boer VO, van Lier ALHMW, Hoogduin JM, Wijnen JP, Luijten PR, Klomp DWJ. 7-T 1H MRS with adiabatic refocusing at short TE using radiofrequency focusing with a dual-channel volume transmit coil. NMR in Biomedicine 2011;24(9):1038-1046.

22. Behar KL, Rothman DL, Shulman RG, Petroff OA, Prichard JW. Detection of cerebral lactate in vivo during hypoxemia by 1H NMR at relatively low field strengths (1.9 T). Proc Natl Acad Sci U S A 1984;81(8):2517-2519.

23. Duijn JH, Matson GB, Maudsley AA, Hugg JW, Weiner MW. Human brain infarction: proton MR spectroscopy. Radiology 1992;183(3):711-718.

24. van Asten J, Cuijpers V, Hulsbergen-van de Kaa C, Soede-Huijbregts C, Witjes J, Verhofstad A, Heerschap A. High resolution magic angle spinning NMR spectroscopy for metabolic assessment of cancer presence and Gleason score in human prostate needle biopsies. Magnetic Resonance Materials in Physics, Biology and Medicine 2008;21(6):435-442.

25. Yaligar J, Thakur SB, Bokacheva L, Carlin S, Thaler HT, Rizwan A, Lupu ME, Wang Y, Matei CC, Zakian KL, Koutcher JA. Lactate MRSI and DCE MRI as surrogate markers of prostate tumor aggressiveness. NMR in Biomedicine 2012;25(1):113–122.

English Summary

This thesis is the result of a PhD project dedicated to developing new techniques for MR imaging and spectroscopy of the human prostate at high field strengths. In order to image the prostate at the high field of 7 Tesla, a dedicated endorectal coil (ERC) for the prostate was constructed with two transceiver elements. With the 2-elements ERC homogeneous imaging with increased coverage (mainly in the anterior-posterior direction) of the prostate was possible. In addition, the inclusion of the second channel to the ERC reduced the local radiofrequency (RF) power deposition by 4-fold, enabling the use more RF demanding MR sequences while keeping local and global safety values below the maximum limits. The lack of a body coil at the high field of 7 Tesla limited the acquisition of MR imaging of the prostate with full diagnostic potential. Therefore, a combined setup of six external radiative antennas with an internal two-element ERC without the use of PIN-diodes was developed. When only transmitting with the external elements, this coil-antennas combination showed minimal interaction between the external and the internal components in the form of RF coupling, as expected from the high tissue load dominance. Notwithstanding, the RF coupling could be removed using active decoupling by transmitting with both channels of the ERC with only a fraction of the maximum amplitude and an optimized phase. This complete setup made possible to acquire homogeneous prostate MRI with a full field of view when using the active decoupling scheme and a short echo time with strong B_1 MRSI measurements when transmitting with all elements (coils and antennas) at maximum amplitude.

As the dedicated efficient ERC for the human prostate is a surface coil, its B_1 field remained non-uniform. Therefore, adiabatic MR sequences for spectroscopy were developed to obtain prostate metabolic information. The limited coverage in the transverse direction of the ERC made it possible to implement a fully adiabatic 2D MR spectroscopic imaging (MRSI) sequence (i.e nsLASER) with a non-selective adiabatic excitation. The nsLASER sequence was expanded to a 3D MRSI sequence (cLASER), which used a composite adiabatic slice-selective excitation. Both nsLASER and cLASER sequences were tested in-vivo in prostate cancer patients and showed improved performances when compared to non- or semi-adiabatic sequences for detecting the prostate metabolites. The development of MRS sequences followed with the implementation of a semi-LASER editing technique with Mescher-Garwood pulses (MEGA-sLASER), for editing J-coupled metabolites (e.g. lactate) and frequency-offset-corrected inversion (FOCI) pulses for slice selection refocusing. The MEGA-sLASER with FOCI pulses showed a substantially reduced chemical

shift displacement artifact (CSDA), enhanced signal detection efficiency particularly for measuring lactate and an improved spatial localization profile.

The developments for prostate MR imaging and spectroscopic imaging continued after observing substantial static B_0 field temporal variations that were the cause of poor MR spectral resolution and presence of artifacts in some cases. This point was approached with the development of a field probe (FP) inserted within the housing of the ERC for real-time monitoring of the static B_0 field variations. The FP was tuned and match at the 19Fluor frequency; therefore, it did not interfere with the ^1H measurements. The FP real-time monitoring was validated with a dynamic B_0 mapping technique. In addition, retrospective corrections could be done on a MRSI in-vivo data set obtained in the human prostate, showing improved spectral resolution, line width decrease and artifact removal when compared to the uncorrected data set. Because the field variations are induced by susceptibilities that are field strength independent, this method is not only useful for monitoring the field variations at ultra high field but also at lower field strengths.

Samenvating in het Nederlands

Dit boek is het resultaat van een promotie-project in welke het ontwikkelen van nieuwe technieken voor MR beeldvorming en spectroscopie van de prostaat bij hoge veldsterktes centraal staat. Om beeldvorming van de prostaat te verkrijgen op de hoge veldsterkte van 7 tesla, werd een speciale endorectale spoel (ERC) voor de prostaat ontworpen met twee zend-elementen. Deze 2-elementen ERC maakt homogene beeldvorming met verbeterde dekking van de prostaat (vooral in de anterior-posterior richting) mogelijk. Bovendien is door de toevoeging van het tweede element in de ERC de lokale radiofrequentie (RF) energie depositie met een 4-voud verminderd, waardoor het gebruik van meer RF eisende MR sequenties mogelijk is terwijl de lokale en globale veiligheidswaarden onder de grenswaarden blijven. Het ontbreken van een "body-coil" op de hoge veldsterkte van 7 tesla beperkt de acquisitie van MR beeldvorming van de prostaat voor diagnostische mogelijkheden. Daarom werd een gecombineerde opstelling ontwikkeld zonder gebruik van PIN-dioden bestaande uit zes externe "radiative antennas" en de interne twee elementen ERC. Het zenden werd gedaan met enkel de externe elementen, deze combinatie van spoelen liet een minimale interactie tussen de externe en interne componenten zien in de vorm van RF koppeling, zoals verwacht door de hoge weefsel dominantie. De RF koppeling kan worden verwijderd door gebruik te maken van actieve ontkoppeling door te zenden met beide kanalen van de ERC het gebruik van slechts een fractie van de maximale amplitude en een geoptimaliseerde fase. Deze complete opstelling maakte het mogelijk om homogene prostaat beeldvorming te verkrijgen met een volledige dekking van de prostaat en omliggende structuren wanneer gebruik wordt gemaakt van actieve ontkoppeling. Daarnaast waren door te zenden met de maximale amplitude van de ERC korte echo tijd MRSI metingen mogelijk met een hoge B_1.

Omdat de efficiënte ERC is toch een oppervlakkig spoel, zijn B_1 veld profiel bleef niet uniform, daarom werden adiabatische MR sequenties voor spectroscopie ontwikkeld welke informatie geven over het metabolisme in de prostaat. De beperkte dekking in de dwarsdoorsnede van de ERC maakte het mogelijk om een volledig adiabatische 2D MR spectroscopische beeldvorming (MRSI) sequentie (nsLASER) te implementeren met een niet-selectieve adiabatische excitatie. De nsLASER sequentie werd uitgebreid tot een 3D MRSI sequentie (cLASER), die een samengestelde adiabatische plak-selectieve excitatie gebruikt. De nsLASER en cLASER sequenties werden getest in vivo in prostaatkankerpatiënten en toonden betere resultaten vergeleken met niet-of semi-adiabatische sequenties

voor het detecteren van de prostaat metabolieten. De ontwikkeling van MRS sequenties werd gevolgd door de implementatie van een semi-LASER editing techniek met Mescher-Garwood pulsen (MEGA-sLASER), voor het editen van J-gekoppelde metabolieten (bijvoorbeeld lactaat) en frequentie-offset gecorrigeerde inversie (FOCI) pulsen voor slice selectie refocusing. De MEGA-sLASER met FOCI pulsen toonde een sterk verbeterde signaal detectie in het bijzonder voor het meten van lactaat en een verbeterd ruimtelijk lokalisatie profiel. Dit blijkt uit met in-vivo metingen van lactaat van de menselijke brein.

De ontwikkelingen voor prostaat MR beeldvorming en spectroscopische beeldvorming werden voortgezet na het observeren van grote temporele variaties van het statische B_0 veld die in diverse patientën de oorzaak waren van een slechte spectrale resolutie en de aanwezigheid van artefacten. Hiervoor werd een veld camera (VC) ingebracht in de behuizing van de ERC voor real-time registratie van de statische B_0 veld variaties. De VC werd geoptimaliseerd voor de frequentie van 19-Fluor, en had daardoor geen invloed op de ^1H metingen. De VC real-time registratie werd gevalideerd met een dynamische B_0 mapping techniek. Bovendien kan door de verkregen informatie tijdens de meting achteraf een correctie worden uitgevoerd op een in-vivo MRSI dataset verkregen in de menselijke prostaat, dit leidt tot een verbeterde spectrale resolutie, afname van de lijnbreedte en minder artefacten in vergelijking met de ongecorrigeerde dataset. Omdat de veldvariaties worden geïnduceerd door oorzaken die veldsterkte onafhankelijk zijn, is deze methode niet alleen nuttig om de veldvariaties bij zeer hoge veldsterkten in beeld te brengen, maar ook bij lagere veldsterkten.

Resumen en Castellano

Esta tesis es el resultado de un proyecto de doctorado dedicado al desarrollo de nuevas técnicas para obtener imágenes y espectroscopia de resonancia magnética (RM) de la próstata a altos campos magnéticos como 7 tesla. Una bobina endorectal (BE) fue construida con dos elementos transductores para obtener imágenes de RM (IRM) de la próstata. Ésta BE de dos elementos posibilitó la obtención de imágenes de RM con una mayor cobertura de la próstata (mayormente en la dirección anterio-posterior) comparado con la BE de un solo elemento. La inclusión del segundo elemento transductor en la BE redujo la deposición de energía de radio frecuencia (RF) en un factor 4, lo que hizo posible usar secuencias de RM que demandan más energía de RF, manteniendo los niveles locales y globales de seguridad dentro de los límites permitidos.

La falta de una bobina de cuerpo completo para el campo magnético de 7 tesla, limita la obtención de imágenes de RM de la próstata con un potencial más alto para el diagnóstico del cáncer a la próstata. Por esta razón es que se desarrolló un conjunto de seis antenas radiativas externas para usar en combinación con la BE interna, excluyendo el uso de diodos-PIN. Como era de esperarse, por la dominancia del tejido sobre los transductores (antenas y ERC), al transmitir sólo con los elementos externos, esta combinación de antenas mostró una mínima interferencia de RF entre los elementos externos e internos, que de todas maneras pudo ser corregida mediante el uso de desacoplamiento activo, al transmitir con la BE con sólo una fracción de la energía máxima y una fase optimizada. El uso de la combinación de antenas externas con la BE posibilitó la obtención de imágenes homogéneas de RM en la próstata, con una mayor cobertura de la anatomía que la rodea al usar la técnica de desacoplamiento activo. Además, IRMS pudo ser obtenido con un tiempo de eco corto y una amplitud de transmisión (B_1) alta, al transmitir con la ERC con las amplitudes máximas.

La habilitación de esta dedicada y eficiente ERC para la próstata humana habilitó el desarrollo de secuencias de imágenes de RM espectroscópica (IRMS) para obtener información metabólica de la próstata. La ERC tiene una cobertura limitada en la dirección transversal (derecha-izquierda) que resultó ventajosa para poder implementar una secuencia 2D de IRMS enteramente adiabática llamada nsLASER, usando un pulso de excitación adiabático no selectivo. La secuencia nsLASER fue expandida a una secuencia 3D de IRMS (cLASER) usando un pulso de excitación adiabático compuesto y selectivo. Ambas secuencias, nsLASER y cLASER, fueron testeadas en-vivo en pacientes con cáncer a la próstata y mostraron un mejor rendimiento comparado con secuencias no- o semi-

adiabáticas usadas para detectar información metabólica de la próstata. La explotación de secuencias de RMS se continuó con la implementación de la secuencia semi-LASER con pulsos Mescher-Garwood (MEGA-sLASER), para editar metabolitos J-acoplados (ej. Acido γ-aminobutírico (GABA) y ácido láctico) y con pulsos de inversión con offset de frecuencia corregidos (FOCI), para obtener ecos de spin en la selección de la imagen. Los pulsos FOCI mostraron reducción del artefacto de desplazamiento por diferencia química, mayor eficacia para detectar la señal, en particular para el acido láctico, y una mejoría en la selección espacial del volumen de interés. Todas las mejoras mencionadas fueron demostradas en-vivo en el cerebro humano con mediciones de GABA y de ácido láctico.

El desarrollo de técnicas para imágenes de RM y de espectroscopia continuó al observar que grandes variaciones temporales del campo magnético estático B_0 deterioraban la resolución espectral de RM o eran las causantes de artefactos en los espectros. Para corregir estas variaciones temporales se creó una sonda de campo (SC) magnético, la que fue insertada dentro de la cubierta de la ERC, para posibilitar el monitoreo en tiempo real de las variaciones del campo estático B_0. La SC fue afinada para resonar a la frecuencia del fluor-19 (^{19}F), por lo tanto no interfirió con las mediciones hechas a la frecuencia del hidrógeno (^{1}H contenido en las moléculas del agua). Las mediciones obtenidas con la SC en tiempo real fueron validadas con la obtención de mapas dinámicos del campo B_0 y luego usadas para corregir retrospectivamente un conjunto de datos de IRMS obtenidos en-vivo en un paciente con cáncer a la próstata. Comparando con los datos no corregidos, las correcciones retrospectivas resultaron en una mejora de la resolución espectral, una disminución del ancho de línea de los picos presentes en los espectros y en la remoción de artefactos. Como las variaciones del campo estático B_0 son inducidas por susceptibilidades que son independientes de la fuerza del campo magnético, este método no sólo resulta útil para el monitoreo en campos magnéticos de alta fuerza, sino que también para el monitoreo en campos más bajos.

List of Publications

1. Arteaga de Castro CS, van den Bergen B, Luijten PR, van der Heide UA, van Vulpen M, Klomp DWJ. Improving SNR and B1 transmit field for an endorectal coil in 7 T MRI and MRS of prostate cancer. Magnetic Resonance in Medicine 2012;68(1):311-318.

2. Arteaga de Castro CS, Luttje MP, van Vulpen M, Luijten PR, van der Heide UA, Klomp DWJ. Composite slice-selective adiabatic excitation for prostate MRSI. NMR in Biomedicine 2012;26(4):436-442.

3. Arteaga de Castro CS, Boer VO, Andreychenko A, Wijnen JP, van der Heide UA, Luijten PR, Klomp DWJ. Improved efficiency on editing MRS of lactate and g-aminobutyric acid by inclusion of frequency offset corrected inversion pulses at high fields. NMR in Biomedicine 2013;*In Press*.

4. Klomp DWJ, Scheenen TWJ, Arteaga CS, van Asten J, Boer VO, Luijten PR. Detection of fully refocused polyamine spins in prostate cancer at 7 T. NMR in Biomedicine 2010;24(3):299-306.

5. van den Bergen B, Klomp DWJ, Raaijmakers AJE, Arteaga de Castro C, Boer VO, Kroeze H, Luijten PR, Lagendijk JJW, van den Berg CAT. Uniform prostate imaging and spectroscopy at 7 T: comparison between a microstrip array and an endorectal coil. NMR in Biomedicine 2010;24(4):358-365.

6. Andreychenko A, Boer VO, Arteaga de Castro CS, Luijten PR, Klomp DW. Efficient spectral editing at 7 T: GABA detection with MEGA-sLASER. Magn Reson Med 2012;68(4):1018-1025.

7. Arteaga CS, van den Bergen B, Luijten PL, van der Heide UA, Klomp DWJ. Improving SNR and RF by Adding a Stripline to Endorectal Coil for the 7T. 2009; Honolulu, Hawaii. p 4744.

8. Arteaga CS, van der Heide UA, van Vulpen M, Luijten PR, Klomp DWJ. 1H MR Spectroscopy of the human prostate using an adiabatic sequence with a SAR optimized endorectal coil. 2010; Stockholm, Sweden. p 3502.

9. Arteaga CS, van der Heide UA, van Vulpen M, Luijten PR, Klomp DW. 31P MR Spectroscopy for Prostate Cancer Characterization at 7Tesla. 2010; Stockholm, Sweden. p 2805.

10. Arteaga de Castro CS, van der Hei UA, Van Vulpen M, Luijten PR, Klomp DWJ. Composite Localization with adiabatic slice selective excitation and refocusing (cLASER) for improved 1H MRSI in non uniform B1 fields. 2011; Montreal, Canada. p 1422.

11. Arteaga de Castro CS, Ipek O, Luttje MP, van Vulpen M, Noteboom J, Luijten PR, van der Heide UA, Klomp DWJ. Active Decoupling for Prostate MR Imaging and Spectroscopy with Extended Field of View at 7T. 2012; Melbourne, Australia. p 2640.

12. Arteaga de Castro CS, Luttje MP, van Vulpen M, van der Heide UA, Luijten PR, Klomp DWJ. RF Coil Selective Adiabatic Excitation in sLASER Sequence for 7T Prostate MRSI at short TE. 2012; Melbourne, Australia. p 1721.

13. Arteaga de Castro CS, Bhogal A, van Vulpen M, Noteboom J, Luijten PR, van der Heide UA, Klomp DWJ. Dynamic B0 Variations in the Prostate. 2012; Melbourne, Australia. p 1740.

14. Arteaga de Castro CS, Ipek O, Raaijmakers AJ, Luttje MP, Van Vulpen M, Luijten PR, van der Heide UA, Klomp DWJ. Uniform Extended FOV MR Imaging and High B1 MRSI of the prostate at 7 Tesla using active decoupling. 2013; Salt Lake City, US. p 1791.

15. Arteaga de Castro CS, Boer VO, Luttje MP, Van Vulpen M, Luijten PR, Van der Heide UA, Klomp DWJ. Correction of Dynamic B0 field changes in MRSI of the prostate at 7T using an internal field probe. 2013; Salt Lake City, US. p 554.

Curriculum Vitae

Catalina Sofía Arteaga de Castro was born in Santiago de Chile the 21st of June of 1982. Her basic education from first to fifth grade took place in different schools of the country, due to her father's work that force the family to move every two years. From sixth grade and on she was at the *Colegio del Sagrado Corazón* in Santiago, where she obtained her high school diploma in 1999. Her education continued at the *Universidad Católica de Chile* in 2000 where she studied Physics and obtained the degree of *Licenciada en Física* in 2005. In the same year, she got married with Axel who was doing a PhD in Astrophysics in The Netherlands at the moment. Thus, they decided to start their family life together in Utrecht, The Netherlands. In 2006, Catalina enrolled herself in the Master in Biomedical Image Sciences program at the Utrecht University, which ended successfully in 2008 after realizing a Master project at the department of radiotherapy at the University Medical Center Utrecht, The Netherlands dedicated to perfusion of cervix tumors. In the same year of 2008, she started a PhD in high field MR with the 7 Tesla team at the University Medical Center Utrecht. During her PhD project, she developed functional techniques for MR imaging and spectroscopy of the human prostate under the direct supervision of her promoter and co-promoters Peter R. Luijten, Dennis W.J. Klomp and Uulke A. van der Heide, respectively.

Currently, she started a post-doc project at the Netherlands Cancer Center (NKI) in Amsterdam following the prostate research with 3 Tesla MR Scanners.

Acknowledgments

It is so easy to say the words and there were so many times when I forgot to say it to all those that without their help this thesis would have never been possible, so I start by saying it one more time: “thank you“!

Dear Dennis, I won the lottery of the co-promotors with you!! without your support I do not know where I would be. You were always there with great new ideas, a big smile, a way to solve my problems and always that positive thinking which I admire so much and told me so many times how awesome all my ideas were! You always motivated me to keep on no matter what and for that I am incredible grateful. I also thank you for your friendship and the good times we had during my PhD, you are awesome!

Dear Uulke, I also won the co-promotors’ lottery with you. Although after you left to the NKI we did not see each other so often, everytime we got together was as always with a lot to catch up, not only from the research but also with our lives. I would not have miss one talk with you because I trully enjoyed them all. You always had an open mind to all my crazy ideas and tested me several times when you asked me to explain how the adiabatic pulses or the spectroscopy sequences worked!

Vincent you are incredible! thanks a lot for all your help! if it wasn’t because of you I would still be programming my first MR sequence!

Mariska, we had some downs while scanning patients but that made our friendship better and stronger. Thanks for all your support when I thought we were going nowhere. Thanks for all the snoepjes and the nice talks. Good luck with your studies and finishing your part of the prostate research!

Anna, thanks for all your help when I was lost and the time you listened to all my stories.

To Michel, Ingmar and the lab crew, thanks for all your handy help with the coils, you are the men! we also had great laughs at the lab, thanks!

I initially arrived at the Q2 and shared the office with Daniel, Jeroen and Vincent. Those guys can work and discuss! they also knew how to have fun. Thanks a lot guys for all the gezelligheid and the laughs.

At the Q4 we got all scrambled. During that time I got to share the office with Daniel, Wybe, Anita and fight for my desk with Wouter. Thanks for all the good fun guys!

Hans and Peter, thanks for all your advices, tips and good stories. Fredy, thanks for your MR help and funny stories during lunch.

At all the Q4 PhD students thanks for all the good cakes, cookies and fun. Now you also know how to properly light a bbq!!!! To all those party animals out there at Q4, we had great times!

To the people at radiotherapy thanks for all the good discussions we had.

Marco, without your help to get myself organized I would have never gotten this book on time. Thanks a lot for your preoccupation, you are a mentor!

Rene and Shanna, I don't know what I would have done without our music sessions. Those were my most necessary breaks. You guys were always there for me when I needed it the most. Lots of love for you two!

Catita y Adriaan, que ricos todos los asados que tuvimos juntos y que espero sean muchos más. Les agradezco de todo corazón por su amistad todo este tiempo. Los quiero mucho!

Maarten, Kate and Finna, I love you guys. Let's get together soon for another movie marathon... this time with kids!

Sabina, thanks for your patience. I was freaking out because I thought I couldn't finish this thesis and papers on time... you always kept me calm

and gave me hope, thanks a lot girl!

To all my friends, in The Netherlands and in Chile, you were and still are such important characters in my life. I love you all.

A mi familia que está en Chile, los quiero mucho a todos. Gracias por todo su apoyo a la distancia. Un Abrazo apretado a cada uno.

Papá y mamá, sin ustedes nada de esto habría sido posible. Esta tesis es para ustedes, a cambio de todo su esfuerzo por educarme como lo hicieron. Gracias por todo su apoyo en todo momento y por su interés en mi trabajo, a pesar de a veces no entender ni la mitad. Los amo con todo mi corazón papitos!

A mis amores Axel, Vincent y Drago... que quieren que les diga! ustedes completan mi vida y me llenan de dicha y alegría. Ya no me es posible imaginar mi vida sin ustedes. Durante todo este tiempo me han mantenido aterrizada y me ayudaron a no volverme loca entre tanto paper. LOS AMO con todo mi ser!

So many people make up my life, here in this lovely country that has welcomed me for so long and in my motherland, which I miss so much! I love you all.

Don't get lost!